# Exploring the Behaviour of Lanthanide-appended Metallocenes and *d-f* Hybrid Complexes




Hyun-Min Lim

Wolfson College

University of Oxford

A Thesis submitted for the degree of

*Doctor of Philosophy*

Hillary Term 2022

Copyright (©) Hyun-Min Lim 2022. All rights reserved.

# Abstract

The lanthanides are widely used in a variety of applications ranging from the materials science of magnets to the development of imaging agents for biomedical diagnosis and drug discovery assay. These exploit the fundamental properties of the lanthanides and focus on the behaviour of lanthanide (III) species with partly filled f-orbitals. Gadolinium complexes have become the contrast agents of choice for magnetic resonance imaging, while luminescent complexes of other lanthanides (particularly europium and terbium) play a key role in display technologies and ultrasensitive bioassay. Early work on such systems focused on simple mononuclear complexes, but the last twenty-five years have witnessed rapidly increasing interest in the behaviour and exploitation of multi-nuclear and multi-metallic complexes, both f-f and d-f heterometallic systems can be prepared by using kinetically stable building blocks to access more complicated architectures.

This thesis explores how d-f hybrid complexes can be prepared and how their properties can be exploited. The research targets on identifying three redox active systems which are ferrocene derivatives and bridging ligands that can incorporate d-metals such as ruthenium chromophores.

Chapter 1 discusses the fundamental principles of the chemistry and photophysics of lanthanides including the sensitisation mechanisms for lanthanide luminescence and the physical and chemical properties that can be derived from spectroscopic analysis. Previously reported d-f heterometallic systems are discussed in this chapter, with a particular focus on metallocene, rhenium and ruthenium.

Chapter 2 discusses the effect of direct and indirect electronic communication between ferrocene and lanthanide centres on the sensitisation of luminescence. This chapter explores studying the kinetic stability of metal centres through electrochemically induced redox cycles using CV, UV-Vis, and luminescence emission measurements. This chapter exploits earlier work on ferrocene derivatives but extends the possibilities for electron transfer and electronic communication by using bridging ligands that provide a path for exchange interactions between the two metal centres.

Chapter 3 discusses d-f compatible phenanthroline ligand and explains their potential as a bridging ligand for ruthenium and osmium incorporation, as well as the observations made during the attempted synthesis of phenanthroline bridging ligand.

Chapter 4 discusses the pH sensitivity of hydroxyphenacyl-DO3A and its potential as a bridging ligand for the incorporation of zirconocene chromophore. This chapter consists of an investigation in the effect of pH change on the physical properties of hydroxyphenacyl-DO3A and describes its suitability for use in biological systems and in pH sensing.

Chapter 5 draws general conclusions which describe the redox activity or pH sensitivity of lanthanide complexes incorporating different ligands and their feasibility to be used in biological media, while Chapter 6 provides experimental detail.

# Content

Abstract ..... i

Content ..... iii

Abbreviations ..... vi

Acknowledgement ..... xi

Chapter 1. Introduction ..... 1

1.1. Photophysics of Lanthanide Ions and Complexes. ..... 1

1.1.1. Spin-Orbit Coupling ..... 2

1.1.2. Electronic Configuration of the Ln(III) Ions ..... 3

1.1.3. Probabilities of *f-f* Transitions ..... 4

1.2. Sensitisation of Lanthanide Complexes ..... 5

1.2.1. Antenna Effect ..... 5

1.2.2. Quenching and Quantum Yield ..... 10

1.3. NMR and Other Spectroscopic Techniques ..... 13

1.3.1. Challenges in Luminescence Measurement and Interpretation ..... 14

1.3.2. Paramagnetic NMR Characteristics ..... 14

1.3.3. Lanthanide Coordination Geometries ..... 18

1.3.4. Relaxivity ..... 21

1.4. *d-f* Heterometallic Complexes ..... 22

1.5. Chemistry of Metallocenes ..... 27

1.5.1. Structure, Bonding and Uses of Metallocenes.....27

1.5.2. Ferrocene-Lanthanide Complexes and their electrochemical properties .....32

1.5.3. Other Applications of Metallocenes .....35

1.5.4. Effect of pH on lanthanide complexes .....36

1.6. Aim of the research.....39

Results and Discussion.....41

Chapter 2. Ferrocene *d-f* Heterometallic Complexes and Their Electrochemical Behaviour 42

2.1. Self-Assembly of Ferrocene Derivatives to Ln.DO3A.....45

2.2. UV-Vis and NMR Spectroscopy Analysis of Ferrocene-Lanthanide complexes .48

2.3. Electrochemical and Spectroelectrochemical Studies of Ferrocene-Ln Complexes 53

Chapter 3. *d-f* Compatible Phenanthroline Complexes.....74

Chapter 4. Hydroxyphenacyl-DO3A as a Bridging Ligand and its Potential for Bioassays 84

4.1. Synthesis and Spectroscopic Analysis of Hydroxyphenacyl-DO3A .....84

4.2. pH-Study of Hydroxyphenacyl-DO3A.....87

Chapter 5. Conclusion and Further Work.....96

Chapter 6. Experimental.....98

6.1. Experimental Procedures and Conditions.....98

6.1.1. NMR Spectroscopy .....98

6.1.2. MS ..... 99

6.1.3. Absorption and Luminescence Measurements ..... 99

6.1.4. Reagents and Solvents Preparation ..... 100

6.1.5. Dialysis, Centrifugation, TLC and Column (flash) Chromatography ..... 100

6.1.6. pH Meter and Buffer Preparation ..... 101

6.1.7. HPLC ..... 102

6.2. General Methods ..... 103

6.2.1. General Procedure 1: Lanthanide Complexation ..... 103

6.2.2. General Procedure 2: Deprotection of acid groups ..... 103

6.2.3. General Procedure 3: Attachment of DO3A to a ligand ..... 104

6.3. Synthetic Methods ..... 104

6.3.1. Products and Intermediates used for Luminescence Studies ..... 104

6.3.2. Ferrocene-related Products and Intermediates ..... 107

6.3.3. Phenanthroline-related Products and Intermediates ..... 111

6.3.4. Hydroxyphenacyl-related Products and Intermediates ..... 119

References ..... 124

Supplementary Data ..... 141

# Abbreviations

| | |
|---|---|
| a.u. | Arbitary unit |
| BET | Back energy transfer |
| bpy | Bipyridine |
| Br | Bromine or Bromide |
| bs | Broad singlet |
| Ce | Cerium |
| CE | Counter Electrode |
| CHES | N-Cyclohexyl-2-aminoethanesulfonic acid |
| Cl | Chlorine or Chloride |
| CO | Carbonyl |
| Cp | Cyclopentadienyl |
| CV | Cyclic Voltammetry |
| d | Doublet |
| DCM | Dichloromethane |
| DMF | Dimethylformamide |
| DMSO | Dimethylsulfoxide |
| DO3A | 1,4,7,10-tetraazacyclododecane-1,4,7-triacetic acid |
| DO3A-tBu | Tri-*tert*-butyl 1,4,7,10-tetraazacyclododecane-1,4,7-triacetate hydrobromide salt |
| DOTA | 1,4,7,10-tetraazacyclododecane-1,4,7,10-tetraacetic acid |
| DOTA-tBu | Tetra-*tert*-butyl 1,4,7,10-tetraazacyclododecane-1,4,7,10-tetraacetate hydrobromide salt |
| Dy | Dysprosium |
| δ | Chemical shift |

| | |
|---|---|
| ESI-MS | Electron spray ionisation mass spectrometry |
| Er | Erbium |
| Eu | Europium |
| Eu-DO3A | Europium 1,4,7,10-tetraazacyclododecane-1,4,7-triacetic acid |
| Eq | Equivalent(s) |
| Fe | Iron |
| FRET | Förster resonance energy transfer |
| Gd | Gadolinium |
| Gd-DO3A | Gadolinium 1,4,7,10-tetraazacyclododecane-1,4,7-triacetic acid |
| h | Hour(s) |
| HEPES | 4-(2-hydroxyethyl)-1-piperazineethanesulfonic acid |
| IR | Infrared |
| ISC | Intersystem crossing |
| L | Ligand |
| LIS | Lanthanide induced shift |
| LMCT | Ligand to metal charge transfer |
| Ln | Lanthanide |
| $\lambda$ | Wavelength |
| $\lambda_{em}$ | Emission wavelength |
| $\lambda_{ex}$ | Excitation wavelength |
| $\lambda_{max}$ | Wavelength at maximum intensity |
| La | Lanthanum |
| Lu | Lutetium |
| m | multiplet |

| | |
|---|---|
| M | Mola ratio, mol/L |
| MALDI | Matrix assisted laser desorption and ionisation |
| MES | 2-(N-morpholino)ethanesulfonic acid |
| MLCT | Metal-to-ligand charge transfer |
| MRI | Magnetic resonance imaging |
| MS | Mass spectrometry |
| *m/z* | Mass-to-charge ratio |
| Nb | Neodymium |
| NBS | *N*-bromosuccinimide |
| nm | Nanometre(s) |
| NMR | Nuclear magnetic resonance |
| O | Oxygen |
| OCP | Open circuit potential |
| Os | Osmium |
| ppm | Parts per million |
| Pr | Praseodymium |
| Φ | Quantum yield |
| q | Quartet |
| *q* | Number of bound solvent molecule(s) |
| r | Distance or bond length |
| rt | Room temperature |
| $r_t$ | Retention time |
| Re | Rhenium |
| RE | Reference electrode |

| | |
|---|---|
| $R_f$ | Retardation factor |
| Ru | Ruthenium |
| s | Singlet |
| SAP | Square antiprism |
| Sec or s | Second(s) |
| Sm | Samarium |
| $S_0$ | Lowest singlet state |
| $S_1$ | First excited singlet state |
| t | Triplet |
| Tb | Terbium |
| TFA | Trifluoroacetic acid |
| THF | Tetrahydrofuran |
| TLC | Thin Layer Chromatography |
| TRIS | 2-amino-2-hydroxymethyl-propane-1,3-diol |
| TSAP | Twisted square antiprism |
| $T_1$ | Spin-lattice or longitudinal relaxation time |
| $T_2$ | Spin-spin or transverse relaxation time |
| UV | Ultraviolet |
| UV-Vis | Ultraviolet-visible spectroscopy |
| v/v | Volume per volume |
| w/v | Weight per volume |
| WE | Working electrode |
| Xe | Xenon |
| Yb | Ytterbium |

| | |
|---|---|
| Yb-DO3A | Ytterbium 1,4,7,10-tetraazacyclododecane-1,4,7-triacetic acid |
| Zn | Zinc |

# Acknowledgement

I would like to thank my supervisor, Prof. Stephen Faulkner, for all the support and guidance and for being the best supervisor ever (except that he's too popular so he's too busy).

I would like to thank everyone from Faulkner group for being so supportive. I would like to especially thank Grace (for giving me hugs when I needed them the most), Carlson (you are one of the best chemists I've ever seen), Marie (congrats, mademoiselle, you survived both me and Andrew at the same time), Kezi (miss you), Debs (for listening to my pathetic whining and moaning), Dani (I am sincerely grateful for your help and kindness, king of the column!), Qidian (for having long lunches with me), Emily (for being cute), Shitong (I love your laugh and you know I love you right), Simon (for having silly jokes with me) and others. I am not sure if I would be able to be a part of such a great group again in my life. I would like to thank Grace, Carlson and Debs again for proofreading this thesis.

I would like to thank Dr. Nick Rees for NMR training and all the help in NMR data analysis, especially for $T_1$ relaxivity measurements. I would like to thank the MS facilities staff for their help in MS training and MS service for accurate mass spec.

I would like to thank Prof. Kylie Vincent, Dr. Ting Chen and Dr. Patricia Rodriguez-Macia for helping me with electrochemistry setup and basically giving me free lectures on the basics of electrochemistry. I would like to especially thank Dr. Patricia Rodriguez-Macia for proofreading this thesis. I am grateful for all the support inside and outside of the lab, despite the results we got.

I would like to thank my best friends, Cheryl and John for always being next to me and cheering me up even though you are going through a lot yourselves. Especially Cheryl, thank you for accepting me for who I am and always being there for me.

I would like to thank my family, especially my mum who was always my role model and always being supportive of my life choices. Thank you for guiding me to the right path when I am struggling and thank you for always being a good inspiration.

I cannot describe how much diverse experience I got in Oxford; both good and bad. Thank you all who helped in making a chapter in my life called Oxford D.Phil. 2017-2022. I am sure I will treasure this chapter of my life and I hope to keep in touch with everyone. I wish all the best to you all.

# Chapter 1. Introduction

This thesis explores the preparation and behaviour of a variety of bimetallic complexes that contain a lanthanide ion and also incorporate redox-active or photophysical active *d*-block binding domain. The work described focuses on the behaviour of kinetically stable systems in which the lanthanide is bound irreversibly under kinetic control, allowing exploration of the interaction of the lanthanide centre with the second metal binding domain. In the course of this thesis, we will explore how such systems can be prepared, and will show how NMR, luminescence and spectroelectrochemical methods can be exploited to establish their behaviour in detail.

## 1.1. Photophysics of Lanthanide Ions and Complexes.

Lanthanide ions (abbreviated to Ln) are *f*-block elements and display different behaviour to other elements in the Periodic Table arising from the partial occupancy of their 4f orbitals.[1]

Generally, these ions exist as $Ln^{3+}$ in aqueous solutions, with electronic configuration of $[Xe]4f^n$ (where $0 \leq n \leq 14$). *f-f* absorptions are partly forbidden (by Laporte selection rules), resulting in low molar absorption coefficients, as well as sharp-line emission in visible to near infrared regions. However, this rule can be relaxed by vibronic coupling of excited states, which causes a change in the symmetry of metal ions by molecular vibration, yet the restricted covalency of Ln(III) complexes limits vibronic coupling through low-energy vibrations.

Figure 1 below illustrates the effect of perturbations on the electron configuration of a lanthanide ion. Firstly, electron-electron repulsion of coulomb interactions splits the *f*-electron energy levels. This is then split further to sublevels by spin-orbit coupling, where

each sub-levels are separated by λ. Crystal field splitting and magnetic field splitting (Zeeman effect) will cause smaller perturbations consecutively on the electron configuration and their energy levels.

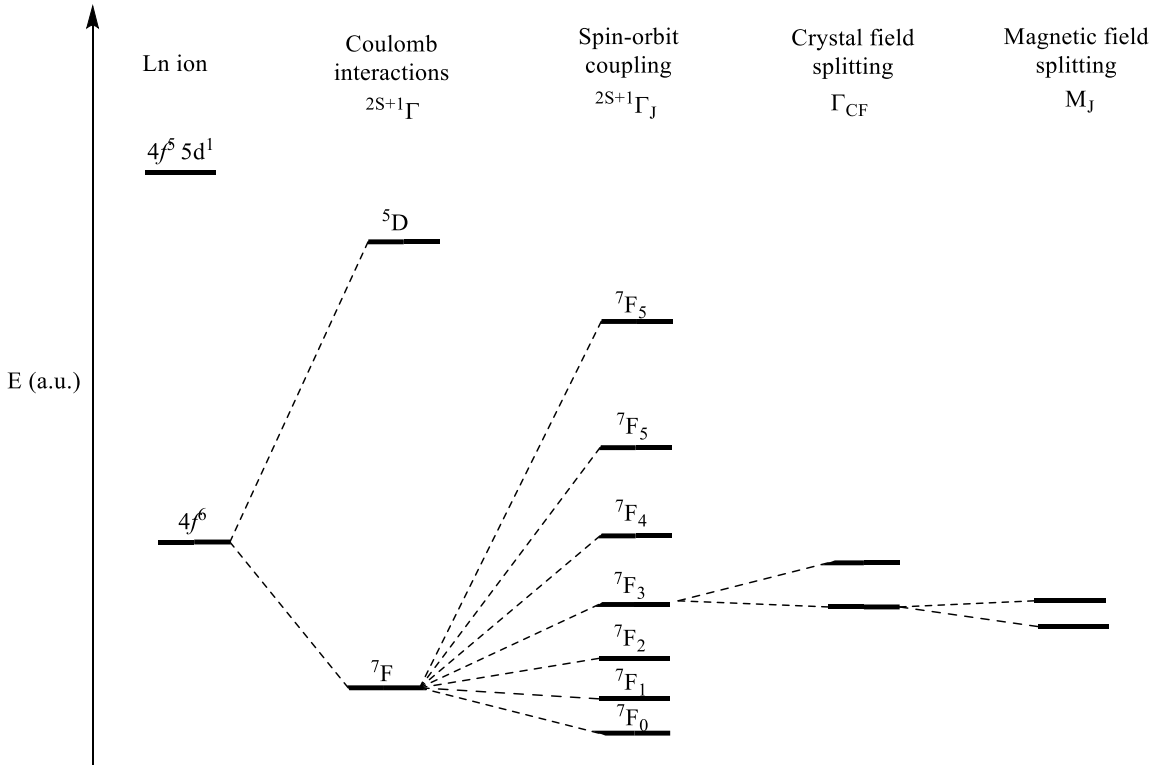



*Figure 1 – Adapted diagram to show the effect of the perturbations on the electron configuration of Eu(III) ion, where the energy units are arbitrary and not to scale.*[2, 3]

### 1.1.1. Spin-Orbit Coupling

Perturbations that affects the energy levels of the lanthanide ions includes: electron-electron repulsion and electron-nucleus attraction (Coulomb interactions), spin and angular momentum interaction, the crystal field (Stark effect), the interaction with a magnetic field (Zeeman effect) and spin-orbit coupling. [2]

The Coulomb interactions influence splitting of the energy level the most, precisely by $10^4$

$cm^{-1}$, and crystal and magnetic fields influences splitting of the energy level the least, precisely by $10^2$ $cm^{-1}$. For transition metals, the crystal field splitting dominates the spin-orbit coupling but this is not the case for the lanthanide ions. As lanthanides are relatively heavy, spin-orbit coupling plays a larger role than crystal field splitting, which increases the spin and angular momenta coupling. [4]

### 1.1.2. Electronic Configuration of the Ln(III) Ions

Ln(III) ions give distinctive line-like spectra derived from the isolation of inner 4f orbitals by shielding of 4f electrons from the filled 5s and 5p orbitals.[5] The 4*f*-electrons are generally not involved in covalent bonding and its lack of crystal field effect results in the weak absorbances and emission of *f-f* transitions. [4, 6] As described before, J levels split by Coulombic interactions and further split into sublevels by spin-orbit coupling as well as small crystal field splitting by ligand donors, which leads to a complicated luminescence spectrum.

Eu(III) in particular has gained a great attention in its use as a luminescent probe. Firstly, unlike the other Ln(III) ions, Eu(III), both the ground state, $^7F_0$ and the emissive state, $^5D_0$, are non-degenerate and they are not affected by the ligand donor, thus the $^7F_0 \rightarrow ^5D_0$ transition results in a single-line peak. Such features make the Eu(III) complexes attractive as a probe for solution speciation. The atomic radii of Ln(III) decrease with increasing atomic number and therefore, early Ln(III) are larger and late Ln(III) ions are smaller retrospectively in comparison to Eu(III). [5]

Secondly, the mid-Ln(III) ions have resembling chemical properties and ionic radii to Eu(III) which makes Eu(III) suitable as a substitute for these ions.

Thirdly, Eu(III) ions have a relatively long luminescence lifetime which is also a property of Tb(III). [7, 8] Such properties allow time-gating experiments on its luminescence to improve signal sensitivity by removing short-lived fluorescence from surrounding relevant fluorophores and biological matter. [9]

Other Ln(III) ions can be split into different lifetimes and the lifetime differences are associated to the energy gap between the excited state and ground state terms of Ln(III) ions. Smaller energy gap leads to prevalence of non-radiative quenching by vibronic coupling to OH or NH oscillators from solvent or ligands which causes decrease in lifetimes and quantum yields (which is discussed further in Chapter 1.2.2).[10]

### 1.1.3. Probabilities of *f-f* Transitions

The interaction of the electric and magnetic components of the electromagnetic radiation with the *f*-electrons leads to *f-f* transitions in 4f orbital - electric or magnetic dipole transitions (ED or MD).

The ED transition corresponds to a linear movement of charge and results in reversed direction of charge through inversion and odd parity. The MD transition corresponds to a rotational movement of charge and results in unaltered direction of charge as well as its sense of rotation through inversion and has even parity. These transitions are subject to the selection rules and mostly *f-f* transitions of Ln(III) ions consists of both ED and MD transitions.

As mentioned above, there are selection rules that govern the optical transitions. The spin selection rule states that the spin of the ground and excited state need to match. This means

that many of the *f-f* transitions for Ln(III) ions are spin-forbidden due to the change in spin. However, the spin-orbit coupling affects the total spin quantum number and relaxes the spin selection rule. [2]

Similarly, the Laporte (parity) rule states that the parity between the initial and final states need to change.[11] As explained earlier, the electric dipole component has odd parity due to the reversed direction of charge through inversion. This means for the optical transition to be allowed, the electric dipole transitions must be between states of opposite parity. The electric dipole component must be combined with other components with odd parity for a *f-f* transition.[12]

## 1.2. Sensitisation of Lanthanide Complexes

### 1.2.1. Antenna Effect

While it is possible to overcome the low extinction coefficient problem through the direct excitation of the Ln ion using intense coherent light sources, often sensitisation of Ln ions occurs via indirect excitation. Sensitised luminescence is the process where absorption of light by a coordinated ligand is transferred to the lanthanide ions and these lanthanides emits light as a result. In most cases with lanthanides, the sensitising chromophore (antenna) is conjugated to the macrocyclic ligand chelating the Ln, such as tris(2-methyl-2-propanyl) 2,2',2"-(1,4,7,10-tetraazacyclododecane-1,4,7-triyl)triacetate (abbreviated to DO3A). Figure 2 illustrates the energy transfer from Antenna to Ln through a linker. Figure 2B illustrates the antenna to lanthanide centre chelated to DO3A macrocycle. The DO3A chelate is often used for two main reasons; i) to inhibit the release of free lanthanides into the

biological systems as they are similarly sized to $Ca^{2+}$ ions, which can disturb electrical nerve signalling, ii) to disturb lanthanide luminescence quenching via vibrational energy loss by surrounding media (e.g., O-H oscillators from water). After excitation of antenna, intersystem crossing occurs populate to the triplet state ($T_1$), followed by the energy transfer from antenna to the excited $^5D_J$ state of the lanthanide. This energy transfer becomes greater as the gap between the lowest $T_1$ state to Ln(III) excited state gets smaller. The lanthanide excited state can then relax via radiative or non-radiative de-activation.[13] The radiative electronic transition from the excited $^5D_J$ state to the $^7F_J$ states causes lanthanide-centred luminescent emission. [14]

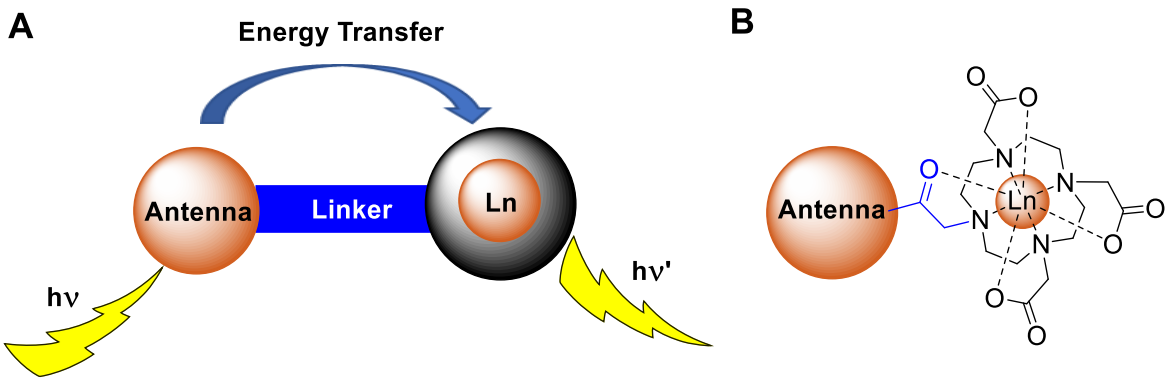



*Figure 2 - Adapted diagram to illustrate the energy transfer from antenna to lanthanide (A), and antenna conjugation to the DO3A chelating the lanthanide (B), where hν = excitation, hν' = emission.* [14]

Generally, Lanthanide complexes have two main types of luminescence; fluorescence which is the transition between states without spin change (i.e. $S_0$ to $S_1$) and phosphorescence with spin change (i.e. $S_1$ to $T_1$). These emissions occur only if the excited state can be occupied and when the non-radiative quenching pathway is blocked. These transitions are shown in Jablonski diagram as illustrated in Figure 3. Phosphorescence occurs after intersystem crossing, which is a non-radiative deactivation and occurs via either $S_1 \rightarrow T_1$ transition,

$^{1}$LMCT→ $^{3}$LMCT (ligand-to-metal charge transfer), $^{1}$ILCT→ $^{3}$ILCT (intra-ligand charge transfer), which will be discussed more in depth for *d-f* complexes in Chapter 1.4. Although it is usually assumed that the energy transfer occurs from the triplet excited state due to the favourable intersystem crossing in the presence of the heavy atom [15], several cases have been reported in which the energy is transferred from the singlet excited state directly to the emissive energy level. [16-20]

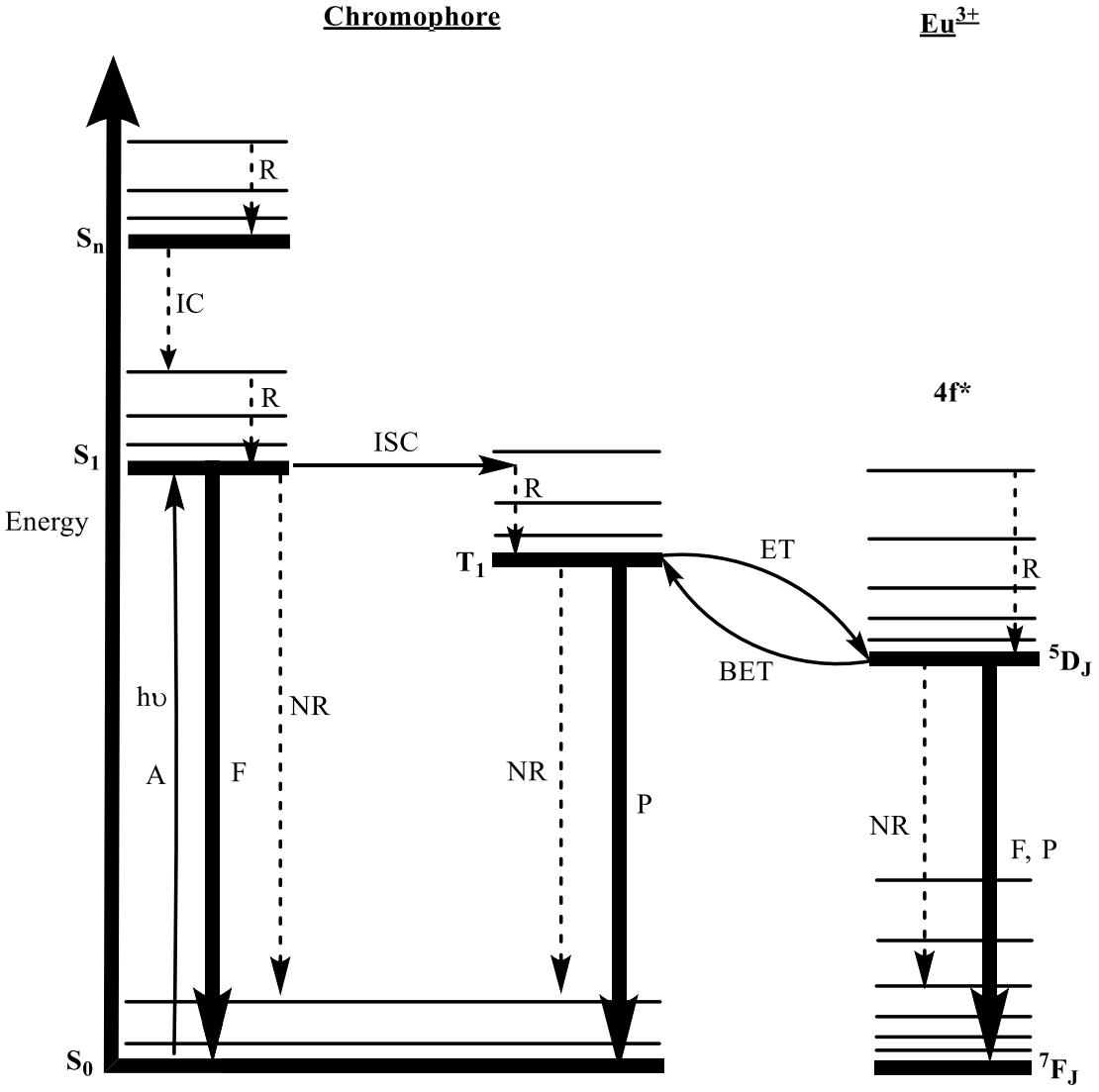



*Figure 3 - Simplified Jablonski diagram showing lanthanide energy flow and sensitisation process, where A = energy absorption, R = relaxation, F = fluorescence emission, NR = non-radiative deactivation, P = phosphorescence emission, IC = internal conversion, ISC = intersystem crossing, (B)ET = (Back) Energy transfer. Energy units are arbitrary and not to scale.*[21, 22]

As illustrated on Figure 4, energy transfer between a donor, D, and an acceptor, A, will transfer energy, usually by electron (Dexter) or dipole-dipole energy (Förster) transfer mechanisms.[23-25] Due to the lack of overlap of the 4f orbitals with the ligand orbitals, it is understood that the energy transfer for lanthanide ions mostly occurs through Förster transfer mechanism, except for Eu and Yb where Dexter and phonon-assisted mechanisms occur as Eu and Yb are easily reduced. [26, 27]

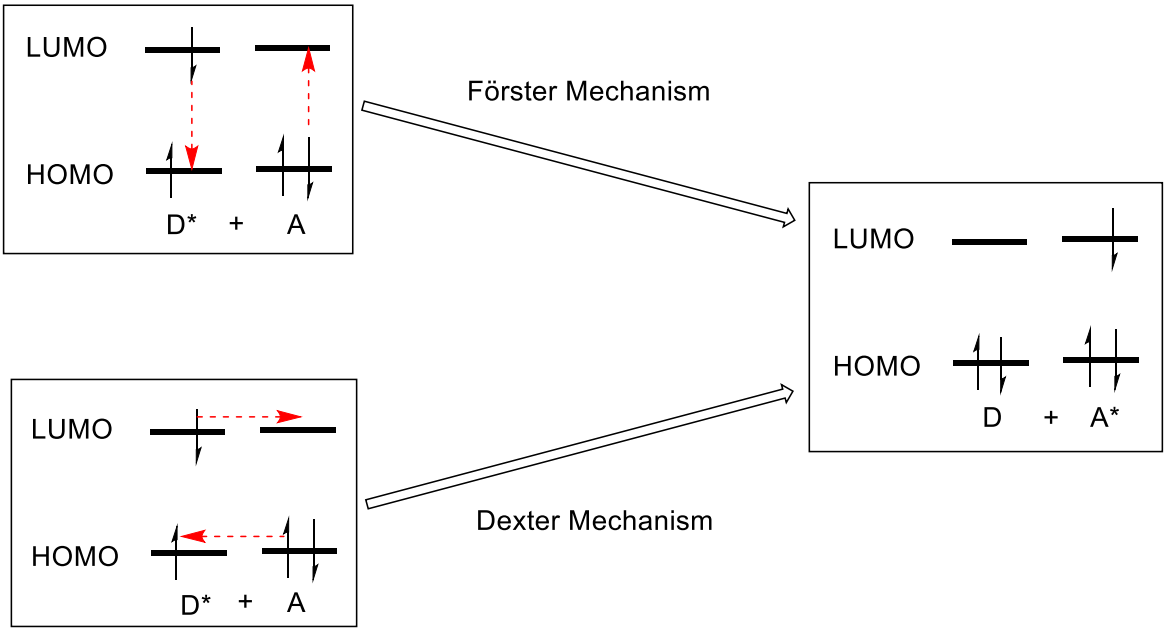



*Figure 4 - Adapted diagram of Förster and Dexter energy transfer mechanisms between donor, D, and acceptor, A.* [2]

The Förster mechanism assumes that the decrease in excitation of the doner occurs simultaneously with the increase in emission of acceptor, hence Förster mechanism can be referred as the dipole-dipole energy transfer mechanism. [23]

Yuster and Weissman [28] were one of the first groups to investigate in the energy transfer mechanism through intersystem crossing due to spin-orbit coupling with lanthanide atoms.

They discovered that change in the intensity of luminescence emission and changes of phosphorescence lifetimes are dependent upon spin-orbit coupling and magnetic moment of the lanthanide ions.[2]

Owing to their special luminescent properties described above, lanthanides have been used in various fields; 1) for light conversion techniques including cathode ray tubes,[29] plasma display lamps,[30] light emitting diode[31] and display phosphors,[32, 33] 2) for telecommunication including lanthanide-appended organic light emitting diodes (OLEDs),[34] optical fibres[35] and amplifiers,[36, 37] 3) for luminescent liquid crystals,[38] 4) for biological and medicinal analysis[39-41] including drug delivery,[42] cell[43] and tissue imaging. [44-46]

Especially, In the last decades there has been intense research in paramagnetic Ln(III) complexes because their magnetic properties, which is further discussed in Chapter 1.3. Most of these studies focused on Gd(III) chelates used as contrast agents in magnetic resonance imaging (MRI),[47, 48] which allows one to obtain images of tissues and organs.[49]

To be effective in such biomedical applications, certain criteria must be satisfied; these include a long excitation wavelength, ideally in the visible region of the spectrum, as well as good solubility in aqueous media. Above all, the complex should be thermodynamically and kinetically stable. Azamacrocyclic systems based on the DO3A moiety are generally kinetically inert and water soluble but require an aryl or transition metal chromophore to meet the other requirements. The chromophore emissive state needs to be at least 2000 $cm^{-1}$ higher than the emissive state of the lanthanide ions; europium and terbium possess high energy emissive (long wavelength excitation) state which restricts the choice of

chromophore. For systems with lower energy gap, non-radiative or radiative deactivation occurs. Thus, $Eu^{3+}$ and $Tb^{3+}$ favours the chromophores with small singlet-triplet energy difference for lanthanide sensitisation upon excitation in the visible range, while prohibiting back energy transfer from lanthanide to chromophore triplet state. There has been extensive research in a wide range of chromophores. Previously reported systems included but not limited to phenanthridine, acridones, azaxanthones and benzophenone derivatives as shown in Figure 5. [50-53]

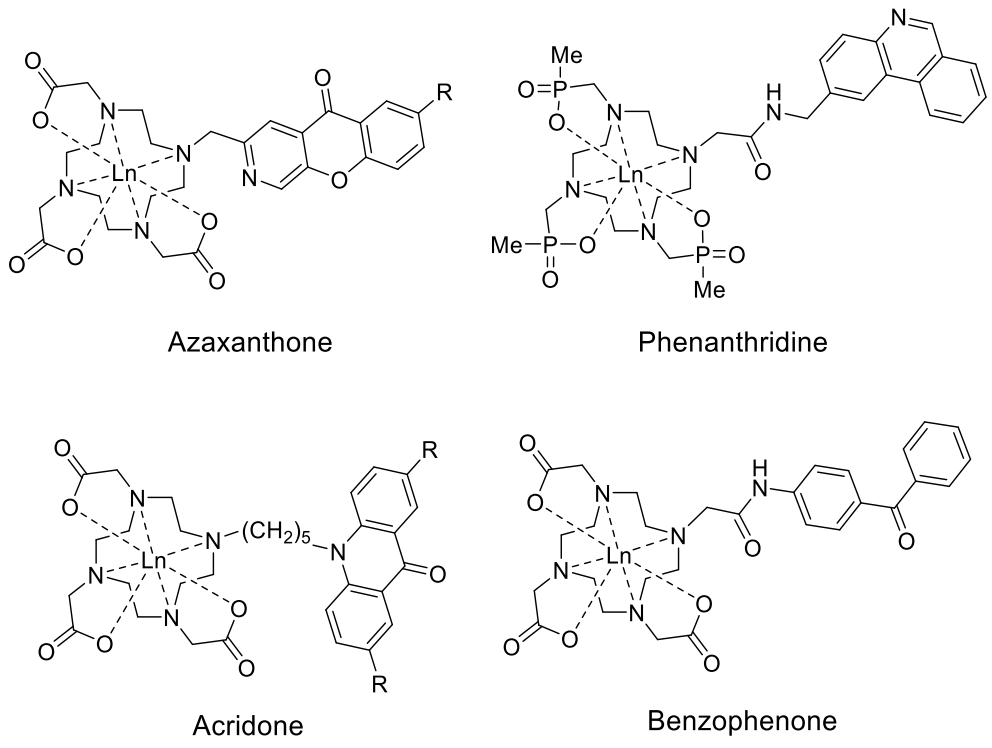



*Figure 5 - Example of previously reported systems with chromophores.* [50-53]

### 1.2.2. Quenching and Quantum Yield

When the photochemical and photophysical process occurs, a photon gets absorbed to excite a molecule. The excited state loses its energy by deactivation via four main pathways: photochemical deactivation (change in chemical structure), release of heat, photophysical

(luminescence), non-radiative quenching (loss of energy to nearby species in solution). [54]

Quenching is a deactivation process of an excited state either by an intermolecular factor such as a quencher or by an intramolecular factor such as a non-radiative interference from a substituent. Quenching can be further categorised into two types: static quenching and dynamic quenching. Static quenching occurs when the external factor, the quencher, inhibits the formation of excited state. Dynamic quenching occurs when the behaviour of the excited state is affected (such as an energy transfer) by the external factor (quencher) after the formation of the excited state. [55, 56] One of the common quenching pathways include non-radiative deactivation by O-H oscillators in aqueous solution.[14]

Quenching affects the quantum yield of photophysical and photochemical reactions, which is a measure of efficiency of light emission, expressed as a number between 0 and 1, where 1 represents 100% efficiency.[57]

The Stern-Volmer kinetic relationships allows to consider the kinetics of photophysical and photochemical deactivation and its effect on the quantum yield upon introduction of a reagent or a quencher: [58]

$$\frac{\tau_0}{\tau} = 1 + k_Q \tau_0 [Q] \qquad (1.1)$$

*Where $\tau_0$ = lifetime of excited state without a quencher, $\tau$ = lifetime of excited state with a quencher, $k_0$ = rate of quenching by a quencher (Q), and [Q] = concentration of quencher.*

The fluorophore excited state is deactivated by interaction with a species which may cause

non-radiative quenching (by O=O, O-H, O-D) which simplifies the equation for dynamic quenching to: [55, 58]

$$\frac{I_0}{I} = 1 + k_{SV}[Q] \quad (1.2)$$

*where $I_0$ = luminescence emission intensity without a quencher, I = intensity with a quencher, $k_{SV}$ = Stern-Volmer quenching constant, and [Q] = concentration of the quencher.*

In the case of the self-assembly of fluorophore to another molecule, the following equation can be derived for static quenching, given that the self-assembled system is not luminescent:

$$\frac{I_0}{I} = 1 + K_A[Q] \quad (1.3)$$

*where $I_0$ = luminescence emission intensity without a quencher, I = intensity with a quencher, $K_A$ = association constant and [Q] = concentration of the quencher.*

The plot of $I_0/I$ vs [Q] (a Stern-Volmer plot) can be plotted to determine the rate of quenching, where a straight-lined graph is typically observed; for static quenching, the gradient will decrease with higher temperatures but for dynamic quenching, the gradient will increase due to increasing collisions in solution.

When both static and dynamic quenching occur in the same solution, the Stern-Volmer relationship can be modified to:

$$\frac{I_0}{I} = \big(1 + k_Q\tau_0[Q]\big)(1 + K_A[Q]) \quad (1.4)$$

*where $I_0$ is the luminescence emission intensity in the absence of a quencher, I = intensity in*

*the presence of a quencher, $k_A$ = quenching rate constant, $\tau_0$ = excited state lifetime in the absence of a quencher, $K_A$ = association constant and [Q] = concentration of the quencher.*

A plot derived from Equation 1.4 gives a curved graph due to the gradient $[Q]^2$. In reality, the systems are more complicated with different photochemical and photophysical deactivations and the plot of the graph gives a curve approaching a plateau. Such a case can be found in Chapter 2.1, where 1:1 binding followed by a 1:2 binding occurs for self-assembly of lanthanide ion and a sensitiser.

## 1.3. NMR and Other Spectroscopic Techniques

The weak luminescence from the *f-f* state in some $Ln^{3+}$ ions can be hidden by radiative decay and emission from other substituents in the complex or quenched by non-radiative decay processes.

The physical properties such as its solubility (aqueous or non-aqueous), texture, phase of matter, crystal system (powder or crystals) dictate the design of experiments for optical emission and excitation and optimisation of external variables such as temperature and pressure.

As luminescence is often measured in differing conditions, either with coordination with multiple lanthanides, or for lanthanide complex with light emitting chromophores, luminescent emission and lifetime measurements needs to be specific spectroscopic and chemical adjustment to determine luminescence quantum yields. [59]

### 1.3.1. Challenges in Luminescence Measurement and Interpretation

Inorganic, organometallic, material sciences chemistries of lanthanide complexes with different state of matter (including powder, solid state on glasses or ceramics) requires flexibility in the administration of samples for luminescence spectroscopy. These will include not only the standard quartz cuvettes used for luminescence studies, but not limited to degassable cuvettes for inert conditions, capillary tubes, thin film cells and self-supporting films. Due to the variety of state of matter, it is often necessary to carefully design each luminescence emission/excitation measurements, instrumental settings, sample administration methods. For example, only optically transparent samples in solutions or glasses are allowed for quantum yield measurements and integrating sphere detector for opaque samples.

Optical emission spectroscopy is prone to be affected by the organic fluorophores that typically has broad background signal can mask the much weaker luminescence signal intrinsic to lanthanide ions, especially the ones with the emission band in the visible region (i.e. Tb(III) and Eu(III)). This problem is usually resolved by measuring the emission lifetimes in millisecond time scale, by benefitting from the longer-lived luminescent signal (μs scale), compared to short-lived signals (ns scale) from organic materials. Therefore, using time-resolved measurements under a short duration of pulsed light is commonly used to resolve such issues. Such optimisation can lead to more distinctive emission signal.

### 1.3.2. Paramagnetic NMR Characteristics

Diamagnetic and paramagnetic compounds can be differentiated on the basis of their

chemical and physical properties. Paramagnetic materials are attracted to external magnetic fields which causes the magnetic field induced by the paramagnetic materials to align with the external magnetic field, whereas diamagnetic materials are repelled, causing the direction of external magnetic field to be opposite to that of induced field. Paramagnetism is caused by the materials containing at least one unpaired electron. As majority of the lanthanide ions have unpaired *f*-electrons, this causes paramagnetism and gives stronger magnetic fields than the diamagnetic compounds.[60]

$^{1}$H-NMR spectroscopy of lanthanide complexes has been widely used to determine its structure in solution. Typically for a paramagnetic complex, the chemical shifts are affected by the hyperfine interactions with unpaired electron in 4f subshell and this causes the chemical shifts of nuclei to shift from their usual positions, and such shift is called the lanthanide induced shift, LIS (Δω). LIS consists of the contact and the pseudo-contact shifts and LIS are measured relative to the diamagnetic shift. The diamagnetic shifts are induced from changes in conformation, inductive and direct field effects. The contact shift ($\Delta\omega_c$) originates from a through-bond interaction of unpaired spin system and pseudo-contact shift ($\Delta\omega_p$) originates from a through-space dipolar interaction to take into account of magnetic anisotropy resulted from the magnetic field induced from unpaired electrons in Ln(III) and the nearby nuclei. [61, 62] Bleaney has derived equations regarding LIS which is the result of the contact and pseudo-contact shift. [60, 63-65]

$$\Delta\omega = \Delta\omega_c + \Delta\omega_p \qquad (1.5)$$

*Where $\Delta\omega$ = Lanthanide induced shift (LIS), $\Delta\omega_c$ = contact shift and $\Delta\omega_p$ = pseudo-contact shift.*

For asymmetric ligands, the spherical coordinates (θ, ϕ are the angles and r is the distance relating to the paramagnetic centre, C, (where C is a constant for a lanthanide state) as shown in Figure 6 can be used to calculate the ligand's pseudo-contact paramenter, G:

$$G = C\left(\frac{(3\cos^2\theta - 1) + (\sin^2\phi\cos^2 2\theta)}{r^3}\right) \quad (1.6)$$

These spherical coordinates vary depending on the temperature and nature of the complex.

The G parameter can be also expressed as below for axially symmetric complexes, where the second term becomes irrelevant:

$$G = C\left(\frac{(3\cos^2\theta - 1)}{r^3}\right) \quad (1.7)$$

The paramagnetic centre, C can also be expressed as:

$$C = \frac{-2C_J\beta^2 B_0^2}{kT^2} \quad (1.8)$$

*Where* $B_0^2$ *= second order crystal field parameter and J is derived from Russell-Saunders coupling where total angular momentum, J = L-S for early lanthanide ions with less than half-filled subshell and L+S for later lanthanides with half or more than half-filled subshell. L = total orbital angular momentum quantum number representing the energy state of a given system and S = spin quantum number.*

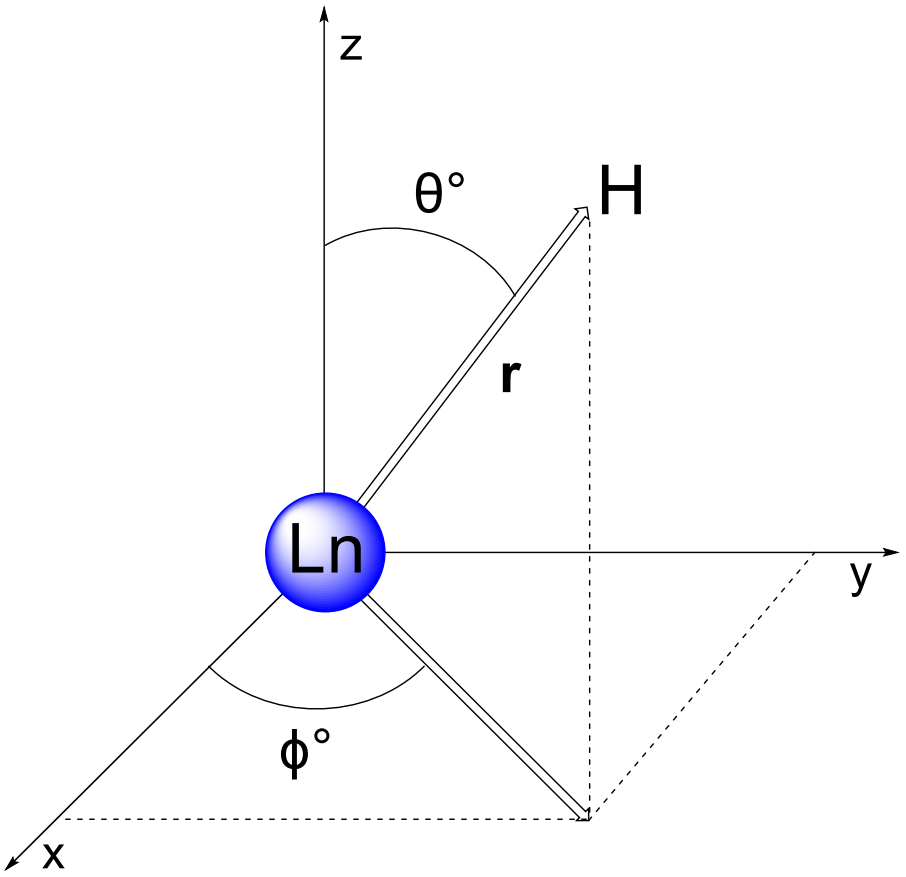



*Figure 6 - Adapted diagram to show spherical coordinates, where θ, ϕ are the angles and r is the distance of hydrogen nucleus, H, relative to the lanthanide centre, Ln.* [66]

However, either Judd-Ofelt-Mason theory, [67-69] or the Bleaney's theory [63, 70, 71] fails to give an accurate picture for optical properties and paramagnetic pseudo-contact shift of lanthanide complexes. Similarly, Bleaney's theory of magnetic anisotropy and its modifications had shortcomings to provide accurate picture of the paramagnetic NMR spectra for some lanthanide complexes, especially for systems with ligand field splitting bigger than kT, anisotropic electron distribution, [72] in addition to the non-consideration of higher order ligand field terms. Therefore, their theory and calculations neglect the optical and magnetic behaviour in *f*-element compounds is the ligand field, such as an electrostatic field induced by the ligands. The resulting energy level splitting is a dependable on the nature and ligand polarizability, the coordination geometry, the solvent, hydrogen bonding with

donor atoms of ligands. The Bleaney's theory also fails to account for the fluctuation in position of the principal magnetic axis, [73] and systems with J-mixing instead of Russell-Saunders coupling. Hence, It is important to consider the relationship between molecular structure, electric and magnetic susceptibilities as well as their anisotropies [72] to design new complexes with desired optical and magnetic properties. [3]

### 1.3.3. Lanthanide Coordination Geometries

As shown in Figure 7, Ln-DOTA exists in four major stereoisomers (2 enantiomers) which are Δ-SAP, Δ-TSAP, Λ-SAP, Λ-TSAP, where SAP corresponds to square antiprism and TSAP corresponds to twisted square antiprism geometries and Δ, Λ represents the carboxylate arm rotation. Typically, SAP is identified by its twist angle of 40°, whereas 30° is seen for TSAP. [65]

Generally, Ln-DOTA, the ninth coordination site is occupied by a water molecule, which can undergo 50 times faster exchange (where the exchange rate is $k_{ex}$) in TSAP isomers ($k_{ex}=5.32\times10^4$ $s^{-1}$ at 298 K) than in SAP isomers ($k_{ex}=2.40\times10^2$ $s^{-1}$ at 298 K). [74] It is possible to interconvert between these isomers as illustrated in Figure 7. The energy barrier for carboxylate arm rotation is much smaller for DO3A than for DOTA, meaning that isomeric interconversion is relatively fast for DO3A on an NMR timescale, which results in broad peaks, whereas relatively slow interconversion (μs timescale) of DOTA on an NMR timescale results in sharp peaks.[75, 76]

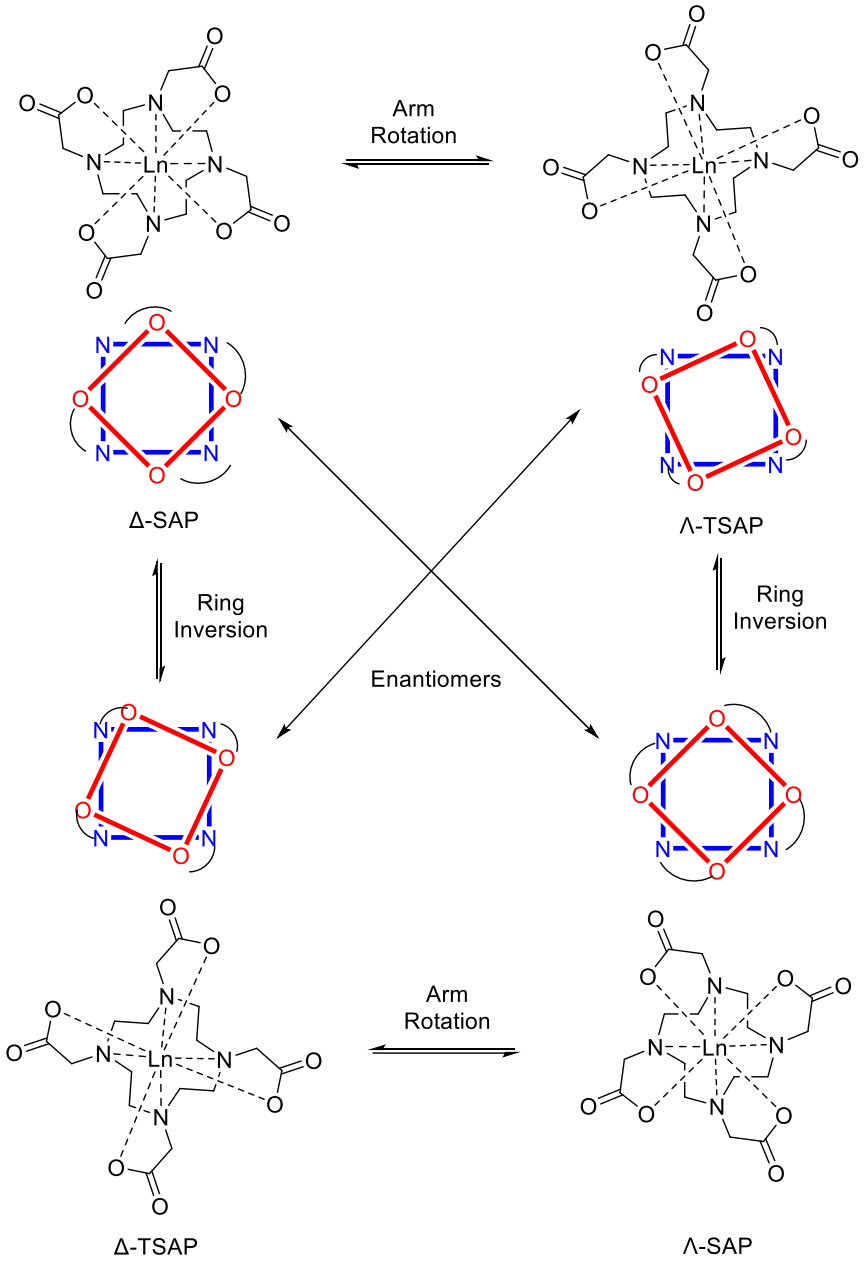



*Figure 7 - Schematic diagram of four stereoisomers of Ln-DOTA complexes and their three-dimensional polyhedral structures.*[2, 57, 65]

As lanthanide contraction gets progressively greater as you go down the series, earlier lanthanide ions in the series with relatively larger size (i.e. La(III) to Pm(III)) favours the more spacious TSAP geometry, whereas complexes containing later lanthanide ions in the series (i.e. Sm(III) to Lu(III)) favours SAP conformations. [77] The chemical shift of the NMR resonances of the axial and equatorial protons represents which of the SAP and TSAP

isomers dominates in solution. For europium complexes, $^{1}$H-NMR resonances shifting downfield by around 15 to 20 ppm represents that protons are lying relatively close to equatorial positions and the dominance of TSAP isomers, whereas those shifting downfield by around 30 to 40 ppm represents the protons are lying relatively close to axial positions and hence the dominance of SAP isomers. [63]

Complexes with macrocyclic ligands generally offer higher kinetic stability in comparison with multidentate ligands, especially octadentate ligands, due to the increased balance of the host molecules and the greater barrier to conformational change conferred by the cyclic nature of their backbones. Therefore, the exchange between the stereoisomers is much slower compared to the heptadentate ligand. In octadentate ligand, the SAP isomer is more prevalent over TSAP isomer. However, this can be easily perturbed by change in structure of system and external conditions such as temperature and the solvent system.[78]

Heptadentate DO3A complexes have a relatively lower barrier to conformational change and therefore the exchange between the SAP and TSAP isomers are much more rapid, which results in broader $^{1}$H-NMR peaks than octadentate DOTA complexes.[75] Asymmetrically substituted ligands such as DO3A lack a $C_n$ rotation axis compared to DOTA, which has $C_4$ symmetry once complexed. This complicates the evaluation of NMR data due to the loss of the axial symmetry. This is because in $^{1}$H-NMR spectra of cyclen-derived complexes, the most downfield proton environment will correspond to one of the axial ring protons. [79] In axially symmetric complexes, SAP isomer has a smaller θ to z-axis (shown in Figure 6) compared to the TSAP isomer so SAP isomer has larger pseudo-contact shift. Therefore, LIS of SAP isomer is larger for axial protons than that for TSAP isomer.[80, 81] Moreover, in DO3A

complexes, there are two water coordination sites and it has been observed that TSAP isomers ($k_{ex}$ = 3.8(±1.5) × $10^5$ $s^{-1}$ at 298 K in $CD_3CN$) have faster water exchange rate at the lanthanide centre, in comparison to the SAP isomer ($k_{ex}$ = 8.3(±2.0) × $10^3$ $s^{-1}$ at 298 K in $CD_3CN$).[81, 82]

Throughout this thesis, several examples showing these stereoisomers are shown in $^1$H-NMR spectra of lanthanide complexes (mainly Eu(III) and Yb(III)).

### 1.3.4. Relaxivity

Relaxivity is a good measure of screening the potential as a bioimaging agents. Relaxivity is the measure of the ability of magnetic compounds to enhance the water relaxation rate. In biological sample, the vast majority of the protons from NMR active nuclei are from water, which is unsuitable for conventional NMR spectroscopy. [65, 83, 84] Non-endogenous paramagnetic systems can improve image contrast and acquisition through changing relaxation rates of protons in surrounding water. [85] Lanthanide ions such as gadolinium have seven unpaired *f*-electrons with symmetric $^8$S ground state and even electron density, which means that this gives no paramagnetically induced shifts as well as slow relaxation rates.

Biological tissue can be characterised by $T_1$- and $T_2$-weighted scans, where $T_1$ and $T_2$ are the two different types of relaxation times: [65]

1. Spin-lattice or longitudinal, relaxation time, $T_1$ is the time taken for the excited protons to return to its equilibrium state (realign with the external magnetic field) after the pulse has been applied.

2. Spin-spin or transverse relaxation time, $T_2$ is the time taken for the excited protons reach equilibrium state (lose nuclear spin phase coherence). $T_2$ determines the rate at which signal fades away.

In magnetic resonance imaging, gadolinium complexes are used to provide image contrast by accelerating the relaxation of bulk water protons. Their effectiveness is measured by the relaxivity (essentially the enhancement in $1/T_1$ per unit gadolinium ion). Contrast agents with gadolinium can enhance $T_1$ weighted images, where the larger the relaxivities per mmol of gadolinium, the more effective the agent and a better image is produced.

The relaxivity $r_n$ (where n = 1, 2 for $T_1$ and $T_2$ measurements respectively) can be defined from:

$$\left(\frac{1}{T_n}\right)_{obs} = \left(\frac{1}{T}\right)_{dia} + r_n[Gd] \qquad (1.9)$$

By taking a number of $T_1$ measurements over a range of contrast agent concentrations , the relaxivity can be calculated, which is the gradient of a plot of $1/T_n$ against concentration of gadolinium. [65] In this thesis, relaxivity of gadolinium complex has been determined through a series of measurement of $T_1$ relaxation times in Chapter 4.2 to determine its suitability in biological systems.

## 1.4.*d-f* Heterometallic Complexes

Owing up to the long-lived luminescence, metal complexes has been extensively researched as imaging agents. But due to low molar absorption coefficients of lanthanide ions, chromophores with larger molar absorption were required alongside to act as an antenna to sensitise lanthanide emission, while avoiding the repopulation of the triplet. As shown in

Figure 8, absorption of energy promotes the chromophore ground state to its excited singlet state ($^1$Ch*) which sensitises the lanthanide emission through intersystem crossing following a triplet-mediated energy transfer,[86] but an alternative mechanism involving the formation of a charge transfer state from an intermediate chromophore to a lanthanide ion has been found to be a dominant pathway for sensitization of Ytterbium wherever it is thermodynamically feasible. [87]

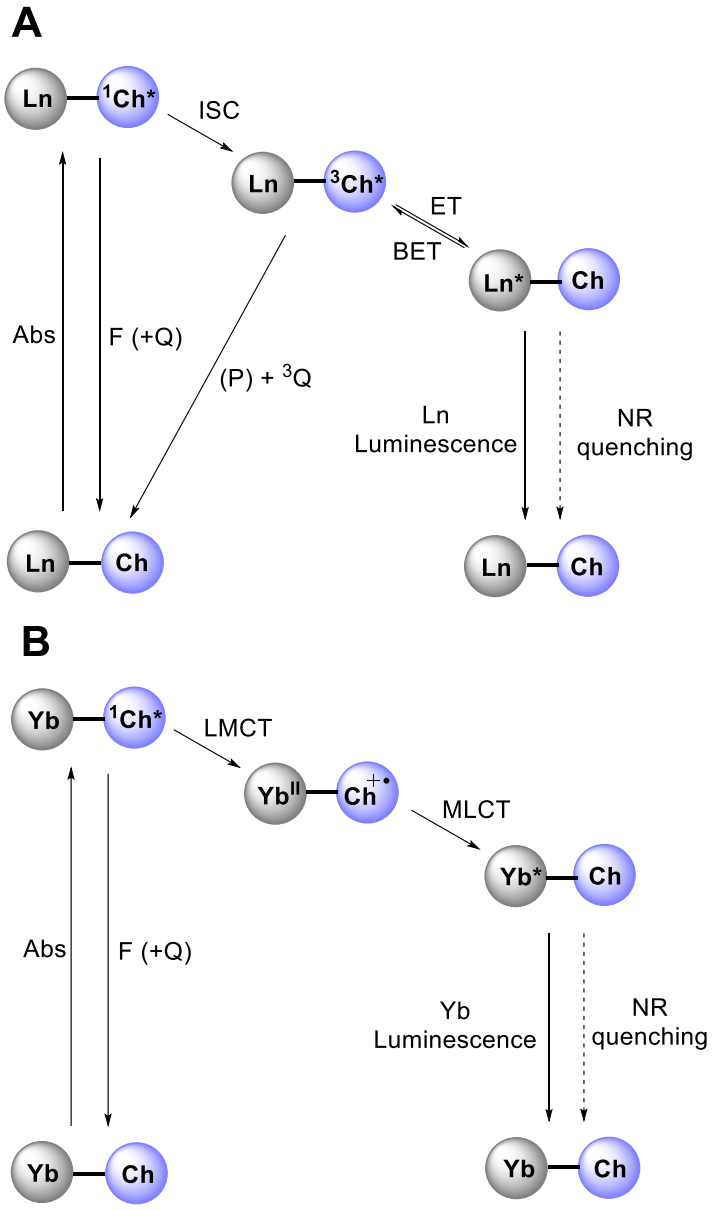



*Figure 8 - Illustration for the sensitised luminescence following formation of chromophore*

*(Ch) triplet mediated state (A) or Ligand to metal charge transfer (LMCT) (B), where ISC = intersystem crossing, (B)ET = (Back) Energy transfer, F = Fluorescence, P = Phosphorescence, Q = Quenching, Abs = Absorption, MLCT = Metal to ligand charge transfer, NR = non-radiative.* [88]

Energy transfer through the triplet mediated state meant that the choice of chromophores for Eu(III) and Yb(III) is limited to the ones with high triplet state energy. Therefore, the research has progressed to incorporate lanthanides with low emissive state due to their near IR luminescence, such as Nd(III),[89] Yb(III), [90, 91] Pr(III), [92] Er(III). [93] These lanthanides broadened the choice of chromophores to those who can absorb lower energy such as visible and red light region, while allowing the same energy transfer mechanisms as shown in Figure 8, although Yb(III) have shown to facilitate double-electron transfer mechanism where overlap between the mediated triplet state and the lanthanide-centred emissive state is poor. [27, 88, 94-97] Energy transfer from the donor to the acceptor can occur through-space (Förster mechanism) [23, 98] or through-bond (Dexter mechanism) [99] as described previously in detail in Chapter 1.2. Though both transfer mechanisms are feasible, the typical narrow absorption lines observed from lanthanide ions is likely to undergo Dexter exchange. [96, 100-102]

Particularly there has been an extensive study on rhenium or ruthenium bipyridyl complexes as a chromophore. [103, 104] Re(I)-Ln(III) complexes especially has shown to have efficient energy transfer from Re(I) to Ln(III) because the lowest electronic excited states around 2.19 eV (17,655 cm−1) of $[Re(CO)_3Cl(L)]$ are close to the excited states of NIR lanthanides.[105] Typically Re(I) and Ru(III) complexes , with kinetically stable low-spin $d^6$ configurations, have been chosen for incorporation into *d-f* bimetallic systems by its coordination to (poly)bipyridine group(s).

$[Ru(bpy)_3]^{2+}$ derivatives have shown red luminescence and is thermodynamically and kinetically stable. This typically shows very intense bipyridine absorption bands in the UV region as well as the broad MLCT peak in the visible region with $\lambda_{max}$ of 450 nm. As shown in Figure 9, the $^3$MLCT state has a distinctive emission band around 600 nm and has a long phosphorescence lifetime (1.1μs in acetonitrile) [106] for the energy transfer to occur in *d-f* complexes. In addition to its oxidising and reducing abilities at $^3$MLCT, Ru centre of $[Ru(bpy)_3]^{2+}$ can be controlled by electrochemical applications; +1.33 V for oxidation and -1.39 V for reduction, all relative to SCE in acetonitrile. [106-108] For such potential for application in electrochemical studies and ligand dependence of Ru-polypyridine systems, [54, 109] which is also applicable for lanthanide-centred emissions, Ru-polypyridine has been extensively investigated in supramolecular chemistry to see the effects of redox states in photochemical and photophysical properties. [110-112]

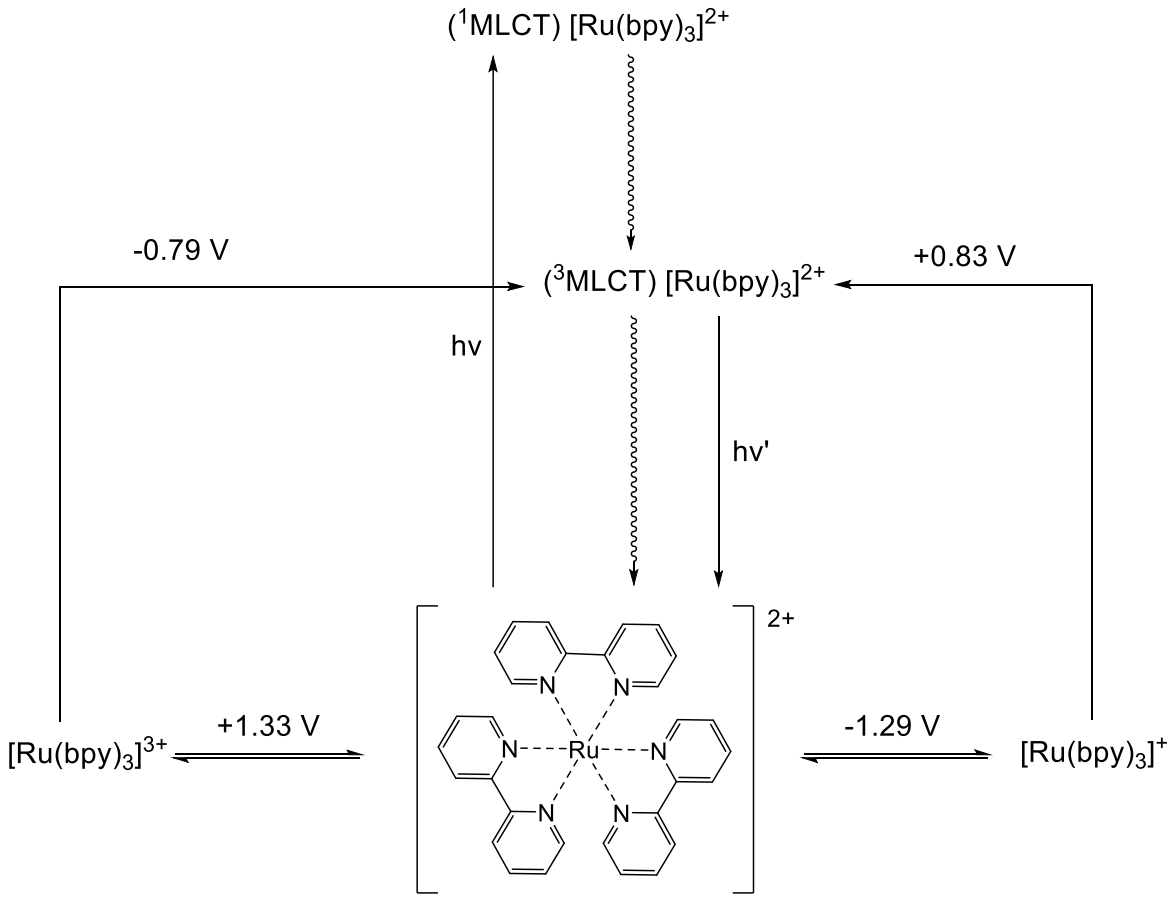



*Figure 9 - Adapted diagram of energy transfer mechanism in $[Ru(bpy)_3]^{2+}$ derivatives via*

*$^{1}$MLCT and $^{3}$MLCT states and its possible oxidation and reduction by electrochemically applied potential (V vs SCE in acetonitrile), where hv = absorption and hv' = emission.* [112]

Figure 10 shows the previously studied Re(I)-Ln(III) and Ru(II)-Ln(III) complexes in supramolecular DO3A systems by Perry et al., [96], Koullourou et al., [113] Tropiano et al., [87] Pope et al., [114] and Katell Senechal-David et al. [115]

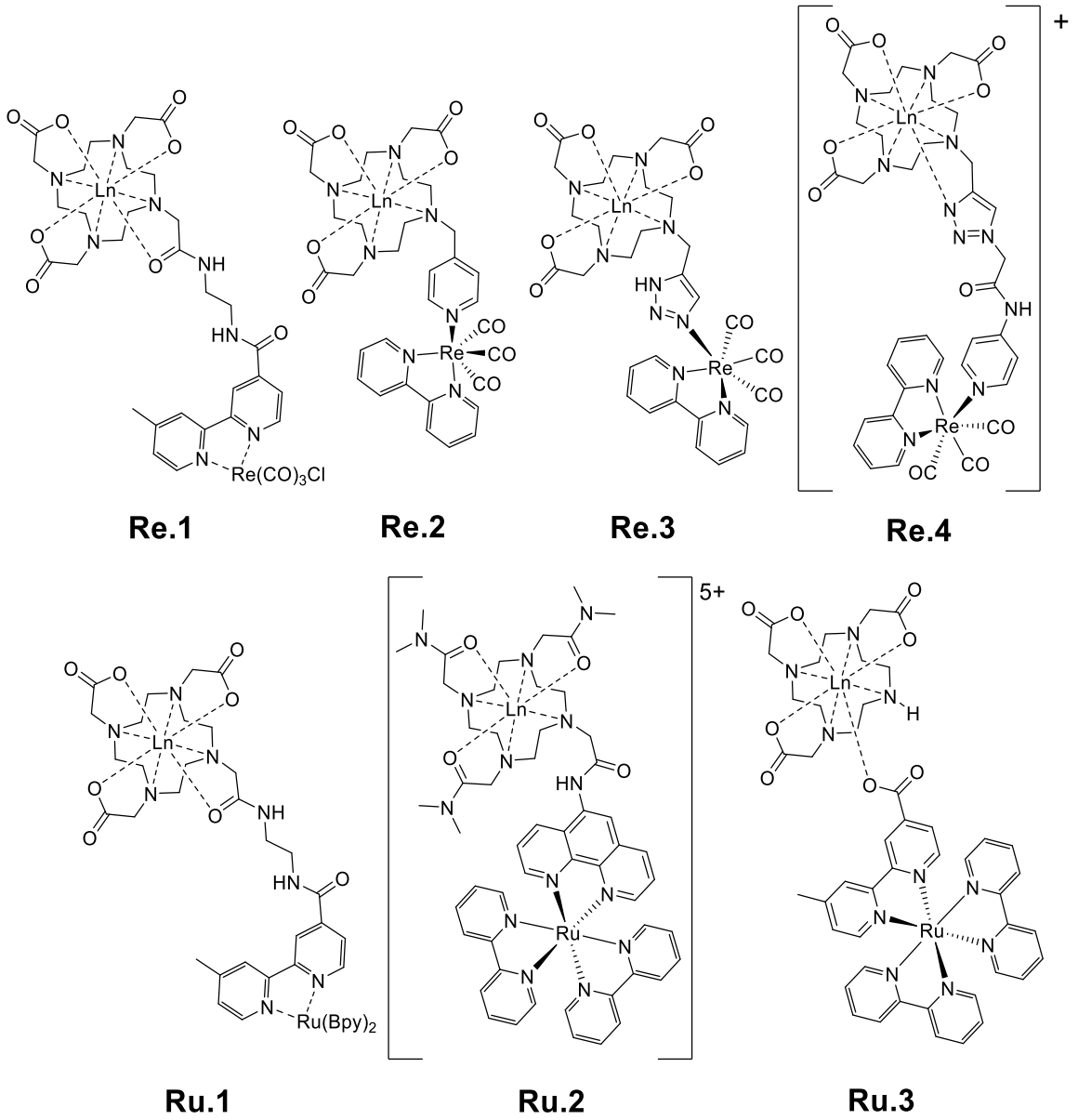



*Figure 10 - Previously reported Re-Ln and Ru-Ln complexes.* [87, 96, 113-115]

They investigated the energy transfer pathways of Re(I) and Ru(II)-polypyridine system to

sensitise lanthanide luminescence, as well as investigating the effect of a modification in spacer group or bridging ligand on the efficiency of energy transfer and the rate of the energy transfer. For **Re.1** and **Ru.1**, an alkyl spacer group separated the transition metal chromophore from the lanthanide emissive centre which slowed down the sensitisation via $^3$MLCT state.

They discovered that the $^3$MLCT and energy transfer may precede by the formation of the $^3$MLCT state (where M = Ru, Re and L = bpy) with an indication for a possible competitive deactivation pathway for the precursor state ($^1$MLCT). Also the incorporation of bridging group not only effected the distance between the *d-f* metals but also affected the energy transfer mechanisms and the relaxivity of Ln(III), especially for Gd(III); **Re.3** has shown suitable sensitisation for near IR emissive lanthanides but **Re.4** has shown suitability with promising results in showing the suitable relaxivity of Gd(III) luminescence (∼140 $s^{-1}$ $mM^{-1}$ and ∼100 $s^{-1}$ $mM^{-1}$ at 25 °C at magnetic fields 1.5 T and 3 T respectively).[116] This meant that consideration of nature of the ligand, presence of spacer group and the nature of the lanthanide luminescence are important factors in designing a *d-f* hybrids to act as a multimodal reagents in bioassays and MRI.

## 1.5. Chemistry of Metallocenes

### 1.5.1. Structure, Bonding and Uses of Metallocenes

A metallocene is a compound typically consists of two cyclopolyenyl anions sandwiching a metal centre (M) in the oxidation state +2. Closely related to the metallocenes are the metallocene derivatives, e.g. titanocene dichloride, vanadocene dichloride. Typically, well-known metallocenes consist of 2 cyclopentadienyl (Cp) anions but can also incorporate

different sized aromatic cyclopolyene rings including but not limited to cyclobutadiene, arenes, cycloheptatrienyl, cyclotatetraene, and cyclopropenium. [117, 118]

The first ever metallocene was discovered by Wilkinson and Fischer who were awarded the Nobel Prize in 1972 for their discovery in the "sandwich" compounds, first reporting the synthesis of ferrocene, bis($\eta^5$-cyclopentadienyl)iron(II). [119]

There are variations in the structure and bonding of metallocenes and especially for the Cp-M complexes and they can be categorized as:

1. $Cp_2$-M; symmetrical "sandwich" structure.
2. $Cp_2$-M-L; "bent" structure with tilted Cp rings relative to the metal centre with coordinated ligand, L.
3. Cp-M-L; One Cp coordinated to M with additional ligand, in "half-sandwich" structure.

There have been other studies on other metallocenes, which have more than 2 Cp coordinated to M centre. [118] Examples of the structures described above is shown in Figure 11.

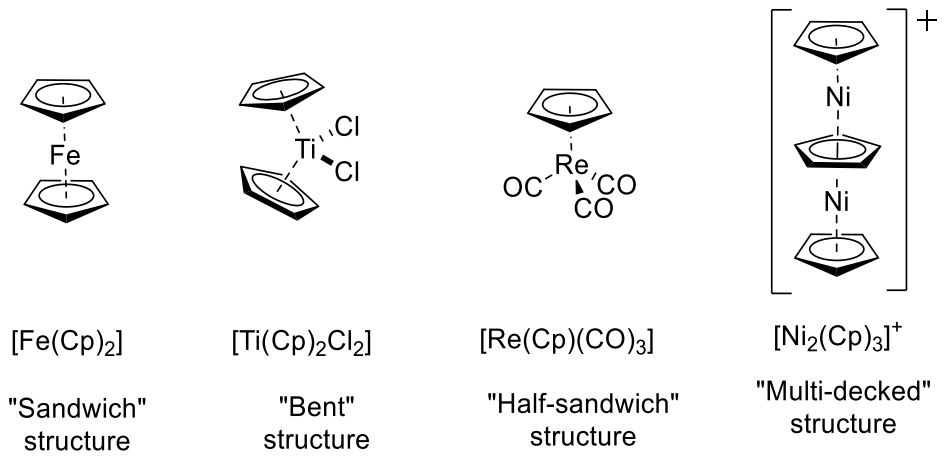



*Figure 11 - Examples of structure of M-Cp metallocene complexes.* [117]

Metallocenes incorporating Group 8 transition metals contain 18-electrons (two five π electrons from each Cp ring and eight electrons from the metal ion), [120] and when this is incorporated as metallocenes (ferrocene, ruthenocene and osmocene) are known to have a great stability and maintain their ligand-metal bonds even under harsh conditions and are feasible to undergo some transformations such as Friedel-Crafts acylation. [117]

In the most widely studied metallocene, ferrocene, the details of the bonding are not fully understood, but a qualitative molecular orbital diagram is shown in Figure 12. This diagram refers to the eclipsed ($D_{5h}$) symmetry of the complex, which in the gas phase is around 4kJ $mol^{-1}$ lower in energy than the staggered ($D_{5d}$) symmetry. As this is only a small conversion barrier, the exchange between staggered and eclipsed symmetry is occurs easily. The lower energy for the eclipsed symmetry is due to the better overlap of M and Cp rings, although the coordination of large ligand to Cp rings can cause steric hinderance and preferred symmetry will easily convert to less-hindered staggered symmetry. [117]

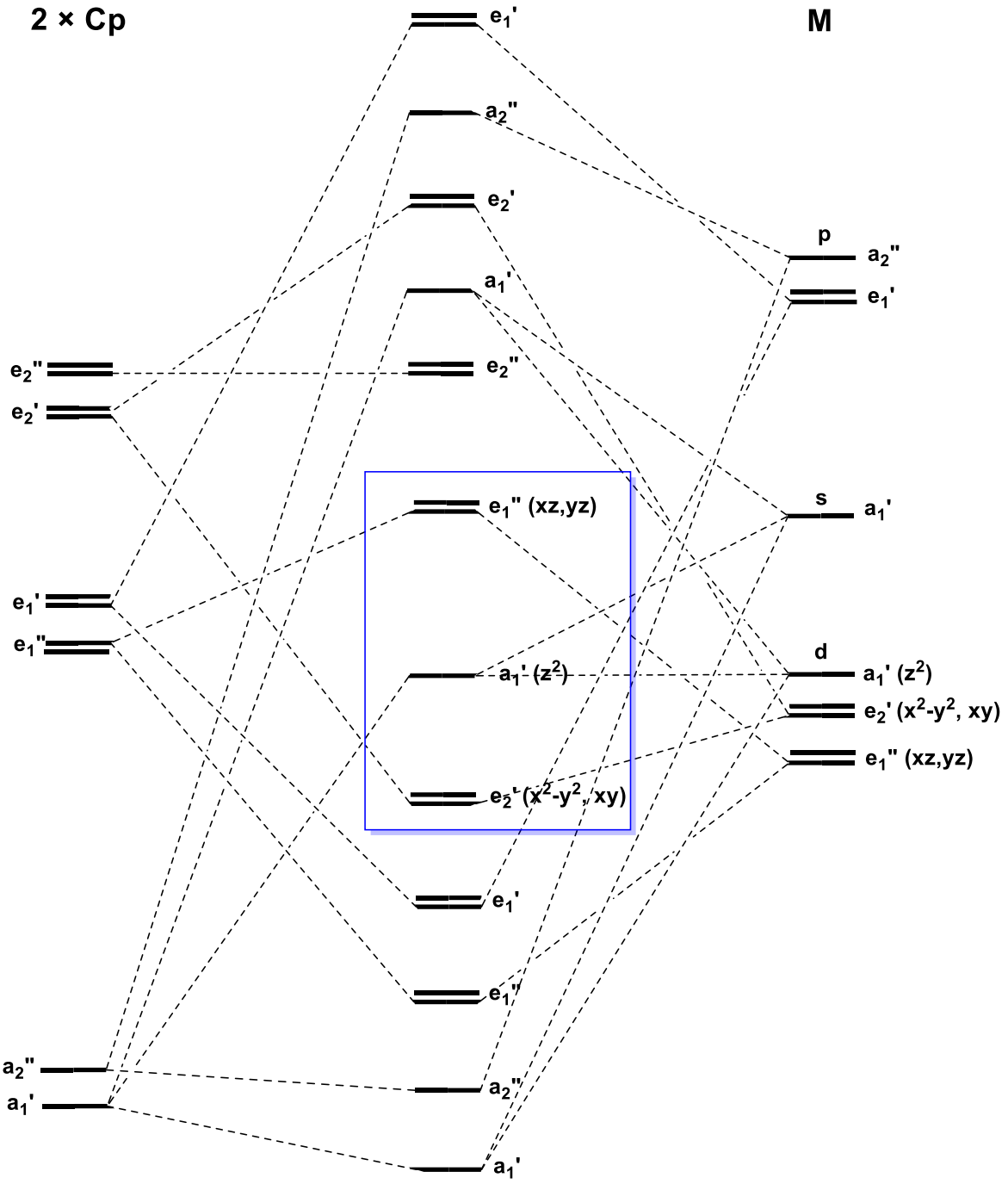



*Figure 12 – An adapted molecular orbital energy level diagram for ferrocene, with frontier orbitals shown in the blue box.* [117, 118]

The symmetry, its orbital energies and their overlap of the ligand π-orbitals and the d, s and p orbitals of metal atom can be used to predict which molecular orbitals will be formed. As shown in Figure 12, the interaction of the two $Cp^-$ ions results in splitting of the five π molecular orbitals into two sub-levels: symmetric and antisymmetric geometries relevant to

horizontal plane of $D_{5h}$ symmetry. The anti-bonding orbitals are left unpopulated for Group 8 metallocenes, and hence this explains why the compound is stable. The frontier orbitals (highlighted in blue box) and $e_1$" symmetry of ligand orbitals have the same symmetry of the $d_{xz}$ and $d_{yz}$ oribtals of the metal ion forming strong π-bonds, which again adds the stability of the metallocenes. The lower energy frontier orbital, $a_1$' composed of $d_{z^2}$ orbital is higher in energy as the metal orbitals with appropriate symmetry linear combinations are much higher in energy. However, there is little to no interaction between the ligands and the metal orbitals because the ligand π-orbitals lies in the conical nodal surface of the $d_{z^2}$ orbital of the metal atom. The $e_2$' orbitals remain essentially metal-based ($d_{x^2-y^2}$, $d_{xy}$), as their δ-overlap with the ligand $e_2$' orbital is poor. [117, 120]

The frontier orbital of a metallocene is found to be resemble to that of octahedral complexes. The $e_1$" orbital of metallocene is related to $e_g$ of octahedral complexes, and $a_1$' in combination with $e_2$' is related to $t_{2g}$ of octahedral complexes, by descent in symmetry. Thus, metallocenes also allow the high and low spin of metallocene complexes.

An important thing to note is that the frontier orbitals are neither strongly bonding nor strongly antibonding. This differs to the standard 18-electron rule, which states that thermodynamically stable transition metal compounds contain 18 valence electrons comprising of the metal *d*-electrons in addition to the electrons from the metal bound ligands. As a noble gas, Argon also consists of 18 electrons, it is known to be one of the most stable compounds with high energy barrier for oxidation. [121, 122] Although ferrocene consists of 18 electrons, there is a smaller energy barrier for the oxidation of 18-electron complex, ferrocene to the 17-electron complex, ferrocenium by loss of an electron from the non-

bonding $a_1$' orbital and metallocenes are more flexible to reduction and oxidation. Gain of an electron in the $e_1$" orbital results in 19-electron and 20-electron complex for other metallocene complexes, which results in M-C bond length changes. [117]

### 1.5.2. Ferrocene-Lanthanide Complexes and their electrochemical properties

By considering the stability of ferrocene (which is briefly described in Chapter 1.5.1) and the electron-donating nature of ferrocenyl group, ferrocene can survive relatively harsh reaction conditions allowing freedom in synthetic variations. Moreover, it is much more prone to electrophilic substitution compared to benzene due to the five π-electrons delocalised over the Cp ring. [123]

As shown in Figure 12, in 18-electron $Cp_2$ complexes like ferrocene, the $a_1$' orbital is full but the $e_1$" frontier orbital and all higher energy orbitals are empty, which is the key factor for the stability of ferrocene. The HOMO of ferrocene can be considered as being the $a_{1g}$' ($3d_z^2$ ), [124] or the $e_{2g}$ ($d_{x^2-y^2}$ , $d_{xy}$) pair. [125] The LUMO of ferrocene is derived from an out of phase π-interaction between the $d_{xz}$, $d_{yz}$ iron orbitals, and the Cp $e_{1g}$ orbitals. [126] The stability of the ferrocene molecule is largely due to the overlap of the ligand $e_{1g}$ orbitals with the $d_{xz}$ and $d_{yz}$ orbitals of the iron atom, which results in the formation of two strong π-bonds. Under substitution of the substituent to Cp rings with the π-orbital (such as acyl group), the π-orbital of the Cp ring can interact together and this lifts degeneracy of the $e_{2g}$ ($d_{x^2-y^2}$ , $d_{xy}$) orbitals, where only one of the orbitals interacts with the substituent's corresponding orbital while the other pair remains non-interacting. For ferrocene derivatives with coordination of carboxaldehyde, carboxylic acid, carboxamide substituents, $e_{2g}$ orbitals are found to be split by 0.046, 0.082, 0.065 eV respectively, and other degenerate orbitals with lower energy are

split even further with acyl group coordination to the Cp ring.[126] Moreover, carboxylate groups can create a strong coordination with Cp rings which can expand the synthetic routes of metallocenes to either bind to see the effect of carboxylate on ferrocene or can be acting as a bridging ligand to coordinate to another metal centre to create a heterometallic complexes. [127]

Because of the stability, low toxicity, distinctive electrochemical and spectroscopic behaviour, its wide application in anion sensing, asymmetric catalysis, redox systems to study enzymes, liquid crystalline compounds and non-linear optics has been studied extensively since its first discovery. The research in incorporation of a ferrocene moiety into biomolecules has taken place since the early 2000s and is still developing. [128-131]

Ferrocene has been found to be an efficient triplet and lanthanide excited-state quencher,[132] when energy transfer between metals are efficent,[133] but ferrocene derivatives also have a sensitized emission from europium complexes in early studies.[134] In addition, Ferrocene demonstrates an efficient ligand-to-metal charge-transfer transition where the extinction coefficient is highly dependent on the metal redox state. Oxidation of ferrocene generates ferrocenium, which acts as a sensitizer for the formation of the $^2F_{5/2}$ excited state of ytterbium(III), but the low-lying $^2F_{5/2}$ excited state allow the ferrocenium to quench the excited state once it has been produced. [135]

As described in Chapter 1.2, most lanthanide complexes have been shown to exhibit sensitised luminescence following triplet-mediated energy transfer,[86] but an alternative mechanism involving the formation of an charge transfer state from intermediate

chromophore to lanthanide ion has been found to be a dominant pathway for sensitization of Yb(III) and Eu(III) wherever it is thermodynamically feasible, but impossible for Tb(III) and Gd(III) due to their very negative reduction potential ($E(Gd(III) \rightarrow Gd(II)) = -3.9$ V and $E(Tb(III) \rightarrow Tb(II)) = -3.7$ V vs NHE, respectively [22]). [136] This can be exploited to achieve quenching by ferrocenium, which can display reversible electrolytic switching of lanthanide emission. The replacement of neutral amide donors with carboxylate anions in DO3A-type ligands has been found to shift the Eu(III) reduction potential to more negative values by around 95 mV per donor atom. [137, 138] The influence of the neutral amide linker (tBu-protected methylcarboxylate or Et) was studied by Morris et al., [139] through Cyclic Voltammetry (CV) measurements and found that the change in reduction potential is only minimal, whereas the negatively charged arm (such as carboxylate groups) led to a better stabilization of Eu(III). [135] In addition, ferrocene containing molecules which have the ability to bind and electrochemically sense anionic substrates have been studied extensively by Beer [140, 141]

With interesting characteristics of ferrocene, the electrochemistry of ferrocene has drawn our group's attention in particular. According to the previous work on ferrocene-appended europium complex by Tropiano, [135] the ferrocene system has shown electrochemically reversible redox processes of iron, where according to the oxidation state (Fe(II) or Fe(III)), his model could be utilised as a switch to turn on and off the luminescence of europium centre through change of the iron oxidation state. Therefore, in this thesis, other systems with direct conjugation of antenna and metal were studied to make comparisons to the ferrocene system and study further *d-f* heterometallic compounds to investigate its redox activity and communication between different spin systems. Further explanations on the corresponding results and discussion can be found in Chapter 2.

### 1.5.3. Other Applications of Metallocenes

As the metal atoms are bound tightly in metallocenes, this prevents the metallocenes from dislocating without a destruction of the molecule and thus, some metallocenes were studied to act as a label to detect its movement, especially when the metal is foreign in living organisms. For example, ferrocene has been used as a glucose sensor. [117, 142]

In addition, due to the size of cyclopentadiene rings, metallocenes have been studied on its capability as competitive enzyme active site inhibitor for cancerous cells mimicking the binding of primary aromatic molecules. [130, 142-144]

The cytostatic effect of the metallocene dihalides may be due to their competency to interact with the DNA of cancer cells,[142] which is alike the intra- and interstrand crosslinking capability for cisplatin.[145] Further details can be found from published articles.[146, 147] Inside the cell, the chloride ligands dissociate from the complex and the metal atom then can bind to any electron-rich species present, particularly by intrastrand bonding between adenine, guanine and cytosine bases of DNA. The inter- and intrastrand cross-linking of DNA develops deactivation of DNA template to result in DNA damage. Anticancer reactivity decreased with the molecular weight in both $d^0$ and $d^1$ metal-centred metallocene dihalides. Cancer cells lack DNA repair systems and they are more prone to mutations; hence they are more amenable to this kind of therapeutic approach.[143, 144]

For a suitable medicinal reagent, certain criteria must be fulfilled; “soft, acidic cation, two electron donating ligands cis to one another and a pair of labile ligands, preferably chlorides”

[130] would be suitable. The ability for DNA chelation alters as the non-bonding Cl-Cl distance or bite angle/length changes,[148] between metal and chloride ion. This is incompatible in zirconocene dichloride as their bite angle was too large for cross-linking.[130]

Titanocene dichloride ($Cp_2TiCl_2$) and vanadocene dichloride ($Cp_2VCl_2$) have also undergone clinical trials.[149] However, by their very nature, they are unsuitable to be used as drugs because of hydrolysis problems.[128, 150] Zirconocene dichloride was discovered to be ineffective for anticancer activities in the clinical trial with Ehrlich's ascites tumour. However, recently, the first effective ionic zirconocene dichloride derivative has been discovered showing cytotoxicity against human tumour cell membranes.[151]

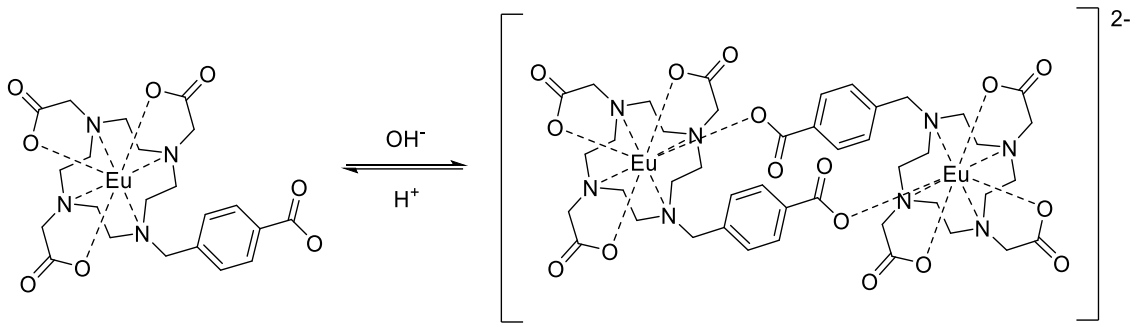
Such extensive research in biological systems proves the stability of the metallocenes and how the use of its electrochemical properties can not only used as sensors but also as fundamental studies to understand enzymic activities. This made us consider studying the effects of coordination of ferrocene to lanthanide centres by allowing direct electronic communication of *d-f* metal centres.

### 1.5.4. Effect of pH on lanthanide complexes

The effect of pH on lanthanide DO3A complexes has been studied extensively by previous members of our research group.

Firstly, Faulkner [152] has previously studied pH dependent self-association in a series of DO3A-derived lanthanide complexes with carboxylates. He reported the carboxybenzyl-

DO3A system with the carboxylic acid bridging the benzyl group to the secondary metal centre. The carboxybenzyl-DO3A linker self-assembles to form a dimer by deprotonation of an OH group of a carboxylate ligand at high pH, as shown in Scheme 1.




*Scheme 1 - pH governing the self-association of Eu complexes.* [152]

A change in pH not only affected the self-assembly but also affected the number of bound solvent (typically aqueous) molecules around the metal centre (hydration number), which can be calculated using the modified Horrock's equation below (Equation 1.10): [152]

$$q = A_{Ln}\left(k_{H_2O} - k_{D_2O} - B_{Ln}\right) \qquad (1.10)$$

where $A_{Ln}$ and $B_{Ln}$ are constants differing to each lanthanide ion and correct for inner sphere and outer sphere quenching effects respectively. For example, $A_{Eu^{3+}}$= 2 ms and $B_{Eu^{3+}}$= 25 $ms^{-1}$, $A_{Tb^{3+}}$= 5 ms and $B_{Tb^{3+}}$= 0.06 $ms^{-1}$, $k_{H_2O}$ and $k_{D_2O}$ are the observed rate constants for luminescence. [153]

In the dimer shown in Scheme 1, the calculated values of q were smaller for pH 7 or over (q = 7 at pH 8), in comparison to that at lower pH (q = 0.2 at pH 2).[152] As the carboxylate group is deprotonated at neutral or higher pH (pKa(benzoic acid) = 4.19) [154] allows the carboxylate to replace one of the water molecules bound to a lanthanide centre, whereas carboxylate

group gets protonated at low pH which is blocked to replace any bound water. For this same reason, the emission at low pH was much weaker than that at high pH. Furthermore, Faulkner has compared the relative intensities of the peaks at 595 and 616 nm upon the change in pH, which has shown a change in local environment at the lanthanide centre.

While Hill [155] has studied the influence of buffer, pH and ligand structure on the binding of dinicotinate, Sorrenson et al., [156] reported an overview of thermodynamics of self-assembly of other anions (such as isophtalate, nicotinate, benzoate, phthalate, terephthalate) to lanthanide complexes that could be be used as a biological sensor due to their pH dependence. These studies on self-assembled systems represent an important development in that they allow self-assembly processes to be used to study the properties of polynuclear lanthanide complexes. Furthermore, these systems show pH dependent self-association and thus have potential as pH sensors in which the spectrum, quantum yield and luminescence lifetime change as a result of self-assembly. This has made us consider investigating the self-assembled systems (not to mention its benefit in the rapid screening of the chromophore sensitisation ability [27, 114]) and study further effect of pH on lanthanide complexes. This trial can be found in more detail in Chapter 2.1 and 4.2.

The pH dependence of lanthanide complexes was not only limited to self-assembled systems but also covalently bound chromophore systems to a lanthanide DO3A moiety. Fisher et al., [157] specifically studied the effect of pH on the sensitisation and coordination of benzimidazole DO3A to lanthanide ions such as Eu(III), Tb(III), Yb(III). It has been found that protonated benzimidazole DO3A in acidic conditions (pKa = 4.1 for the Eu(III) complex) changed its coordination structure, not to mention its enhancement in the thermodynamic

stability in aqueous media. In acidic conditions, coordinated benzimidazole ligand dissociated from the lanthanide centre whereas q was not affected on protonation of the benzimidazole DO3A. Sparke et al., [158] have previously reported the synthesis of benzimidazole with different chelators at the benzimidazole nitrogen site. This will allow modification of the photophysical and sensitisation pathways and efficiencies by removal of the N–H oscillator as well as modification to form bifunctional chelators which will be useful for radiopharmaceuticals by introducing functional groups for targeting proteins or other biological systems. [157, 159] This has caught our attention and has encouraged us to expand our study on *d-f* hybrids to incorporate functionalisation of N-H oscillators in phenanthroline linker (between *d-f* metal centres) and study the effect of pH on the metal centre(s). This attempt is further described in Chapter 4.2.

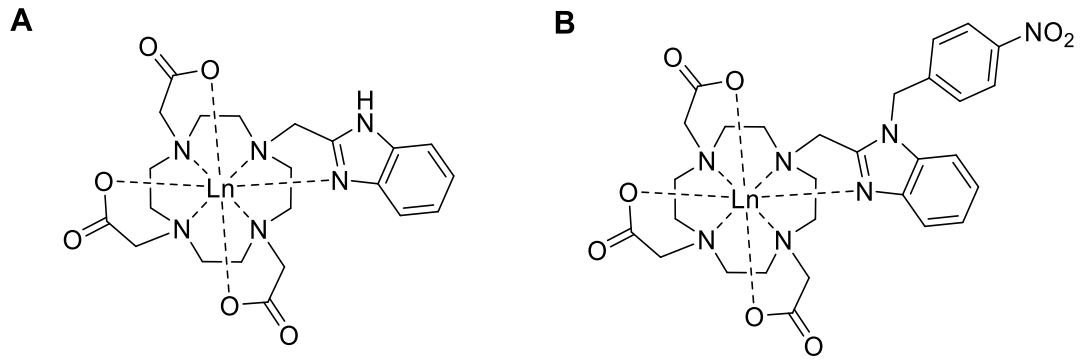



*Figure 13 - Lanthanide complexes incorporating the benzimidazole derivatives studied by Fisher et al., (A),[157] and Sparke et al., (B).[158]*

## 1.6. Aim of the research

This thesis aims to provide a clear view on how *d-f* hybrid complexes can be prepared and how their chemical and physical properties (particularly photophysical properties) can be exploited. The particular focus is on metallocenes and redox active chromophores. This study exploits earlier work on ferrocene derivatives but extends the possibilities for electron

transfer and electronic communication by using bridging carboxylates that provide a path for direct Dexter exchange between the two metal centres. The research targets three systems which are ferrocene, zirconocene derivatives and bridging ligands that can incorporate *d*-metal chromophores. Further studies on phenanthroline and hydroxyphenacyl groups as the bridging ligands were studied to understand their suitability as a bridging ligand as well as their possible functionalisation and use as pH sensors through spectroscopic analysis under different pH values.

# Results and Discussion

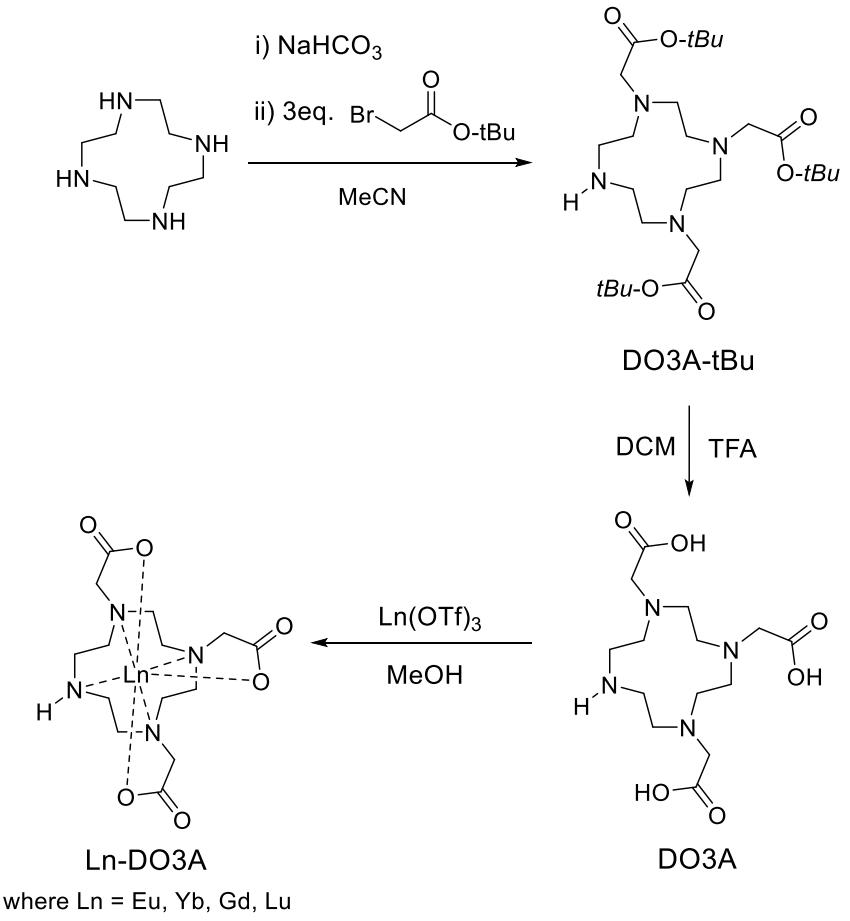
# Chapter 2. Ferrocene *d-f* Heterometallic Complexes and Their Electrochemical Behaviour

Previously, self-assembled systems, relying on thermodynamic stability, have been prepared and studied in great detail.[1, 6, 160, 161] The Faulkner group and others have exploited the formation of ternary complexes between kinetically stable lanthanide complexes and simple carboxylates to probe energy transfer, [97] and as a fast and effective means of screening chromophores for use as sensitisers of lanthanide emission. [27, 155, 162]

There have been conventional luminescence methods can be exploited in conjunction with lanthanide luminescence. In the simplest cases, a single lanthanide can be used to achieve a switchable response in combination with a transition metal complex. [163] For example, Tropiano [135] successfully developed a *d-f* hybrid of europium-ferrocene which can act as a luminescence switch that can switch-on and -off the lumiFirnescence upon electrochemical redox adjustments. In this model, a triazole group was the bridging ligand between the ferrocene and Eu-DO3A as shown in Scheme 3. Here, we investigated the effect of direct ferrocene coordination to the europium macrocycle, Eu-DO3A (shown in Scheme 2). This was examined by comparing the effect of change in redox state of Eu or Fe in a self-assembled system containing Eu-DO3A and ferrocene carboxylate, and by comparing this with a covalently linked system that allowed for Dexter exchange mediated energy transfer.

Europium DO3A was synthesised through a three-step procedure as shown in Scheme 2. The first step involved reaction of cyclen with t-butyl bromoacetate to form the triester, tri-

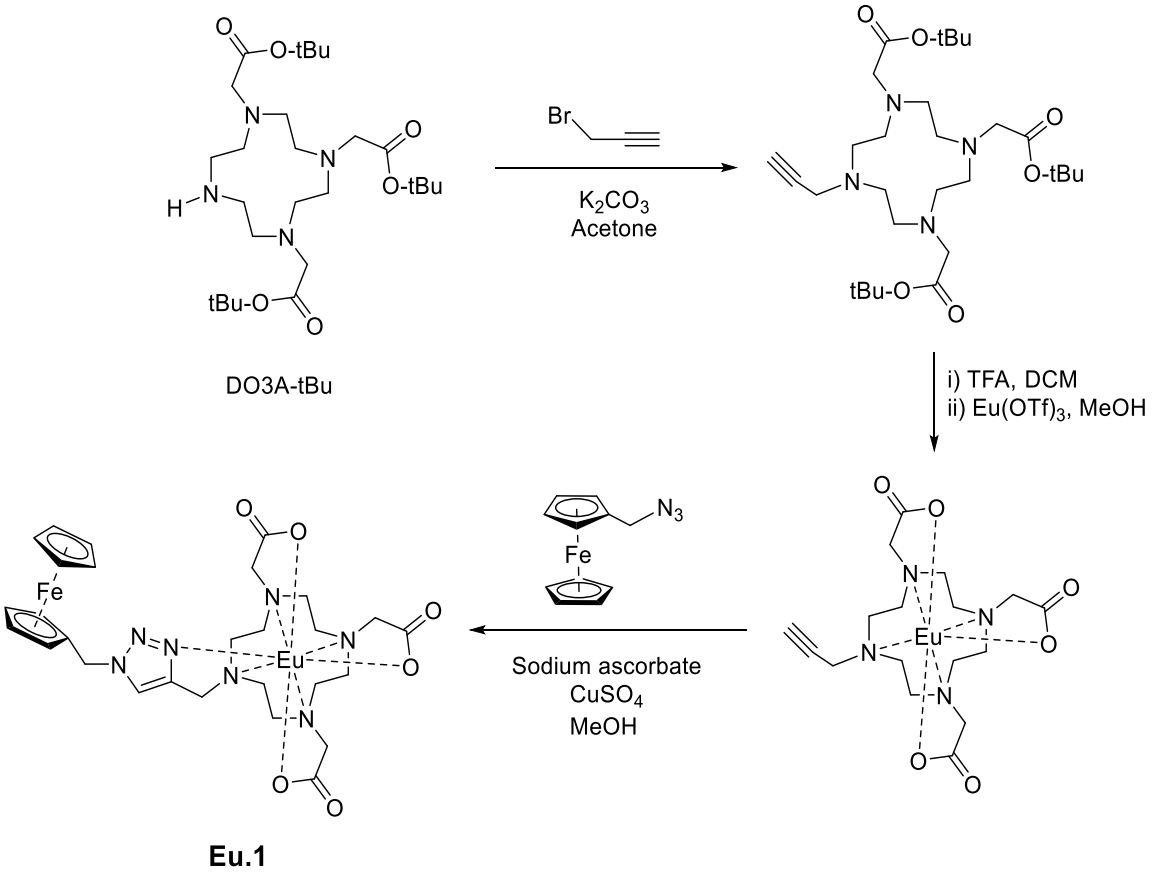
*tert*-butyl 1,4,7,10-tetraazacyclododecane-1,4,7-triacetate (DO3A-tBu). Deprotection of carboxylates using trifluoroacetic acid (TFA) resulted in the formation of DO3A. Finally, complexation of DO3A with europium triflate gave the desired europium DO3A complex. This was characterised with MS and $^{1}$H-NMR spectroscopy to match the previously studies on Eu-DO3A, and the data obtained was consistent from previously published data by Tropiano. [164]




*Scheme 2 - Simplified synthetic scheme of Ln-DO3A, where Ln = Eu, Yb, Gd, Lu.*

As shown in Scheme 3, alkylation of the DO3A-tBu with propargyl bromide yielded the protected propargyl DO3A. Subsequent treatment with TFA followed by a complexation with europium triflate yielded **Eu.1**. This was characterised with $^{1}$H-NMR spectroscopy to

match the previously reported data from Jauregui et al. [165]




*Scheme 3 – Synthetic scheme of Tropiano's triazole ferrocene Eu-DO3A,* ***Eu.1****.* [164, 165]

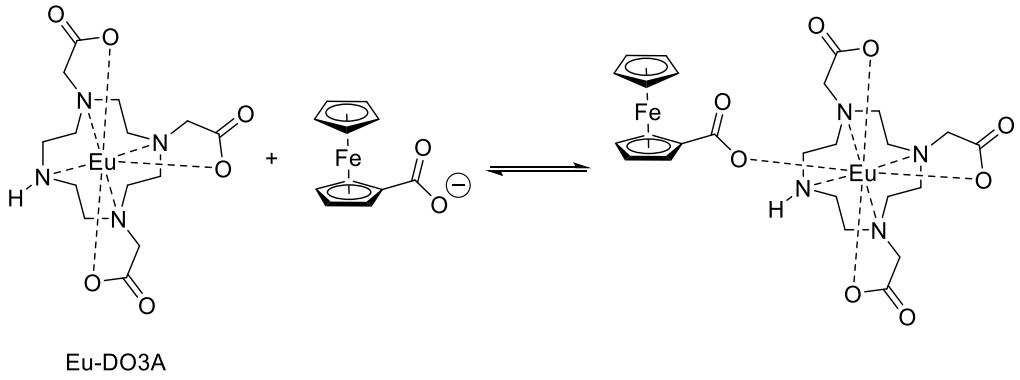
In this chapter, we explored the interaction between ferrocene carboxylic acid and Ln-DO3A to establish the relative affinity of the oxidized and reduced ferrocene carboxylate for the Ln complex and explore the communication between unpaired electrons. Then we moved to investigate the effect of redox state of metal centres in the luminescence of *d-f* hybrid.

Both the oxidation of ferrocene and reduction of Ln (III) were carried out electrochemically. Particular focus was on generating ferrocenium, the oxidised form of ferrocene, to investigate sensitising ability of ferrocenium. Ferrocenium has a doublet excited state which

act as a sensitizer for the formation of the ytterbium $^2F_{5/2}$ excited state, but this low-lying excited state gives ability for the ferrocenium to quench the excited state once it has been produced. Thus, the interactions between unpaired electrons within ferrocenium ion can be compared to ferrocene itself after coordination of ferrocene to lanthanide ions.

## 2.1.Self-Assembly of Ferrocene Derivatives to Ln.DO3A.

As mentioned above, self-assembly of *d-f* or *f-f* systems had been popular amongst scientists to screen the sensitising ability of the chromophore. The time-consuming synthetic procedures was a burden to examine the optical properties of chromophores and limited the variety of complexes to study, which shown any photophysical complications only after the final system is developed and investigated. Often complications arose from reversible energy transfer from the chromophore to Ln, [166] or from overlapped Ln emission from the tail of the metal-to-ligand charge-transfer (MLCT) emission. [167] Pope et et al. [162] previously used such an approach to assess the suitability of a range of potential sensitising chromophores. [168, 169] Self-assembly of heterometallic *d-f* complexes using a carboxylate bearing *d*-block chromophore and lanthanide DO3A complexes in aqueous solution can be used to assess donor-acceptor pairs without recourse to complicated synthetic procedures-providing a quick way to screen the sensitising ability of a chromophore of interest.




*Scheme 4 - Self-assembly of ferrocene carboxylate with Eu-DO3A.*

In this work, we extended this approach to assess a self-assembled, non-covalently linked, system (Scheme 4) that could be used to assess the possibility of through-bond sensitisation of lanthanide emission by ferrocene; allowing rapid exploration of the photophysics and spectroelectrochemistry of this *d-f* heterometallic system.

A phosphorescence titration was carried out to study the interactions and explore sensitization of Ln ions. A mixture of host (Eu-DO3A) and guest (ferrocene carboxylic acid) were added to keep the concentration of the ferrocene carboxylic acid constant. Accurate number of equivalents were calculated and administered using Gilson pipette. As shown in Figure 14, upon the titration of ferrocene carboxylic acid to Eu-DO3A in methanol, the emission intensity observed following direct excitation of the metal centre at 397 nm, changes with increasing ferrocene concentration. [132] It can be seen that the relative intensity of the hypersensitive transition ($^5D_0$-$^7F_2$, observed at 613 nm) changes relative to that of the $^5D_0$-$^7F_1$ transition at 591 nm, suggesting a change in structure at the metal centre consistent with binding the carboxylate to the lanthanide. Closer examination reveals a rapid change in ratio, followed by a recovery of the original ratio that might be suggestive of a second binding event. After addition of the second equivalence of ferrocene carboxylate, there is a plateau in the ratio of emission intensity, suggesting that only two equivalents of metal ion

can easily be accommodated, as might be expected around DO3A.

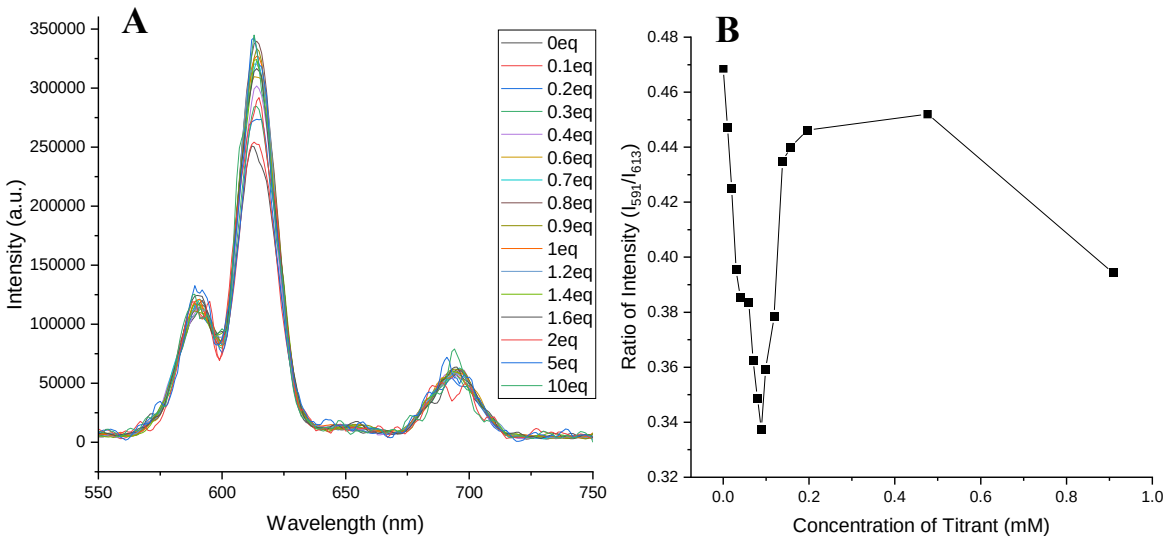
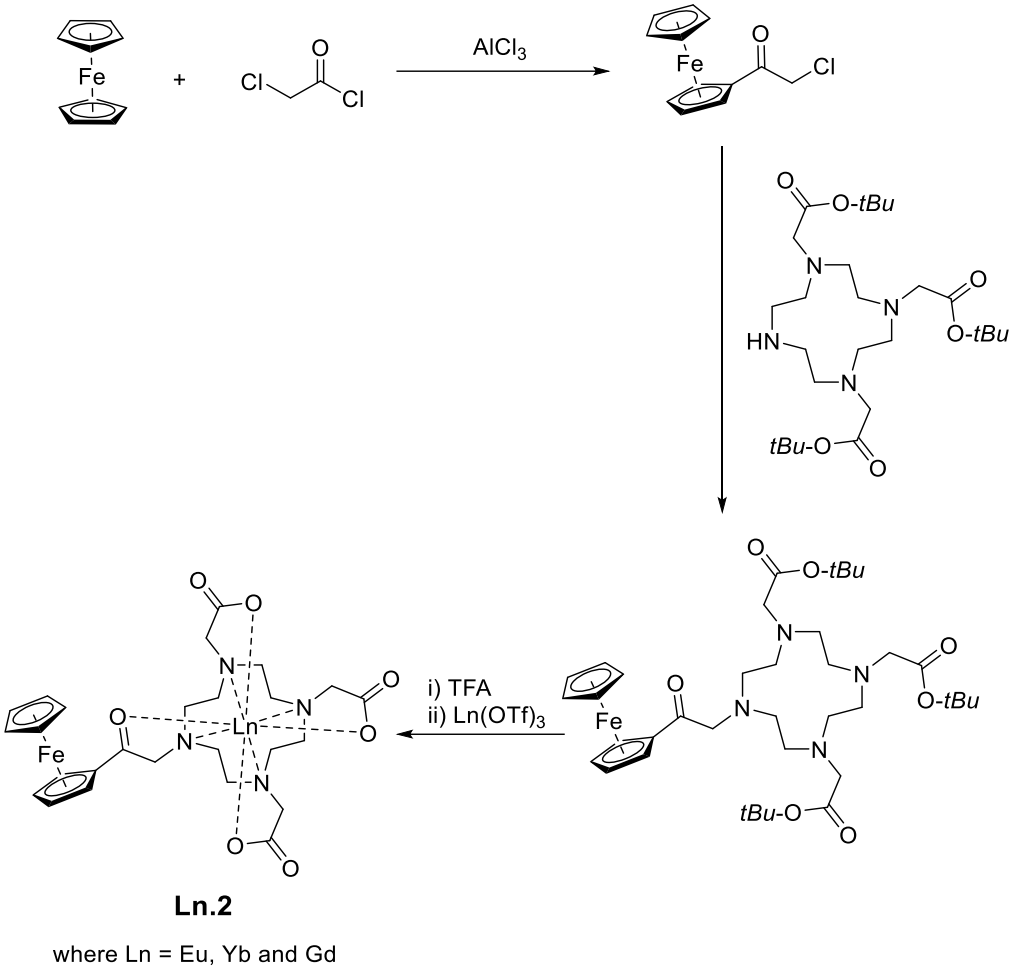



*Figure 14 - Phosphorescence emission spectra upon titration of ferrocene carboxylic to Eu-DO3A in MeOH with $\lambda_{ex}$ = 397 nm (A) and graph of ratio of intensity at 591 nm/616 nm (B); concentration of europium DO3A and ferrocene carboxylic acid used for titration was $10^{-4}$ M and $10^{-2}$ M respectively, with slit width 15 nm/10 nm for excitation and emission respectively, at 25°C.*

This indicates a strong 1:1 binding followed by weaker binding of a second carboxylate. The binding of the second carboxylate results in a decrease in observed signal, possibly as a consequence of energy or charge transfer between bound ferrocene domains. This shows the clear evidence of ferrocene carboxylate binding to Eu-DO3A and therefore further investigation into covalently-linked system (Scheme 5) was followed to study this as a comparison with non-covalent bonding.

Ln.2 was prepared by Friedel-acylation of ferrocene, with chloroacetylchloride followed by reaction with Ln-DO3A as shown in Scheme 5. Subsequent deprotection of the ester groups and reaction with lanthanide triflate salts yielded the desired lanthanide complexes.




*Scheme 5 - Synthetic route of **Ln.2** complex (where Ln = Eu, Yb, Lu and Gd).*

## 2.2. UV-Vis and NMR Spectroscopy Analysis of Ferrocene-Lanthanide complexes

As discussed previously in Chapter 1.3.3, rotation of the arms on DO3A or inversion of the DOTA macrocycle both allow interconversion between the diastereoisomers of the complex. This molecular motion gives rise to two pairs of enantiomeric species, which have square antiprismatic (SAP) and twisted-square antiprismatic geometries (TSAP) at the metal centre. These are differentiated by the position of donor atoms relative to the metal ion. In the absence of a chiral auxiliary, both SAP and TSAP isomers are observed as racemates. The relative abundance of SAP and TSAP varies with the size of the lanthanide ion and a solution state behaviour.[77]

In addition, the rate of water exchange at the axial coordination position alters greatly with the dominance of SAP or TSAP, with the latter exhibiting 50 times faster exchange rate ($k_{ex}$ = 3.8(±1.5) × $10^5$ $s^{-1}$ at 298 K in $CD_3CN$) than the SAP model ($k_{ex}$ = 8.3(±2.0) × $10^3$ $s^{-1}$ at 298 K in $CD_3CN$) as discussed in Chapter 1.3.3. [74, 81] The model can also be applied to most lanthanide complexes coordinated to the DO3A moiety, despite the loss of axial symmetry when one of the nitrogens is coordinated to a different group other than carboxylic group. Geometric differences between diastereoisomers can be explored using NMR spectroscopy, since the pseudo-contact shift facilitates the characterization between SAP and TSAP model. [79, 170]

As can be seen from Figure 15 and Figure 16, structural differences are observed across the series. These reflect changes in local geometry and crystal field. From these, it is clear that, while the europium complex exists predominantly as SAP isomers, the ytterbium complex is a mixture of SAP and TSAP forms. This is likely to be a consequence of the lanthanide contraction, with the smaller ytterbium centre giving rise to higher steric interactions in the ternary complex (and interfering significant coordination of water or carboxylate at the axial coordination site).

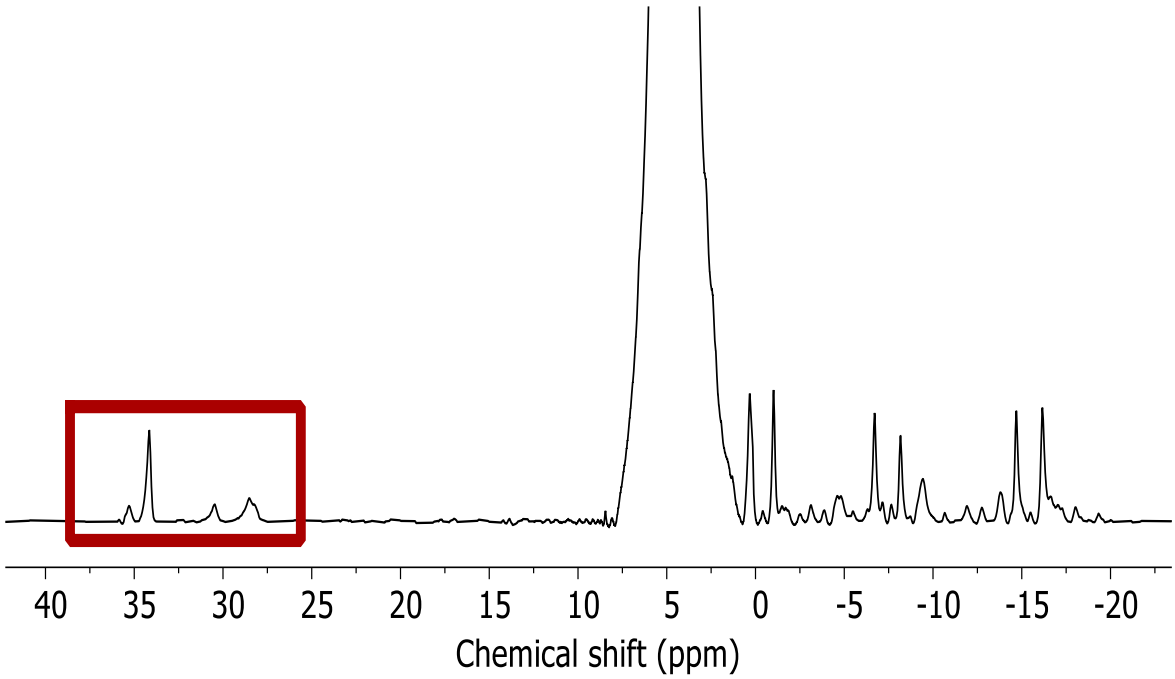



*Figure 15 - $^{1}H$ NMR (400 MHz, $D_2O$) spectrum of **Eu.2**, measured at 25°C, highlighting axial ring protons on the azamacrocycle ring and the dominance of the SAP isomer (shown in red box).*

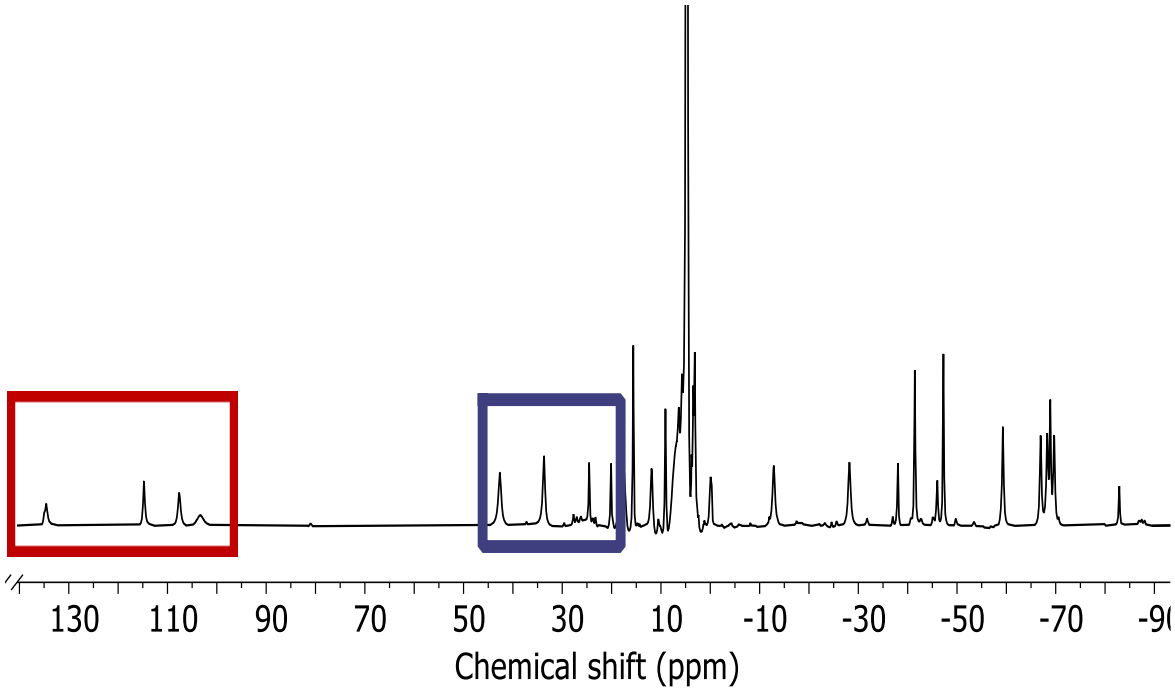



*Figure 16 - $^{1}H$ NMR (400 MHz, $D_2O$) spectrum of **Yb.2**, measured at 25°C, highlighting the axial ring protons for both SAP (red box) and TSAP (blue box) isomers.*

The UV-Visible spectra shown in Figure 17 clearly show the presence of ferrocene carboxylate DO3A attached to lanthanide ions. There are two electronic transitions; the peak at 220 nm corresponds to $a_1(\sigma)$ to $e_1(\pi^*)$ transition and the peak at 340 nm corresponds to $e_2(\delta)$ to $e_1(\pi^*)$ transition. All the complexes have these similar features as ferrocene energy absorption dominates.

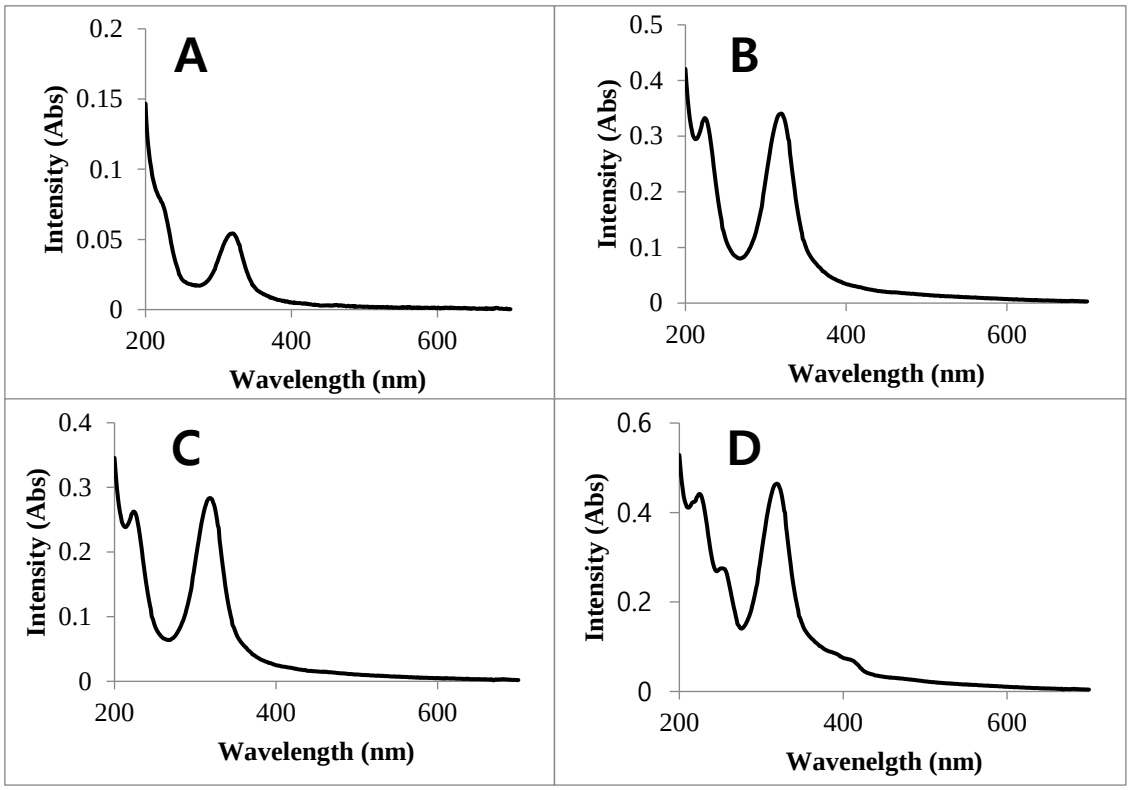



*Figure 17 – UV-Visible spectra of **Ln.2**; **Eu.2** (A), **Yb.2** (B), **Lu.2** (C) and **Gd.2** (D), all with $1\times10^{-4}$ M concentration in MeOH, measured at 25°C.*

Figure 18 shows luminescence data of ferrocene carboxylate-DO3A lanthanide complexes. For **Eu.2** with $\lambda_{ex}$ = 300 nm, typical sharp lanthanide emission peak at 616 nm are observed as well as a 591 nm peak ascribed to ferrocene carboxylate emission. These represent the direct excitation peak corresponding to the $^5L_6 \leftarrow\!- {}^7F_0$ transition, which is subsumed by the indirect excitation band, attributable to the presence of the ferrocene excited states acting as antennas. Indirect excitation through the ferrocene chromophore resulted in the

characteristic europium emission, characterised by a significantly different fine structure in the emission spectra. Transition from J=0 to J=1, J=2 and 4 are present at 591 nm, 616 nm and 691 nm respectively for **Eu.2** (Figure 18A).

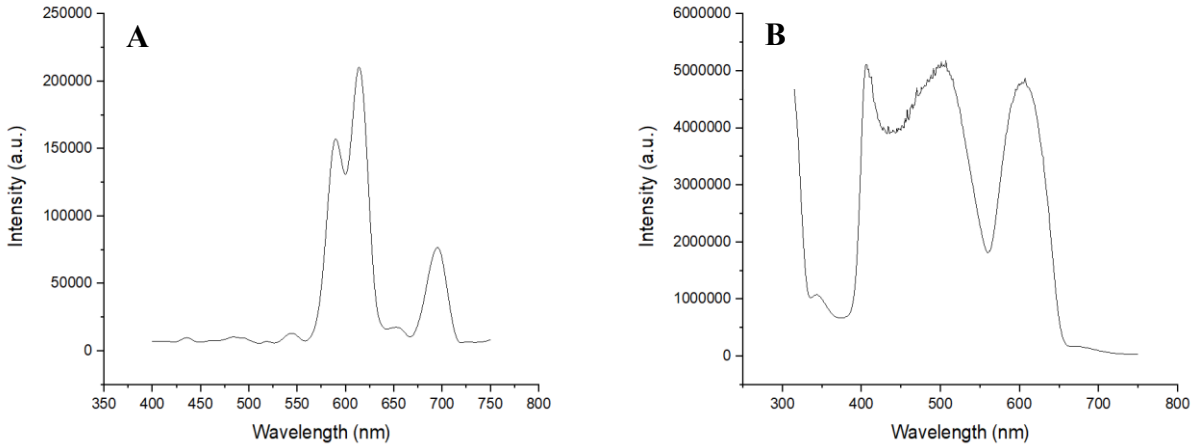



*Figure 18 – Phosphorescence emission graph for **Eu.2** with $\lambda_{ex}$=300 nm (A), Fluorescence emission graph for **Gd.2** with $\lambda_{ex}$ = 304 nm (B); where the peak at 608 nm is an artifact.*

The fluorescence emission spectrum of the gadolinium analogue, **Gd.2** (Figure 18B) is dominated by broad bands suggestive of a conjugated π-system of the ferrocene moiety. It is revealing that these peaks are not observed in the europium analogue. This is strongly suggestive of efficient energy transfer from the chromophore to the metal in the europium containing system- there are no peaks that do not correspond to $^5D_0$-$^7F_J$ transitions, indicating that any ligand-centred excited states must be quenched rapidly before they can emit. The peak at 608 nm seems to be 2λ of excitation wavelength and this is an artifact. The fluorescence emission of **Gd.2** illustrates very weak emission and hence the spectrum is dominated by artifacts.

The absorption of **Ln.2** compared to excitation fluorescence spectra did not display good

overlap which means the sensitisation of ferrocene carboxylate was not efficient. This is also clear from measurement of europium phosphorescence emission which was shown to be weak even with the largest slit length of excitation. This represents that more research on ferrocene should be made and if this displays a weak sensitisation of ferrocene carboxylate, different sensitisers should be employed.

## 2.3.Electrochemical and Spectroelectrochemical Studies of Ferrocene-Ln Complexes

As illustrated in Figure 19, the typical electrochemistry set-up is a three-electrodes system consisting of a working electrode (WE), counter electrode (CE) and a reference electrode (RE) submerged in the same electrolyte solution. The WE is the electrode where the desired redox reaction takes place, providing a surface at which the analyte undergoes reduction and oxidation (redox). Typical working electrodes are conductive, chemically stable and electrochemically inert materials, ranging from inert metals such as gold, platinum, or silver, to carbon materials such as graphite or glassy carbon. The applied potential at the WE is measured against the RE, therefore the RE acts as a reference in measuring and controlling the working electrode potential, without passing any current. The reference electrode should have a constant, stable and well-known electrochemical potential. Examples of commonly used reference electrodes are the saturated calomel electrode (SCE) or the silver/silver chloride (Ag/AgCl) electrode. The CE is used to close the electrochemical circuit, so the role of the counter electrode is to pass the current needed to balance the current observed at the working electrode. Counter electrodes are usually made from good and electrochemically inert conductors, examples including platinum, carbon or gold. Ideally, the CE has a large surface area, much larger than that of the WE to ensure that the redox reaction occurring at CE can occur fast enough so as not to limit the process at the WE. To avoid mass transport limitations, it is usually the case that the WE is a rotating disc electrode

(RDE) so that it rotates during experiments inducing a flux of analyte to the electrode achieving a steady-state mass transport regime, for which the extent of the redox reaction depends on the rotation rate of the electrode.

A potentiostat is an electronic instrument used to control the voltage difference between the WE and the RE. The potentiostat implements this control by injecting current into the electrochemical cell through the CE, and by measuring the current flow between the working and counter electrodes. The controlled variable in a potentiostat is the cell potential and the measured variable is the cell current. The open circuit potential (OCP, which could also be referred to as the equilibrium potential), is the potential measured between the working and reference electrodes when no current flows within the circuit. The OCP should be around the midpoint potential ($E_{1/2}$) of the redox analyte.

In this study, a saturated calomel electrode (SCE) was used as a RE, a platinum wire was used as a CE, and a graphite electrode was used as a WE. NaCl was always used as a supporting electrolyte (≈ 50-100 mM) . All the potentials were measured against the SCE and then converted relative to the Standard Hydrogen Electrode (SHE) by using the conversion *E* (vs SHE) = *E* (vs SCE) +0.2415 V at 25°C. [171] Before undergoing any electrochemical measurement, the SCE reference electrode was calibrated by measuring the midpoint potential of the well-known redox mediator methylviologen ($E_m$= -445 mV vs SHE).

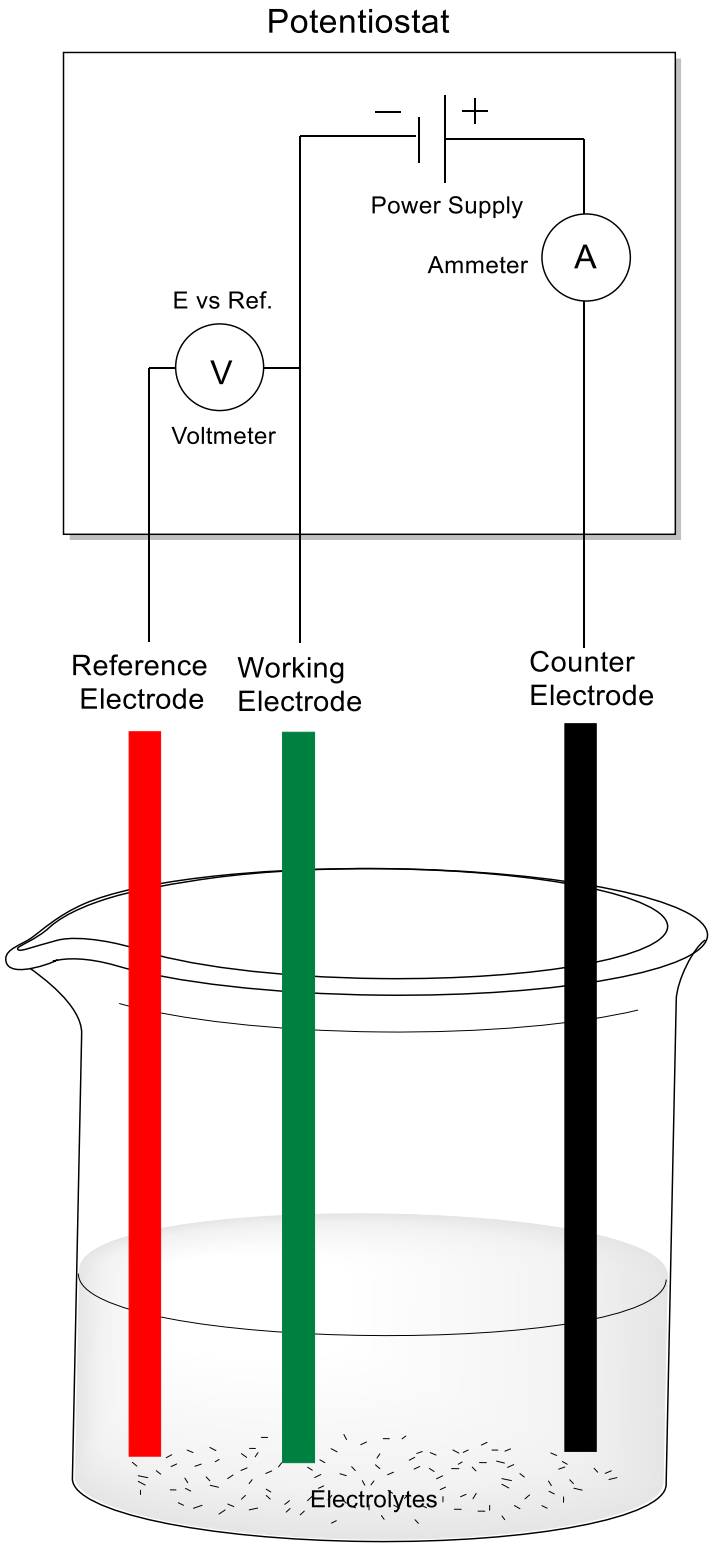



*Figure 19 - Adapted diagram of a typical three-electrode electrochemical cell.* [172, 173]

Figure 20 shows the spectroelectrochemical (SEC) setup used for UV-Vis and luminescence measurements. This consisted of a peristaltic pump, a sealed glass vial containing the analyte

sample, a quartz cuvette and a three-electrodes electrochemical cell. The mechanical pump was used to flow the sample around the SEC set-up at a 50 rpm speed, allowing fast and even distribution of the reduced and oxidised species. As for sample preparation, the sample was dissolved in the appropriate solvent inside a glass vial that was later on sealed with a rubber lid to make it air-tight. The glass vial was flushed with Argon overnight, before setting up the whole SEC setup inside a $N_2$ glovebox (Glove Box Technology Limited, UK $\geq$ 2ppm $O_2$) to avoid $O_2$ traces. The specialised quartz cuvette of 1 nm pathlength was placed in between the electrochemical cell and the glass vial containing the sample. It had a lid containing an inlet and an outlet each screwed to a thin plastic tube to allow sample flow in from sample vial and flow out to the pump and back to the sample vial. The flow electrochemical cell was designed and develop in Prof. Kylie Vincent's group. The three electrodes in the electrochemical cell compromised a platinum wire as a CE, a standard calomel reference electrode as a RE and a carbon WE. The electrodes were connected to a potentiostat which was linked to a computer. To control the potential, an Autolab potentiostat (PGSTAT10) controlled by Nova software was used and UV-Vis spectra were collected using a Cary 60 UV-Vis spectrophotometer.

Once the sample was prepared and flushed with Argon overnight, it was connected to the cuvette with a thin tube, and the cuvette was also connected to the electrochemical cell which at the same time was connected to the peristaltic pump. Finally, the peristaltic pump was connected back to the sample solution via an adapted needle to allow the full cycle of the SEC setup. The whole setup was compact and designed to be air-tight (either by screw ends or rubber seal) as oxygen can get reduced at the electrode surface therefore disturbing the desired redox reaction. The air-tight SEC setup was crucial as it has to be transported in and out of the glovebox to be able to transport it where the fluorimeter is to measure

luminescence, at the same time that the compact design allowed the whole setup to be inserted into Fluorolog without disturbing the light pathways.

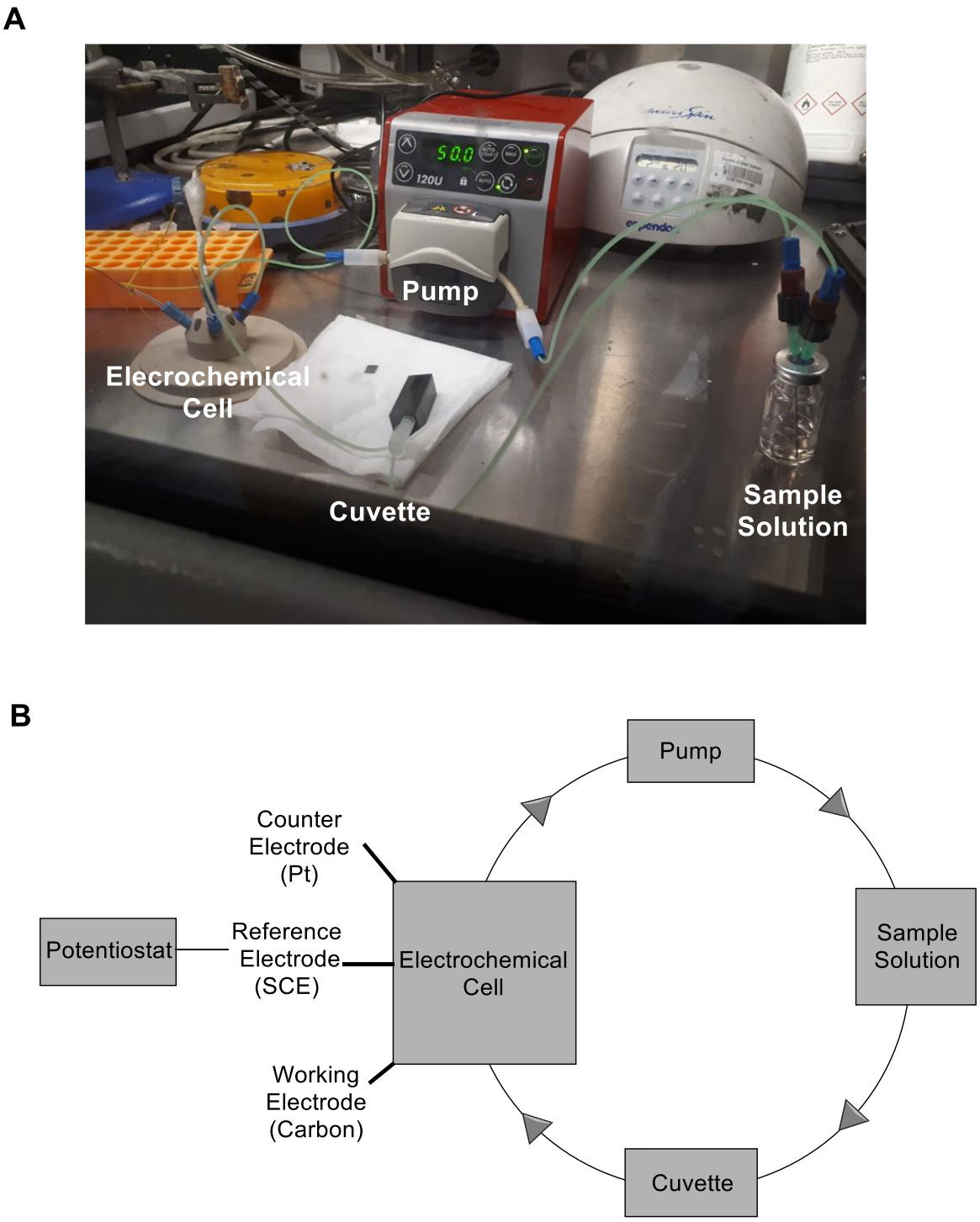



*Figure 20 – Electrochemical setup used for electrochemical measurements where A is picture of actual electrochemical setup, B is a simplified diagram of apparatus setup.*

Normally, a cyclic voltammogram (CV) for solution electrochemistry (i.e. diffusion controlled) processes consists of the typical 'duck' shape. In a CV the potential is scanned linearly vs time in a cyclic fashion while the current is recorded and plotted against the applied potential. Normally a typical voltammogram consists of two peaks and each peak is the result of either oxidation or reduction half-reaction. As illustrated in Figure 21, when the potential is scanned from high to low in the CV, a reduction half-reaction takes place, where electrons flow from the electrode to the sample, causing a cathodic peak (negative current). When the direction is reverse and the potential is scanned from low to high potential, an oxidation half-reaction takes place, where electrons flow from the sample to the electrode, giving rise to an anodic peak (positive current). When the sample is fully oxidised or reduced at the surface of the electrode, the current reaches its maximum peak, $i_{pa}$ and $i_{pc}$ respectively. The potentials of the fully oxidised and reduced peaks are referred as $E_{pa}$ and $E_{pc}$. The reduction potential of the analyte redox sample is specific to the experimental conditions employed and is estimated experimentally by calculating the midpoint potential, $E_{1/2}$, that is the average potential between $E_{pc}$ and $E_{pa}$. A lot of information can be extracted from a simple cyclic voltammogram, such as the stability and reversibility of the redox system, the kinetics of redox reaction a as well as thermodynamic information.[174-176]

The two peaks are separated due to the diffusion of the analyte to and from the electrode. When the redox process is chemically and electrochemically reversible, the separation between cathodic and anodic peaks is 57 mV at 25℃ (for one $e^-$ reduction, or 57 mV/$n$ for more than one $e^-$, where $n$ is the number of electrons involved in the redox reaction), with a width at half max on the forward scan of 59 mV. [177] Reversible systems are able to get fully reduced and can be fully oxidised back. If the peak-to-peak separation $\gg$ 57 mV, then the system can be referred to as irreversible. CV data can be a good indication for kinetic

stability of the compound upon reduction and its ability to return to the original oxidation state. Analytes can be chemically irreversible (product degradation or chemical reaction) or electrochemically irreversible (high energy barrier for electron transfer). In case of electrochemical irreversibility, higher energy barrier for electron transfer can lead to slow electron transfer, requiring more negative or positive potentials to observe the corresponding redox reactions, giving rise to greater separation between the cathodic and anodic peaks. [178]

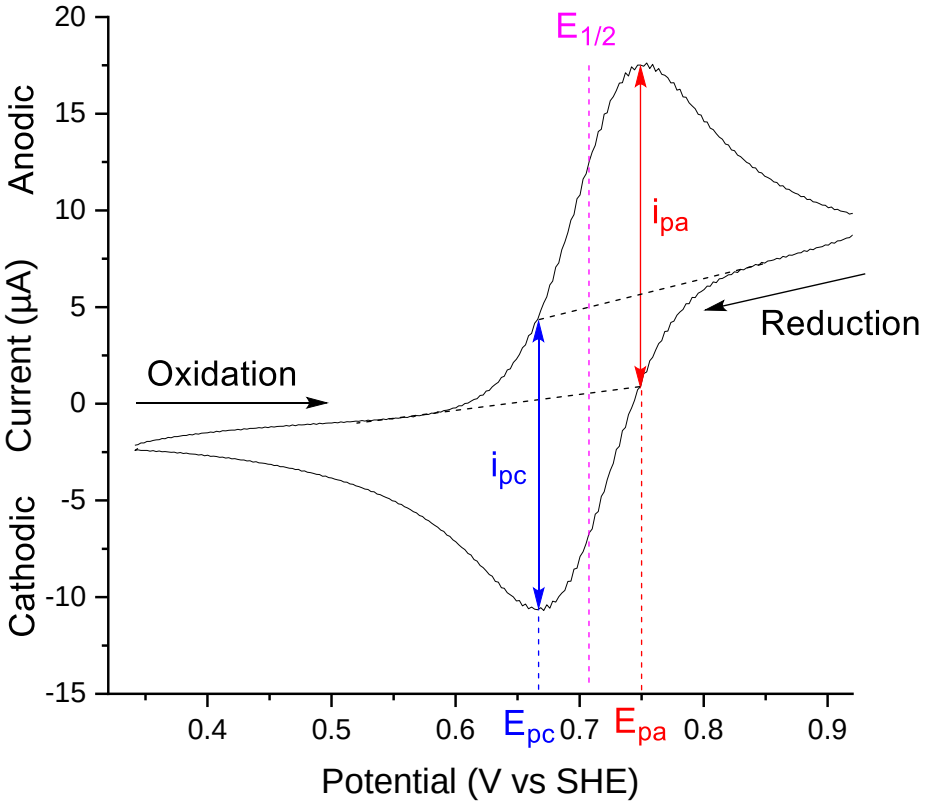



*Figure 21 - Adapted diagram of a typical cyclic voltammogram undergoing reversible one-electron reduction, where $i_{pa}$ = peak anodic current, $i_{pc}$ = peak cathodic current, $E_{pa}$ = potential at peak anodic current, $E_{pc}$ = potential at peak cathodic current and $E_{1/2}$ = reduction potential.* [174, 175, 178]

The cyclic voltammograms (Figure 22) were firstly measured on the ferrocene and DO3A derivatives to identify its reversibility of redox states as well as the potential needed to be

applied in the following UV-Vis and luminescence experiments. Firstly, CV of ferrocene carboxylic acid was scanned at a wide potential range to identify $E_{1/2}$ for ferrocene system (Figure 22A) in order to select the appropriate potential window for the CV measurements on other ferrocene derivatives.

It was clear that the covalent attachment of ferrocene acyl group to DO3A induced irreversibility to the ferrocene system (Figure 22D,E and F) as compared with the ferrocene carboxylic acid (A), acetylferrocene (B). CVs in Figure 22, C and E focus on the potential window for the Eu (III/II) couple with (E) and without (C) ferrocene attachment. It was also clear that the Eu system is reversible regardless of whether or not the ferrocene is covalently attached. Therefore, we can conclude that attachment of ferrocene to Eu-DO3A does not disturb the redox potential of the Eu (III/II) couple and does not introduce irreversibility. On Figure 20E, there are two small oxidation peaks which do not belong to the Eu system and are attributed to small impurities in the solution.

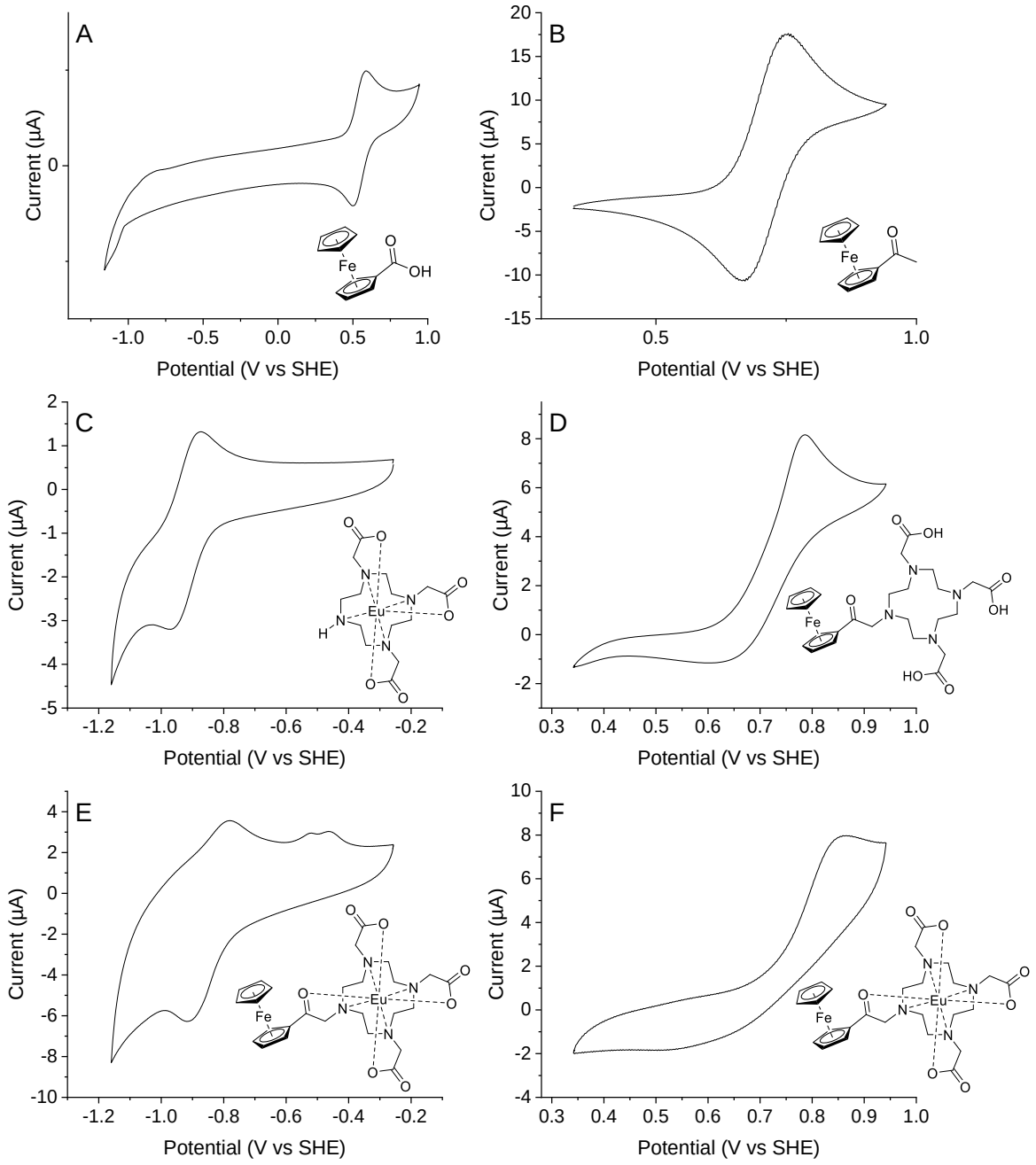



*Figure 22 – CV graph of ferrocene carboxylic acid (A), acetylferrocene (B), Eu-DO3A (C), acetylferrocene-DO3A (D), **Eu.2**, (E and F), all CV measured at 50 mV/s scan rate, at 25°C, for2 mM concentrated samples in 50 mM TRIS buffer with 50 mM NaCl.*

Potential window used for CV measurements were between 0.34 to 0.94 V vs SHE for redox cycles induced at ferrocene (Fe) centre and -1.18 to -0.208 V vs SHE for redox cycles induced at Eu centre. The mid-point potential, $E_{1/2}$ of ferrocene and DO3A derivatives were derived from Figure 22 and summarised in Table 1.

*Table 1 - Mid-point potential, $E_{1/2}$ for ferrocene and DO3A derivatives as shown in Figure 22.*

| | Name of compound | Mid-point potential, $E_{1/2}$ (V vs SHE) |
|---|---|---|
| A | Ferrocene carboxylic acid | 0.550 |
| B | Acetylferrocene | 0.711 |
| C | Eu-DO3A | -0.925 |
| D | Acetylferrocene-DO3A | 0.735 |
| E | Eu.2 | -0.846 (Eu) |
| F | | 0.699 (Ferrocene) |

To see if this irreversibility is also introduced in non-covalently linked system, CVs were taken for the self-assembled system of Eu-DO3A and ferrocene carboxylic acid (Figure 23).

As shown in Figure 23, it was interesting to see that there has not been much distinguishable change to the position of the Eu-DO3A and ferrocene carboxylate peaks on the CV graph upon addition of ferrocene carboxylate to Eu-DO3A. It is clear that Eu(III/II) and Fe(II/III) redox reactions are fully reversible for the self-assembled system, in stark contrast with the irreversibility observed for the acetylferrocene-DO3A and Eu-acetylferrocene-DO3A covalent systems (Figure 22D and E/F).

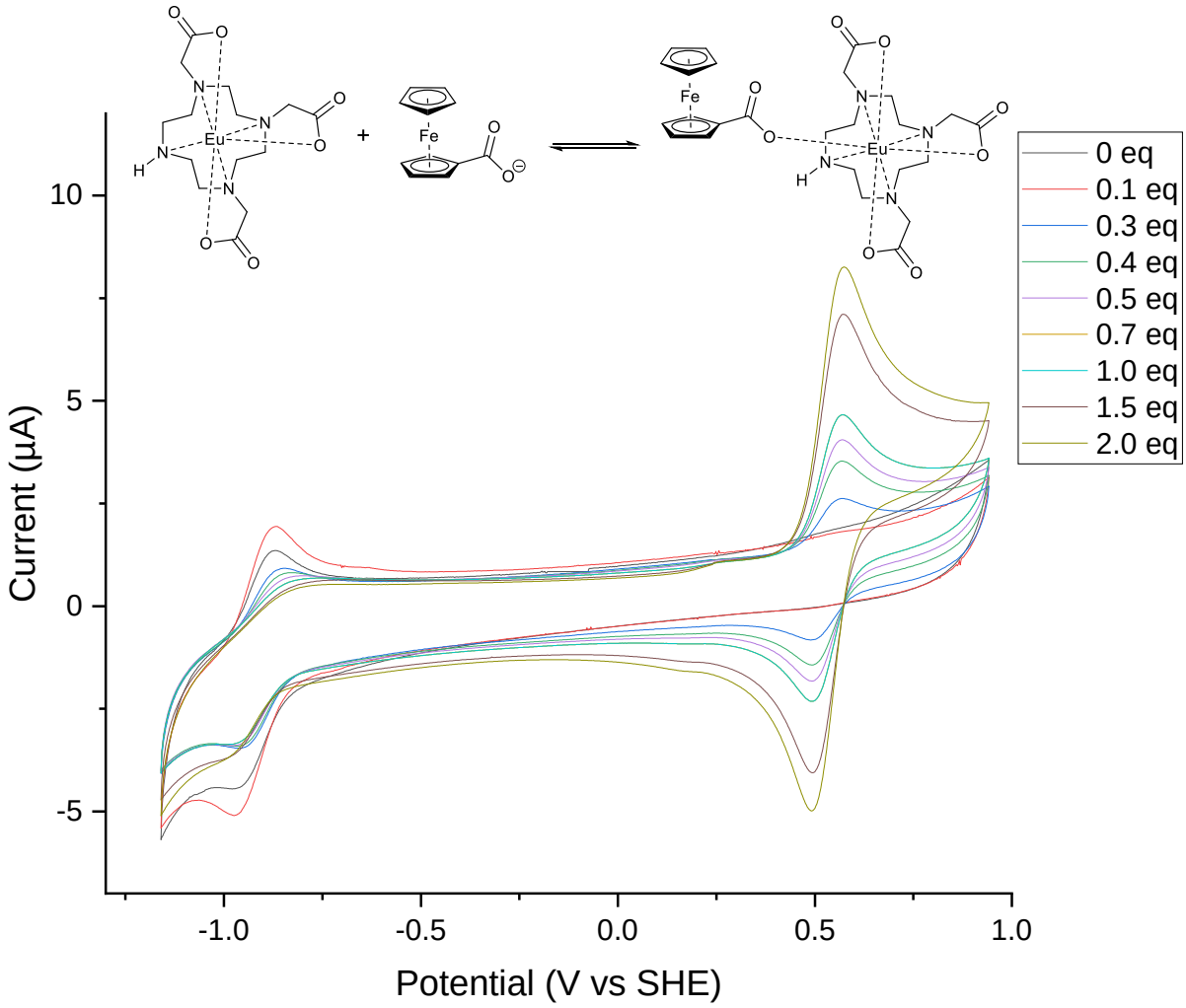



*Figure 23 - CV following titration of Ferrocene carboxylic acid to Eu-DO3A; all CV measured at 50 mV/s scan rate, at 25°C, for2 mM concentrated samples in 50 mM TRIS buffer with 50 mM NaCl, measured in the flow cell (Figure 20).*

UV-Visible measurements (Figure 24) and phosphorescence measurements (Figure 25) were also completed on Eu-acetylferrocene-DO3A (**Eu.2**) while changing the oxidation state of ferrocene (Fe) and europium centre electrochemically. Oxidation of ferrocene centre (from $Fe^{2+}$ to $Fe^{3+}$ state) was induced by applying +1.0 V vs SHE and $Fe^{3+}$ was reduced back to $Fe^{2+}$ state by applying +0.3 V vs SHE.

As illustrated in Figure 24, UV-Vis measurements were taken upon electrochemically

induced redox reaction at both the europium centre and ferrocene centre. These measurements were taken for both the covalently linked system (Eu.2) and the self-assembled system of Eu-ferrocene carboxylate and were compared. When -1.1V vs SHE was applied, this reduced the Eu(III) to Eu(II) and when +0.2 V were applied, Eu(II) was oxidised back to Eu(III). Similarly, when +1.0 V vs SHE was applied, ferrocene (Fe(II)) was oxidised to ferrocenium (Fe(III)) and when +0.3 V vs SHE was applied, ferrocenium (Fe(III)) was reduced back to ferrocene (Fe(II)). These cycles were repeated twice. Each redox cycle was initiated by the UV-Vis measurements at open circuit potential (OCP), referring to any measurements taken without any potential applied before starting the redox cycles. This was to make comparison of all the systems with and without applied potential.

The covalently bonded system (**Eu.2**) and self-assembled system show contrasting UV-Vis spectra. For the self-assembled Eu-Ferrocene carboxylate system, a 1:1 molecular ratio of Eu-DO3A and ferrocene carboxylic acid were combined and UV-Vis measurements were taken.

Upon changing between the Eu(II) and Eu(III) states on self-assembled system (Graph A, Figure 24), there was minimal change in the absorbances and the spectra at OCP were very similar to that of the oxidised Eu centre. As UV-Vis spectroscopy only shows the absorption at the ferrocene moiety, this means that redox cycle at the Eu centre did not affect the energy of absorption at the ferrocene moiety. However, with the redox cycle at the ferrocene centre (Figure 24, C), not only the spectra at OCP were significantly changed upon oxidation but also the spectra of ferrocene compared to ferrocenium state. Upon the oxidation of ferrocene (Fe(II)) to ferrocenium (Fe(III)), a new peak appeared around 635 nm, which relates to the

absorption band for ferrocenium.[179] Following the appearance of the new peak at 635 nm, the sample solution visibly changed the colour from dark yellow to purple.

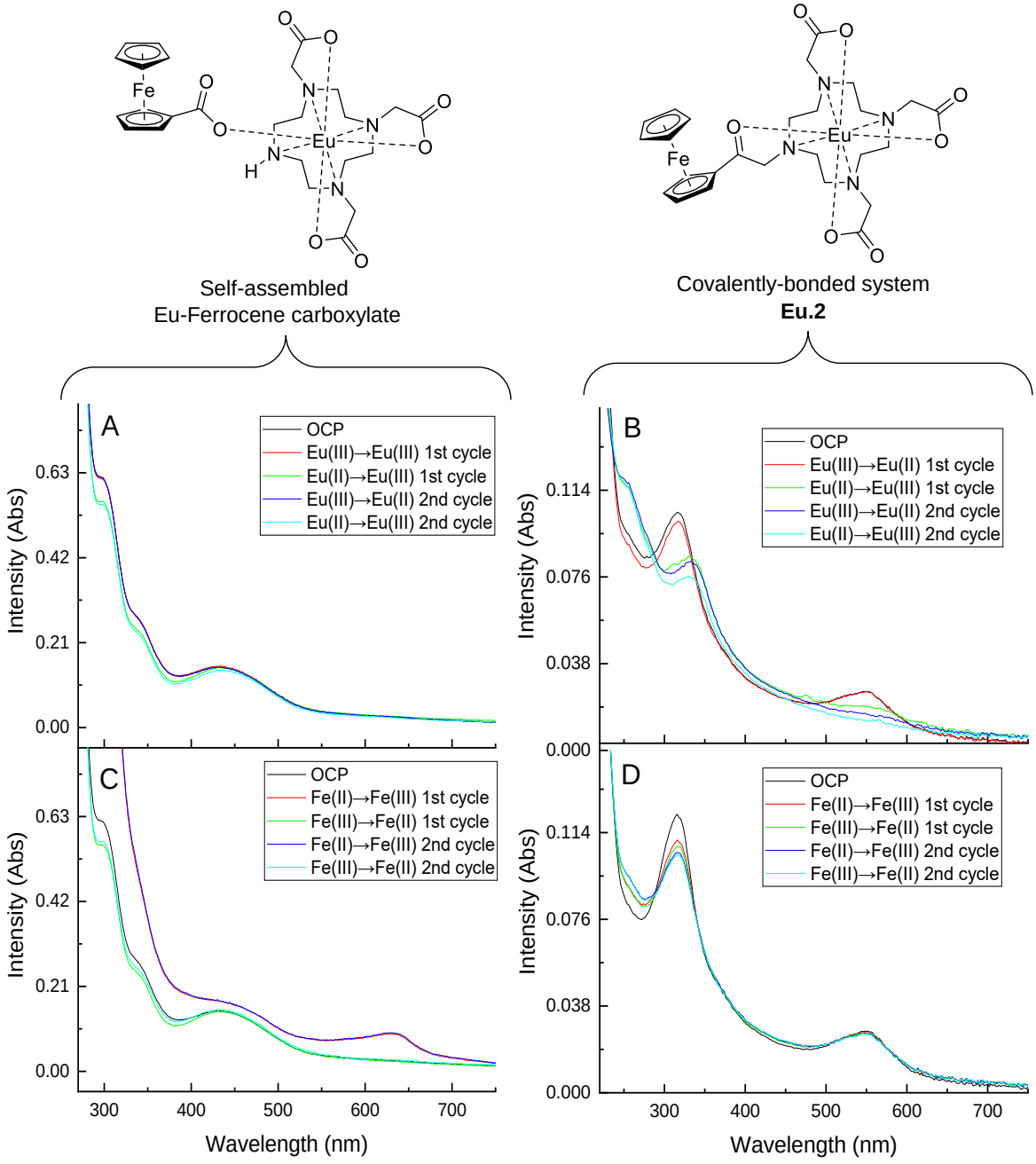



*Figure 24 - UV-Vis spectra of self-assembled Eu-ferrocene carboxylate system (A,C) and* ***Eu.2*** *(B,D), while applying -1.1 V/+0.2 V for redox reaction at Eu (A,B) and +1.0 V/+0.3 V for redox reaction at Fe centre (C,D) at scan rate 50 mV/s, for 1 mM sample in 0.1 M Tris buffer containing 0.15 M NaCl, measured in the flow cell (Figure 20), at 25°C.*

For **Eu.2**, upon the first cycle of redox reaction at Eu centre (Figure 24, B), the peak intensity at 256 nm has increased, and there was a shift in the position of the peak from 317 nm to 332 nm. The peak at 552 nm disappeared over the course of redox reactions and this made the sample solution to change colour from purple to brown. After the first oxidation of Eu(III) to Eu(II) (Figure 24, B, red trace), the absorption intensity could not be reinstated to the original intensity in the following (second) cycle (Figure 24, B, blue trace), which demonstrates that there has been some irreversible change in the complex and this chemical change could not reinstate the absorption bands of either the measurements taken at OCP or the first cycle of Eu oxidation from +2 to +3 oxidation state. The chemical change was also apparent upon applying potential for redox reactions at the ferrocene centre (Figure 24, D). Oxidation of ferrocene showed decrease in absorption intensity at 298 nm.

Unlike **Eu.2**, the self-assembled system showed reversible change of absorption following the redox cycles at both the europium and the ferrocene centre, which matches the reversibility of the redox reactions observed in the CV data (Figure 22). The irreversible **Eu.2** electrochemical system also matched the irreversible Eu and ferrocene (Fe) redox cycles as shown in CV data (Figure 22).

There are several possible reasons behind these differences in reversibility; the first possibility could be that ferrocenium is not stable enough to undergo few redox cycles. The second possibility is that the oxidation is enhanced by some kind of catalytic reaction or that when the ferrocene or Eu centre gets oxidized, irreversible chemical reaction may have taken place and therefore, the system could not come back to its original state. For this reason, mass spectroscopic studies have been performed to find out the intermediates formed during

the redox reaction but there has been no definite sign of decomposition nor the formation of oxidized intermediate.

Spectroelectrochemical phosphorescence emission measurements were taken with covalently linked system, **Eu.2**, as illustrated in Figure 25. Interestingly, when the potential was applied every 15 minutes, the intensity of luminescence gradually increased but never returned to the starting intensity of $Fe^{2+}$ before oxidation. This agrees with the observed irreversibility of the redox reaction. However, this was in contrast to Tropiano's work (with **Eu.1**)[135], which showed electrochemical reversibility (in CVs) and UV-Vis measurements, as well as the ability of the system to act as a "switch" to turn on/off the luminescence, which meant that depending on the redox state of the iron or lanthanide centre, luminescence emission at the lanthanide centre could be quenched and therefore allowed for a controllable luminescence via electrochemistry. These results made us to reconsider the case of Tropiano's previous work [135] and the reasons making these two systems to react so differently.

In order to find the cause of low stability of ferrocene system, **Eu.1** [135] was re-synthesised. However, due to the lack of time and restriction in lab occupancy, the collaboration work with Vincent group, electrochemical behaviour of **Eu.1** could not be tested. Since the restriction is now lifted, it would be worth investigating in **Eu.1** in the future.

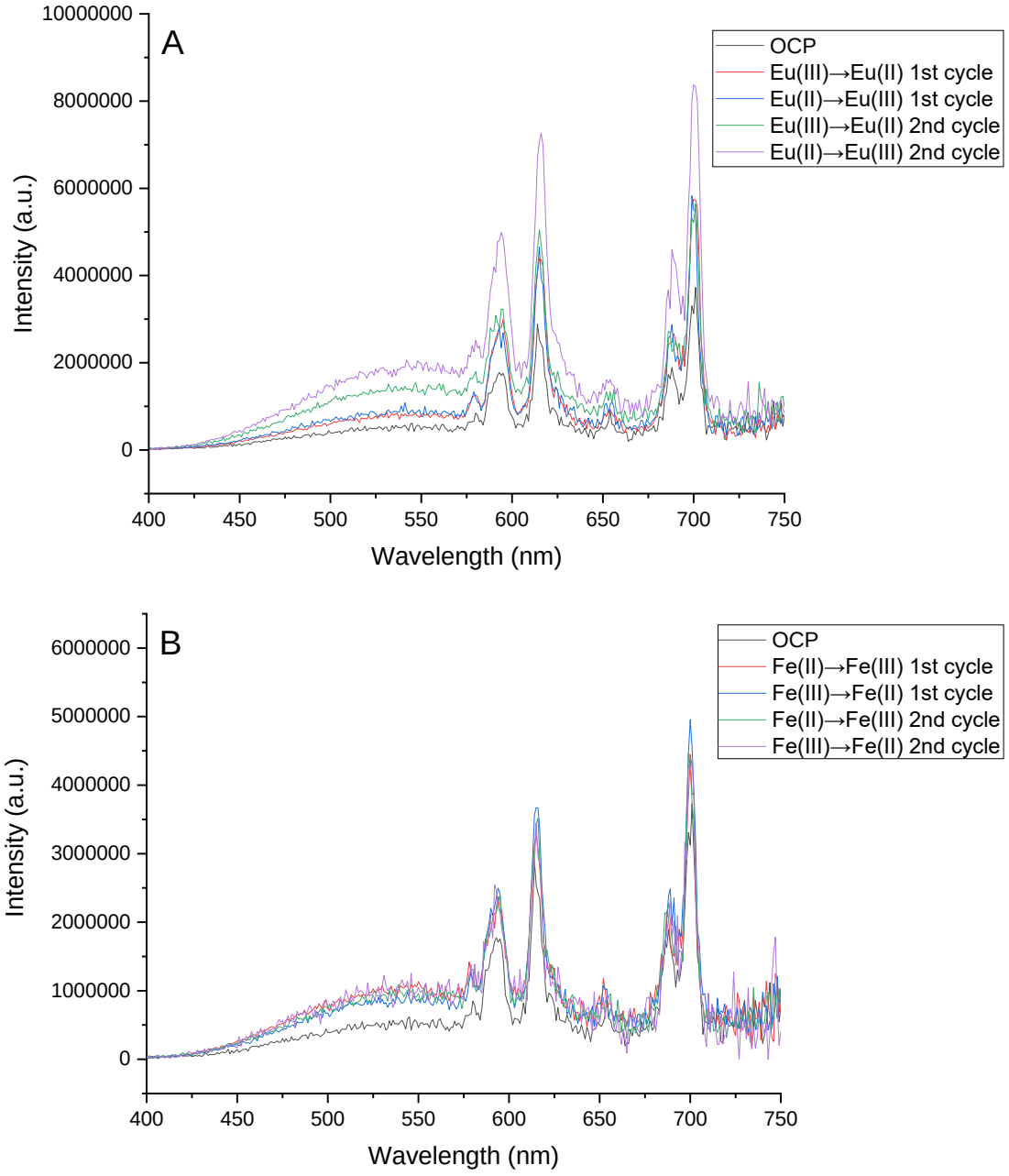



*Figure 25 – Phosphorescence emission spectra of **Eu.2** when excited at 300 nm, while applying -1.1 V/+0.2 V for the redox reaction of Eu (A) and +1.0 V/+0.3 V for redox reaction of Fe centre (B) at scan rate of 50 mV/s; all with 0.1 mM sample in 0.1 M Tris buffer containing 0.15 M NaCl, using slit width 10 nm/5 nm for excitation and emission, respectively in the flow cell (Figure 20), at 25°C.*

As there was negligible to no change in the CV of Eu-DO3A upon titration of ferrocene carboxylic acid (ferrocene carboxylate), and the luminescence emission data obtained is rather the puzzling, it was unclear whether the ferrocene carboxylate was actively binding

to Eu-DO3A. Therefore, we moved on to study the change in lifetime (decay time) of Eu-DO3A upon titration of ferrocene carboxylate. Previously, Dickins et al., [180] studied the change in structural, luminescence and NMR spectra upon acetate binding of chiral diaqua ytterbium, gadolinium and europium complexes, where they could see the hydrogen bonding of axial acetate oxygen from the decrease in the number of bound water molecule, q, which was derived from the lifetime. The reduction in q was because of the decrease in lifetime resulted from the replacement of bound water molecule by acetate binding.

Here, the lifetime, τ of Eu-DO3A was measured upon the titration of ferrocene carboxylate at pH 5.0 and 8.0 (slightly acidic and basic conditions) as shown on the Table 2.

*Table 2 - Table of lifetime taken upon titration of ferrocene carboxylate to Eu-DO3A solution in deionised water, at pH 5.0 and 8.0, measured at 25℃. Calculated hydration numbers were obtained using Kimura's equation, [181] and should be discounted as unreliable.*

| Equivalents of ferrocene carboxylate | pH 5.0 | | pH 8.0 | |
|---|---|---|---|---|
| | Lifetime, τ (ms) | Calculated hydration number, $q_{cal}$ | Lifetime, τ (ms) | Calculated hydration number, $q_{cal}$ |
| 0 | 0.40 | 2.06 | 0.40 | 2.06 |
| 1 | 0.11 | 9.11 | 0.15 | 6.51 |
| 2 | 0.10 | 10.08 | 0.11 | 9.11 |
| 3 | 0.09 | 11.27 | 0.07 | 14.67 |
| 4 | 0.08 | 12.76 | (unmeasurable) | - |

As shown on the Table 2, There was decrease in lifetime for both pH 5.0 and 8.0 with increasing concentration of ferrocene carboxylate. It was apparent that there was a dramatic quenching effect by the ferrocene carboxylate and this proved that there is an association (or

exchange) of ferrocene carboxylate to Eu-DO3A. Thus, it was evident that ferrocene carboxylate is capable of binding to Eu-DO3A but the question remained as to why the ferrocene carboxylate binding did not affect the electronic communication of lanthanide centre.

Moreover, the hydration numbers, $q_{cal}$ shown in Table 2 were calculated using an equation derived by Kimura et al.[181], which were calculated by correlating the various luminescence decay measurements:

$$n_{H_2O} = 1.07 \times k_{obs}(Eu) - 0.62 \qquad (2.1)$$

Where

$$k_{obs} = \frac{1}{\tau} \qquad (2.2)$$

The calculated hydration number seems plausible in the absence of ferrocene carboxylate, given that the ligand is heptadentate, but the subsequent calculated values do not withstand scrutiny. Even if we were to assume sequestration of europium ions from DO3A, the europium aquo ion contains only nine water molecules: furthermore, coordination of ferrocene is required to sensitise luminescence from the lanthanide. It is clear that the equation is not suitable for use with this system. Unlike the more widely used equation (Equation 1.10), [152] Kimura's equation (Equation 2.1) [181] does not rely on recording a second-rate constant in deuterated media, meaning that it cannot account for other quenching pathways beside OH oscillator mediated quenching. In this system (and indeed in most systems), the addition of a secondary quenching pathway through charge transfer between ligand and metal will clearly inhibit luminescence and shorten the lifetime. As a result, the tabulated values of q above should be discounted. The challenge in matching pH between solutions in protic and deuterated solvents made it impossible to recod a comparable lifetime in $D_2O$.

In this chapter, three main systems were discussed, Tropiano's model (**Eu.1**), covalently linked Eu-ferrocene system (**Eu.2**) and self-assembled system as shown in Figure 26. For a self-assembled Eu-ferrocene system, there was clear evidence of 1:1 binding of carboxylate followed by a second carboxylate binding from phosphorescence emission taken upon titration of ferrocene carboxylate to Eu-DO3A (Chapter 2.1). However, there were little to no change in the UV-Vis measurement. Subsequently, lifetime measurements upon titration of ferrocene carboxylic acid to Eu-DO3A showed decrease in lifetime with increasing concentration of ferrocene carboxylate, which in turn represent that ferrocene carboxylate is capable of binding to Eu-DO3A.

Following UV-Vis and luminescence measurements on the covalently bonded Eu-ferrocene system (**Eu.2**, Figure 26), we could observe that **Eu.2** was electrochemically irreversible. It was noted that the absorption intensity did not quite return to that of ferrocene when the ferrocene was oxidised to ferrocenium, and in contrast, kept on increasing. This could mean that there is an irreversible chemical process occurring upon reduction of **Eu.2**, which could likely hinder the complex to fully recover its original oxidation state. This is in disagreement to the electrochemically reversible system of **Eu.1**, [135] which has shown effective quenching and this resulted in inhibition of effective electronic communication between ferrocene and lanthanide centre to sensitise lanthanide luminescence.

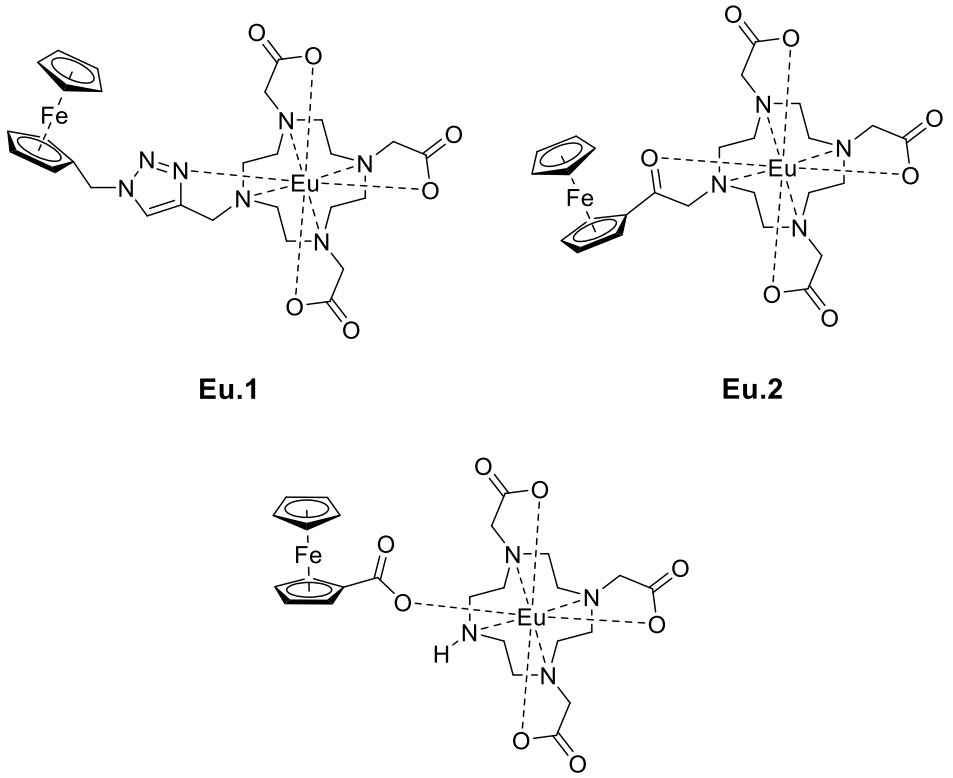



*Figure 26 – The main Eu-Ferrocene systems discussed in this thesis.*

One of the main differences between **Eu.2** and **Eu.1** is the presence of triazole linker between ferrocene centre and lanthanide DO3A moiety. This could imply that the triazole linkage between Eu-ferrocene in **Eu.1** may have a major influence in the reversibility of the ferrocene centre and therefore, acting as an effective switch for luminescence in accordance with the redox reactions at the Fe centre. More importantly, **Eu.1** has a $CH_2$ linkage between the ferrocene and the triazole which prevents the Dexter energy transfer mechanism between ferrocene and europium. This differs to the Tropiano's work [135] that allows the Dexter mechanism.

Overall, three main Fe-Eu systems were investigated to examine the dependence of direct attachment of europium with ferrocene and the difference between ionic and covalent

bonding between the ferrocene and the europium centre. It was apparent that the linker size, the type of bonding, and the distance between the europium and ferrocene have shown to influence the ferrocene sensitising/quenching ability of lanthanide luminescence. A systematic study of a range of complexes is clearly needed to interpret the available pathways in full.

.

# Chapter 3. *d-f* Compatible Phenanthroline Complexes

Recent studies on solution-state spectroscopy for luminescence spectroscopy have been developed Ln(III) emission in the near-IR.[182-184] In comparison to Eu(III) or Tb(III), near-IR systems have a lower emissive energy level to absorb visible light with assistance of the chromophores. This can broaden the range of detection in bioassays.[185] Therefore there has been increased research on Ln emitting near-IR by using *d*-block complexes as sensitizers. The emissive sensitizer weakens its emission because of the electronic energy transfer and intensifies the Ln-based signal. This interaction can further develop into probes, sensors, and assays and examples including Ru(II),[167] Cr(III),[186] Pt(II)[168, 169] and ferrocenyl group were investigated previously.[167]

As previously described in Chapter 1.4, $[Ru(bpy)_3]^{2+}$ in particular gained our attention due to its useful spectroscopic and photophysical behaviours:

Firstly, its exceptionally high triplet state yield allows excitation of Nd(III) and Yb(III) with visible light of up to 500 nm.

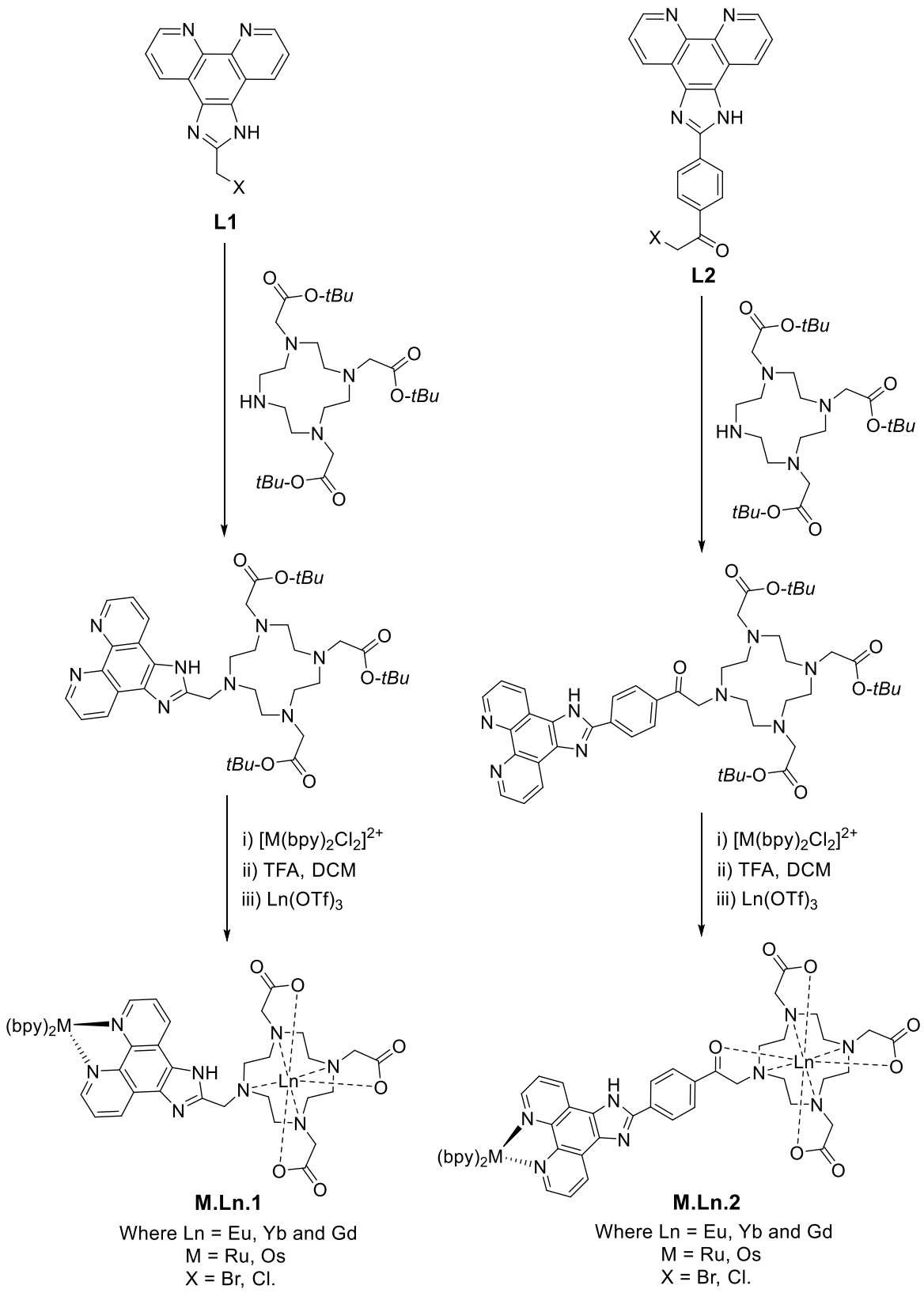
Secondly, its interesting electrochemical characteristics. [187]

Thirdly, due to its conjugated organic moiety, $[Ru(bpy)_3]^{2+}$ is one of the sensitisers that enables visible light in place of near-UV excitation. [54, 109]

Lastly, $[Ru(bpy)_3]^{2+}$ can solve the problem of the forbidden direct energy transfer of *f-f* transition and its low absorption coefficients (as a consequence) and provide indirect excitation by energy transfer from the triplet state of organic chromophores. [167]

The imidazole ring on heteroaromatic phenanthroline can be explored to be used for a pH probe. The imidazole N-H proton can interact directly with the Ln centre, thus, a short distance between the imidazole N-H proton and Ln.DO3A is desirable.

The initial plan for the synthesis of **M.Ln.1** and **M.Ln.2** are shown in Scheme 6. The difference between these complexes was that the attachment of the aromatic phenanthroline chromophore to Ln.DO3A were either direct or indirect. The initial plan shows that ligand 1 (**L1**) or 2 (**L2**) firstly is coordinated to DO3A and then to $[M(bpy)_2Cl_2]^{2+}$ where M = Ru or Os. Deprotection of the carboxylate arms of DO3A macrocycle and complexation with lanthanide ion is followed to form **M.Ln.1**.



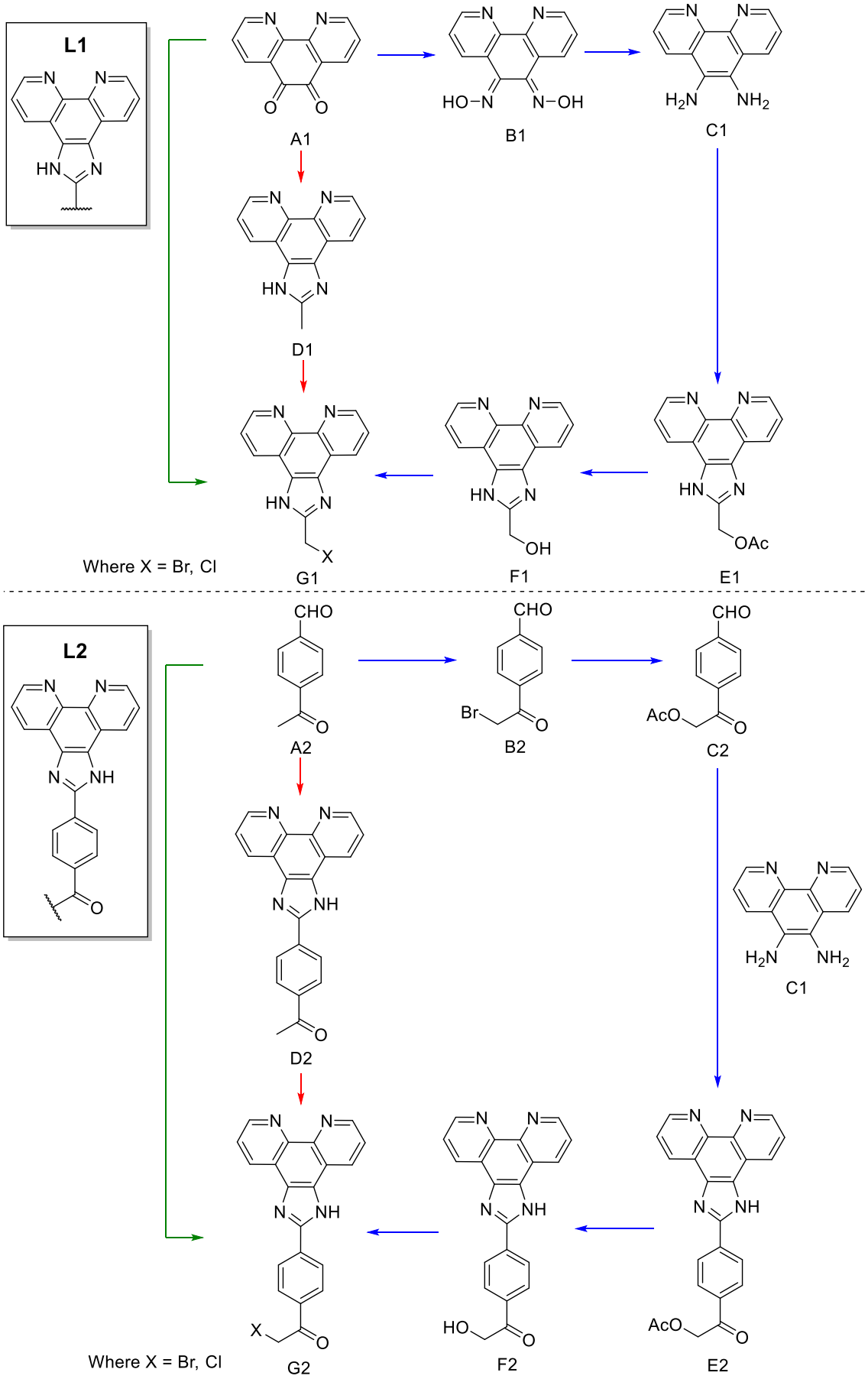

*Scheme 6 - Initial plan for synthesis of **M.Ln.1** and **M.Ln.2**.*

In order to produce **M.Ln.1** and **M.Ln.2**, **L1** and **L2** were initially identified as targets to synthesise. The synthesis of **L1** and **L2** was attempted using different reaction conditions and reagents and the relevant intermediates of **L1** and **L2** are shown in Scheme 7.

Formation of **G1** was attempted in three main pathways: via **D1** (Scheme 7, red trace), direct formation of **G1** from **A1** (Scheme 7, green trace), or via **C1** (Scheme 7, blue trace).

Firstly, synthesis of intermediate **G1** was attempted by the reaction of **A1** with acetaldehyde (via **D1**, red trace), using ammonium acetate in acetic acid (by modifying a procedure from literature). [188, 189] The conversion of **A1** to **D1** occurred successfully, which could be observed in MS and NMR spectra. However, subsequent halogenation to **G1** or hydroxylation for attachment of DO3A were unsuccessful.

Secondly, synthesis of intermediate **G1** was attempted by the reaction of **A1** with chloroacetaldehyde, or chloroacetyl chloride (green trace) using ammonium acetate in acetic acid. [188, 189] However, there was no sign of formation of **G1** either through MS or NMR spectra analysis; $^{1}$H-NMR did not show any corresponding peak for Cl-$CH_2$ group that would have otherwise formed during the formation of a five-membered ring.




*Scheme 7 – A reaction scheme for the attempted synthesis of L1 and L2.*

As the formation of **G1** directly from **A1** or via **D1** by reaction of **A1** with aldehyde or acetyl chloride proved to be difficult, we decided to modify our synthetic plan to form intermediate **C1**, followed by formation of the five-membered ring and conversion to **G1** by several functional group conversions. Therefore, formation of **C1** was attempted next (to follow blue trace).

The synthesis of **C1** involved the reaction of **A1** with $NH_2OH.HCl$, $BaCO_3$ in dry ethanol under reflux for 14 hours, followed by the reaction of **B1** with Pd/C, hydrazine monohydrate in ethanol under reflux in an inert atmosphere. This was successfully made following a procedure reported by Jothi and Alexander. [190] Subsequently, **C1** was reacted with acetoxyacetyl chloride to form a mixture of **E1** and **F1**. The possible reason behind the formation of **F1** could be the wet condition of the solvent used. To test this hypothesis, 3 equivalents of deionised water were added as a trial, but was shown to interrupt a transition from phenanthroline N-acyl chloride to F1. This could mean that excessive amount of deionised water quenches the reaction but minimal amount of water in solvent could have helped with the formation of **F1**. **E1** and **F1** produced from this step were purified by flash chromatography. The purified **E1** was converted to **F1** using 2M NaOH and this was later combined with purified **F1** from the previous step to continue exploring options of chlorination to create **G1**.

However, solubility issues with **F1** limited the option for halogenation; **F1** was only soluble in pyridine, DMF, DMSO and the mixture of DCM and methanol, but protonated solvent could not be used for halogenation as the use of base was required. Several test halogenation reactions were carried out in pyridine and DMF.

Firstly, halogenation of **F1** to **G1** was tried using excess thionyl chloride solution (as a solvent and a reagent) with boron trifluoride etherate, but only partial conversion was observed under $^{1}$H-NMR, TLC and EI-MS spectra. Under $^{1}$H-NMR, the $CH_2$ peak (4.86 ppm, d, DMSO-$d^6$) located next to OH group (5.88 ppm, t, DMSO-$d^6$) had disappeared and a new singlet had appeared at 5.14 ppm ($CH_2$-Cl, s, DMSO-$d^6$). $CH_2$ next to acetyl group (2.15ppm, O=C-$CH_3$, s, DMSO-$d^6$) is found at 5.40 ppm (check supplementary data for more detail).

Secondly, 5 equivalents of thionyl chloride in $CCl_4$ were used but due to the bad solubility, the reaction was unsuccessful.

Thirdly, to improve the conversion, pyridine was used as solvent but was found to react with thionyl chloride and the phenanthroline moiety. Addition of DMF as a catalyst did not help in this reaction.

Fourthly, halogenation with HBr in acetic acid was tried but again, only partial conversion occurred.

Lastly, DMF was used as a solvent with 5 equivalents of thionyl chloride. Some products precipitated as a beige solid which was collected through centrifugation. Products dissolved in the DMF layer were further collected through precipitation with excess THF. The yield of **G1** was very low (<8%) to continue the attachment of DO3A (as shown in Scheme 6) and the complete removal of DMF was incredibly difficult, which meant that the separation of **G1** was also very difficult. Partial conversion of **F1** to **G1** could be observed by MS and NMR spectroscopy. Increasing the thionyl chloride concentration (up to 20 equivalents) showed little to no improvement.

Throughout the attempt to create **L1**, the most significant problem encountered was from its poor solubility, in both organic and aqueous solvents. In attempt to search for an alternative reaction conditions or pathway, we discovered previous work by Wang and Qin explaining how making a five-membered ring without an aromatic linker or without a 700W microwave was unsuccessful, [191] which further supports the difficulty in the formation of **L1**. Hence, the synthesis of lanthanide-phenanthroline system with benzoyl linker (**L2**) was considered for synthesis.

Approaches to the synthesis of **M.Ln.2** were also examined. Likewise, three synthetic pathways were attempted; via **D2** (Scheme 7, red trace), direct formation of **G2** from **A2** (Scheme 7, green trace), or via **C2** (Scheme 7, blue trace).

Synthesis of **G2** was attempted by reaction of **A2** with **C1** to form **D2**, followed by its conversion to **G2** (red trace). Unfortunately, the synthesis of **M.Ln.2** was not feasible as the benzoyl linker made the solubility issue of the phenanthroline derivatives to worse. Although the system with benzoyl linker was successfully formed (**D2**) under MS and $^{1}$H-NMR, this intermediate could not be halogenated (to **G2**) to be able to attach to DO3A moiety. This solubility issue had pros and cons; due to the bad solubility of **C1**, only heterogeneous reaction was allowed and inevitably, some harsher conditions (heating at 100 ℃ or higher, use of DMF or DMSO etc.,) were used. In the case of conversion of **A2** to **D2**, heterogenous reaction eased the collection. Both **A2** and **D2** were insoluble in ethanol but as the reaction progressed over time, the solution became partially soluble wherein the impurities or by-products became soluble in ethanol but the product had precipitated out.

A possible explanation for the unsuccessful conversion of **D2** to **G2** is that the N-H from imidazole could have reacted with another intermediate to form a dimer. Subsequently, protecting this N-H was attempted: benzyl carbamate, tert-butyl carbamate and acetyl group were tried but were unsuccessful. Bromination with copper bromide was not feasible as copper ions can bind to the phenanthroline aromatic nitrogen cavity. Concern arose in the use of other halogenation reagents such as $Br_2$ or HBr which could result in dimerization and multi-bromination. In addition, the small mass of $Br_2$ and HBr compared to the relatively large molecular mass of phenanthroline systems meant dilution of reaction mixture was inevitable which will lower the chance of the efficient reaction. Therefore, reaction with *N*-bromosuccinimide (NBS) was attempted, but was also unsuccessful.

Secondly, formation of **G2** from **A2** via **C2** (Scheme 7, blue trace) was attempted. Although conversion of **A2** to **B2** and **B2** to **C2** were successful, the conversion from **C2** to **E2** were unsuccessful, possibly due to bad solubility.

Within 2 weeks, **E1**, **F1** and **G1** were found to decompose and it was later discovered that the **E1**, **F1** and **G1** were unstable when stored in solution and are possibly light-sensitive. Therefore, the reactions were repeated to synthesise **G1**. Overall, phenanthroline-derived compounds (both **L1** and **L2** derived) were difficult to separate and purify due to bad tailing in flash chromatography.

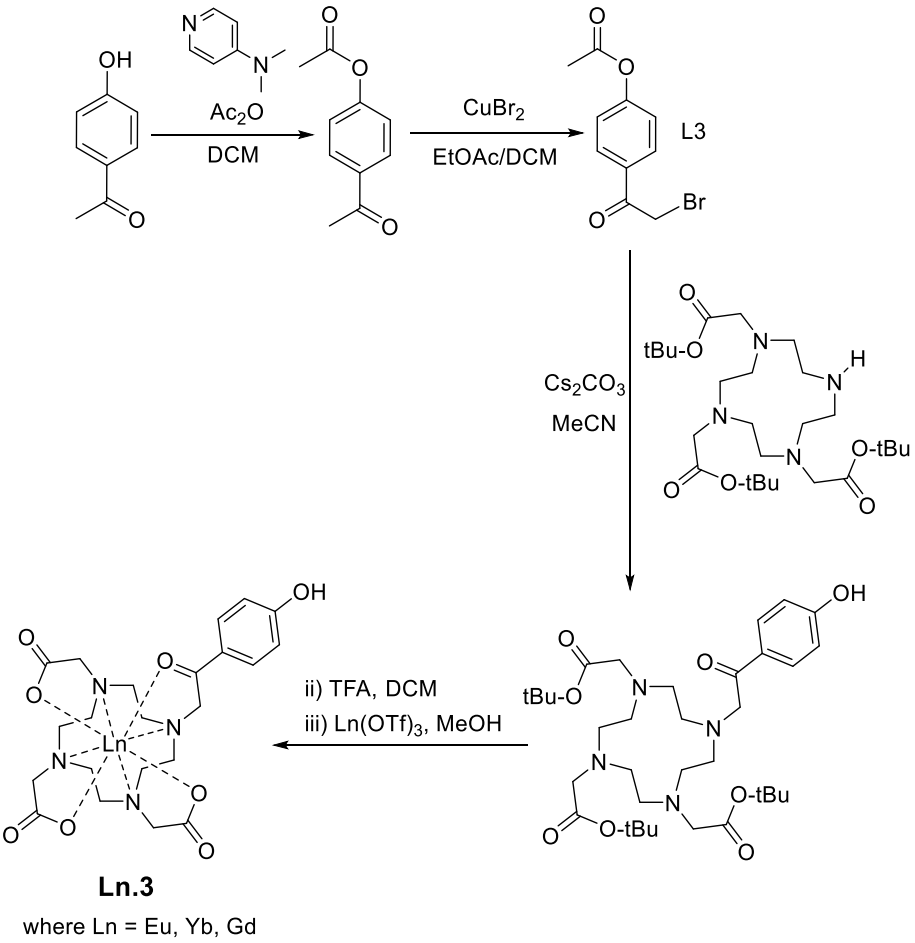
Therefore, the synthetic approach was not taken further to incorporate DO3A and the experiment paused here due to lack of time. As the synthetic step was very close to the formation of **L1** or **L2**, it would be worth completing the formation of **L1** and/or **L2**, and

investigating its photophysical properties and electrochemical behaviour when incorporated to ruthenium or osmium.

# Chapter 4. Hydroxyphenacyl-DO3A as a Bridging Ligand and its Potential for Bioassays

## 4.1. Synthesis and Spectroscopic Analysis of Hydroxyphenacyl-DO3A

Hydroxyphenacyl-DO3A (**Ln.3**) was designed as a bridging ligand (Scheme 8) to combine zirconocene and Ln-DO3A (Scheme 9) but has a potential to be used for other metallocene systems. These ligands can offer pH dependence to become a pH probe or as a sensitizer for a luminescence switch.

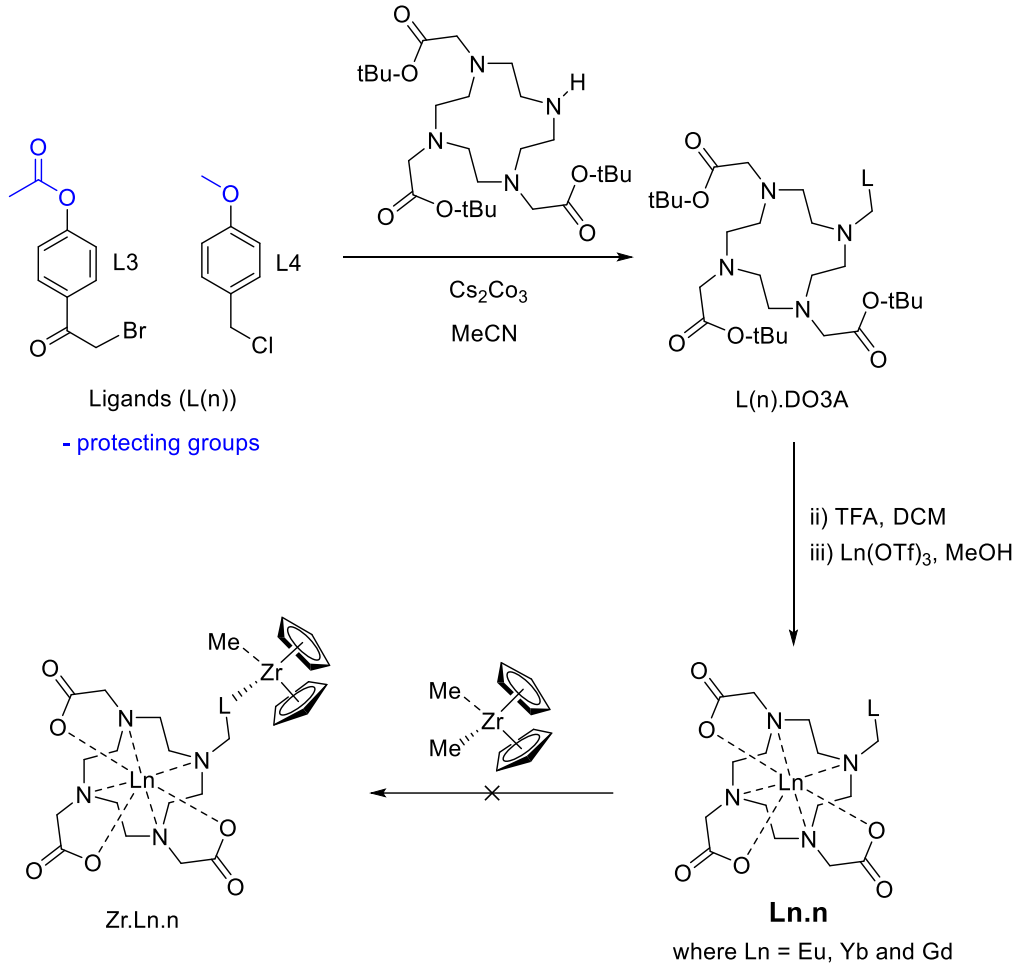



*Scheme 8 – Synthetic route of intermediate bridging ligand, **Ln.3** (where Ln = Eu, Yb, Gd).*

Initially, two versions of ligands, L3 and L4 were proposed to synthesise **L3.DO3A** and

**L4.DO3A** (Scheme 9). **L3.DO3A** was difficult to separate from unreacted DO3A and other by-products for Ln.DO3A synthesis by column chromatography. Several attempts of column chromatography were carried out and it was discovered that **L3.DO3A** degrades with alumina and silica column chromatography gave bad separation. Hence, L3.DO3A was deprotected and purified by HPLC before complexation; the conditions used are explained in detail in Chapter 6.1.7 (data shown in Supplementary data). The purified ligand was carried forward and complexes with europium, ytterbium, gadolinium for analysis in its pH sensitivity.

Synthesis of **Ln.4** gave rise to many difficulties; particularly in finding a suitable protecting groups for L4. Initially, the protecting group (shown in blue) was acetyl group. However, this gave bad solubility in most of organic and aqueous solutions including DMSO. Thus, the protecting group has been modified to methyl group, which eliminated solubility problems, though demethylation was difficult to follow. Therefore, only **Ln.3** was used for further analysis.




*Scheme 9 – Synthetic plan for an attempted synthesis of **Ln.n** and **Zr.Ln.n** complexes.*

To synthesise **Eu.3** and **Yb.3**, **L3.DO3A** was purified to by HPLC before complexation; the conditions used are explained in detail in Chapter 6.1.7 (data shown in Supplementary data). As shown in Figure 27, **Eu.3** has shown predominance of TSAP isomers, but **Yb.3** has shown evidence of exchange broadening leading to re-equilibration and mixtures of TSAP and SAP isomers (Figure 28). **Gd.3** was identifiable from MS data (m/z 636 for $[M+H]^+$). **Eu.3**, **Yb.3**, and **Gd.3** were further analysed for their pH sensitivity.

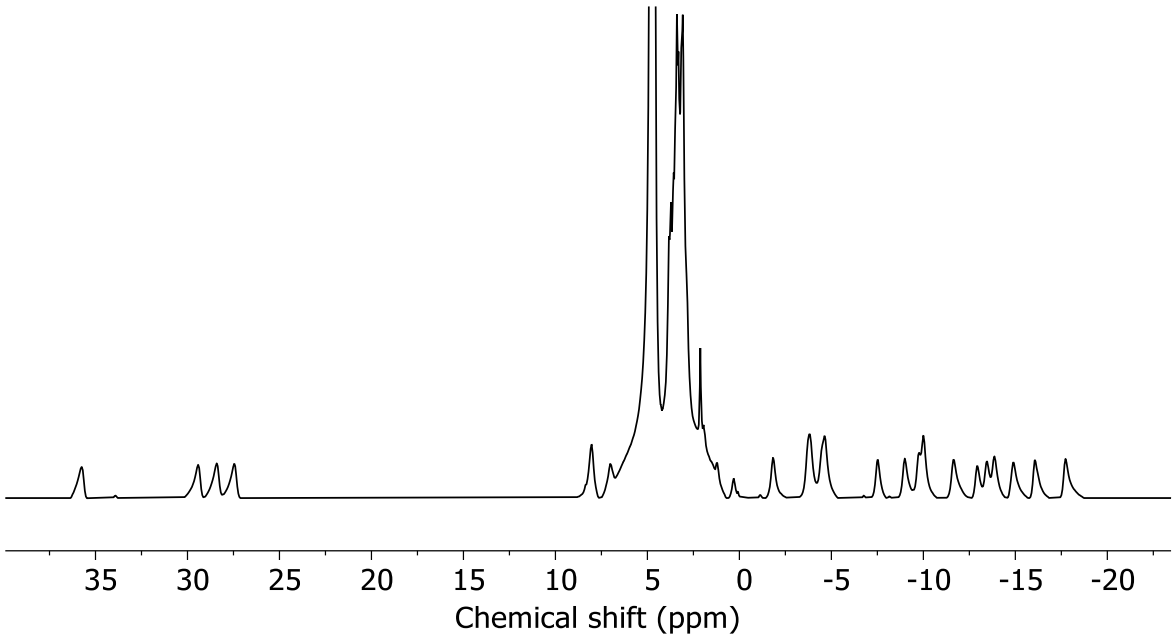



*Figure 27 – $^{1}$H-NMR (400 MHz, $D_2O$) spectrum of **Eu.3** complex, measured at 25°C.*

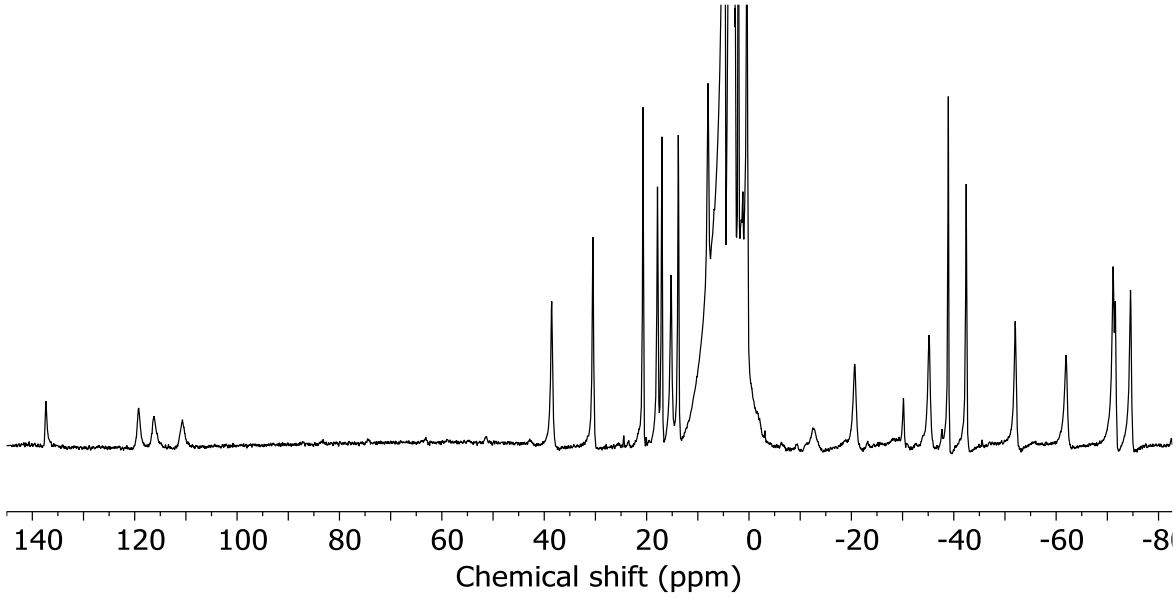



*Figure 28 - $^{1}$H-NMR (400 MHz, $D_2O$) spectrum of **Yb.3** complex, measured at 25°C.*

## 4.2.pH-Study of Hydroxyphenacyl-DO3A

The behaviour of **Eu.3** at different pH conditions has been investigated through UV-Vis, luminescence and $T_1$ relaxivity studies. Firstly, UV-Vis (Figure 29) and relaxivity studies (

Figure 30 and Figure 31) were carried out on the europium complexes between pH 5.5 and pH 9.0. Three different buffers were used: MES for pH 5.5, 6.0, 6.5, HEPES for pH 7.0, 7.5, 8.0 and CHES for pH 8.1, 8.6, 9.0 in Milli-Q water. Buffers were kept at 1 mM concentration for UV-Vis measurement and sample concentration was kept at 50 µM. As you can observe from Figure 29, the protonated complex exhibits a distinctive peak at 304 nm at pH below 6.5, whereas the deprotonated complex has a distinctive peak at 356 nm with isosbestic point at 323 nm. From the ratio of these peaks (Figure 30), a plot of the variation with pH reveals that the pKa of the complex is approximately 7.5.

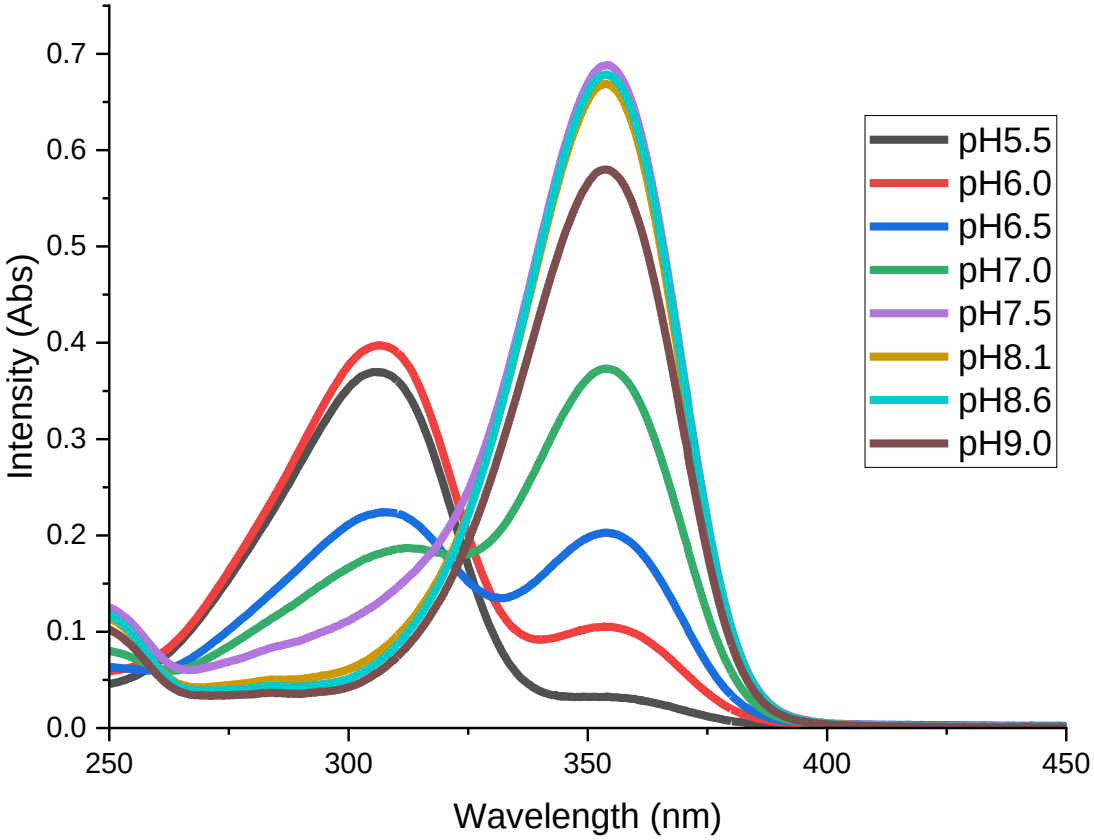



*Figure 29 - UV-Vis spectra of **Eu.3** at pH 5.5 to pH 9.0, measured at 25°C.*

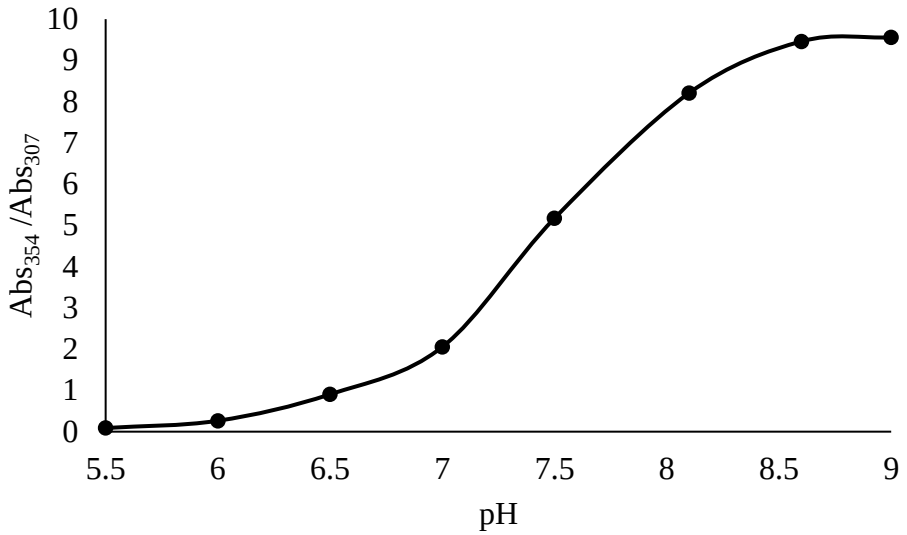



*Figure 30 - Plot of ratio of absorbances of **Eu.3** at 354 nm/307 nm versus pH, at 25°C.*

When considering the development of responsive probes for biomedical applications, tissue pH tends to vary between 7.4 for normal tissue to around 6.8 in certain tumours. The change in absorption spectra of the complex across this pH range made us keen to explore its potential to signal changes in pH.

From Figure 31, it is clear that at all pHs investigated, the water $T_1$ relaxation time decreases and plateaus as the concentration of sample increases. A plot of $1/T_1$ against concentration of the complex (Figure 32) reveals that the relaxivity of the protonated complex (1.70 mM $s^{-1}$) is marginally lower than that of the deprotonated complex (1.83 mM $s^{-1}$). These values were determined by Equation 1.9 in Chapter 1.3.4. The relaxivity rn (where n = 1, 2 for T1 and T2 measurements respectively) can be defined from:

$$\left(\frac{1}{T_n}\right)_{obs} = \left(\frac{1}{T}\right)_{dia} + r_n[Gd] \qquad (1.9)$$

However, the values obtained are very similar to one another, presumably as a consequence of the similarity in metal binding site and solvation of the metal centre at all pHs studied.

This limits the potential of classical MRI methods using the gadolinium complex.

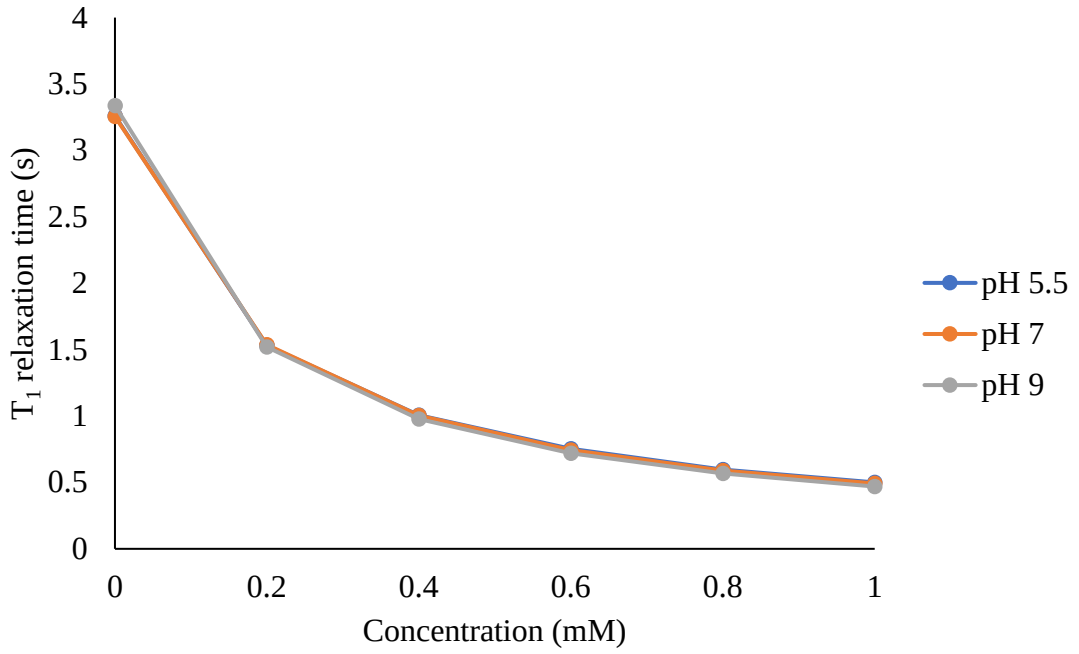



*Figure 31 – Plot of $T_1$ relaxation time over concentration of **Gd.3** at pH 5.5, 7.0 and 9.0.*

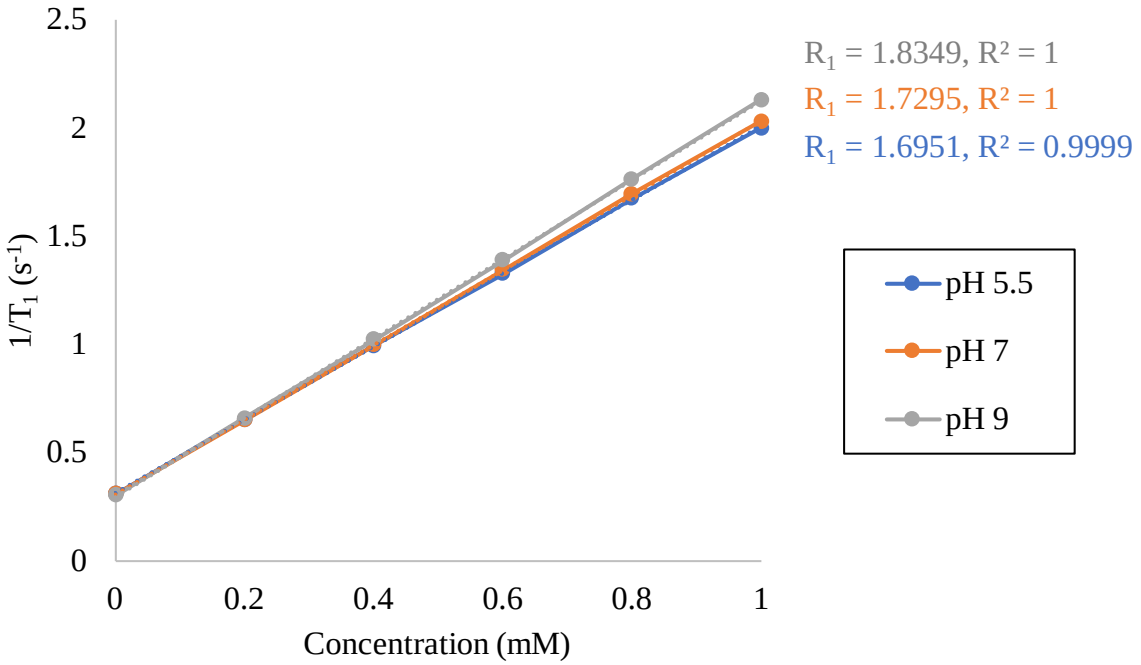



*Figure 32 - Rate of $T_1$ relaxation over concentration of **Gd.3** at pH 5.5, 7.0, and 9.0, where $R_1$ = relaxivity derived from gradient of the graph (mM $s^{-1}$) and $R^2$ = fit of the graph in the scale of 1.*

We moved to study further on phosphorescence excitation and emission measurements. Again, the same buffer systems (MES, HEPES, CHES) as the UV-Vis measurement were used to keep the pH constant for the sample of **Eu.3** in Milli-Q water, but with 1 mM concentration of buffer and 0.1 mM concentration of sample.

Phosphorescence excitation spectra illustrated in Figure 33 show that there is clear evidence that the deprotonated form is much less emissive than the protonated form, although it can be populated by energy transfer from the longer wavelength absorption band (where only it has significant absorption).

Furthermore, the observed intensity of any band reflects the product of the quantum yield and the probability of a photon being absorbed. Therefore, at pH 9.0, there is a different trend in the variation of intensities to that with the other excitation wavelengths. This follows what we have observed UV-Vis measurements (Figure 29) where the decrease in pH has shown an increase in intensity of the absorption band at 293 nm for protonated **Eu.3**. Similarly, an increase in pH has shown an increase in intensity of the absorption band at 362 nm for deprotonated **Eu.3**.

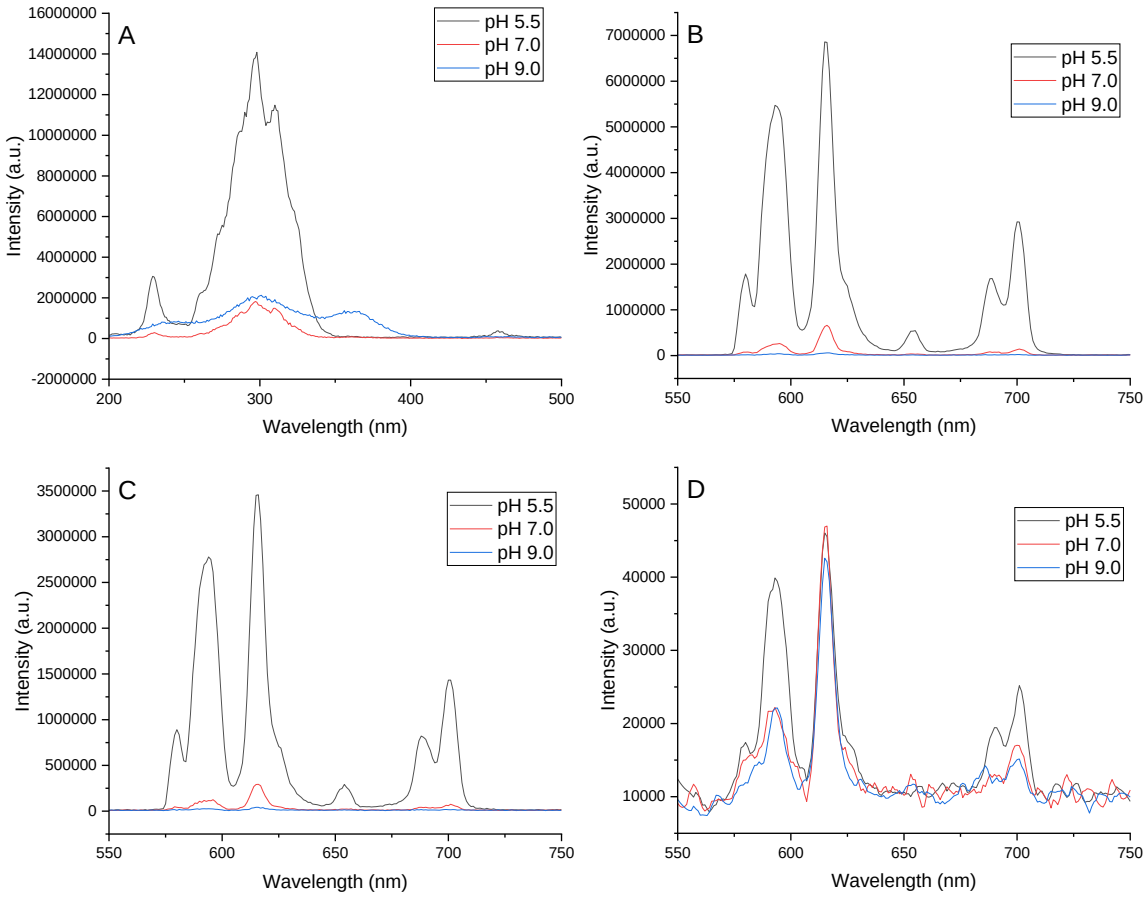



*Figure 33 - Phosphorescence spectra of* ***Eu.3*** *in pH 5.5, 7.0, 9.0 buffer systems at 25°C; excitation spectra for emission at 617 nm (A), emission spectra following excitation at 293 nm (B), 323 nm (C) and 362 nm (D), all with 1 mM concentration and excitation/emission slit width 15 nm/5 nm. Excitation wavelengths were chosen on the basis of the data in Figure 29.*

The phosphorescence emission signal diminishes with increasing pH when excited at 285 or 321 nm but increases with increasing pH for the excitation at pH 9.0. It is apparent that the protonated band prevails over the deprotonated band when it has both a large absorption and a high emissive quantum yield, but the deprotonated one wins for excitation at 365 nm where the protonated form has very little absorption.

In this complex, the pronounced effect of both excitation wavelength and pH on the observed luminescence can be ascribed to the possibility of enhanced non-radiative relaxation through

photoinduced LMCT quenching of the excited state manifold. This pathway is particularly pronounced at pH 9.0, where deprotonation is complete, and electron transfer from the phenoxide lone pair can quench the excited state manifold effectively.

Given these observations, we turned our attention to the behaviour of the europium complex as a paraSHIFT imaging agent.[192, 193] The concept of paraSHIFT NMR imaging has recently been proposed as a means to exploit the pseudo-contact shift induced by the magnetic anisotropy of a bound lanthanide and the reduction in $T_1$ for protons on the complex itself.[194-196] Furthermore, changes to the local ligand field brought on by deprotonation of the pendent hydroxyphenacyl group would give rise to changes in the local ligand field at the metal, changing the observed chemical shifts of the protons on the ligand skeleton. We decided to investigate further to see the change in the $^1$H-NMR spectra of **Eu.3** as the pD increases. $^1$H-NMR measurements were first taken on the complex before any pD adjustment as a reference and increased the pD from 5.5 to 9.0 by addition of diluted NaOD and DCl solution in D2O; pD was adjusted according to the equation: [197]

$$pD = pH + 0.45 \qquad (4.1)$$

As can be seen from Figure 34, the resonances responsible for the pseudo-axial ring protons (shown in blue box) in SAP geometry start to shift upfield from 30-36 ppm to 27-36 ppm as the pD is reduced. Additionally new peaks start to appear from pD 5.5 to pD 7.0. The $^1$H-NMR taken before any pD adjustment shows a very similar spectrum to that taken at pD 5.5 but differs slightly to pD 7.0 and pD 9.0. This probably means that the compound changes its geometry at neutral to basic pD. If we focus on the pseudo-axial ring protons from the macrocycle ring, it is clear that the result of deprotonation (and the consequent increase in

electron donor ability of the phenacyl carbonyl) is to increase the chemical shift. This is consistent with the increase in anisotropy around the metal. This approach clearly has potential for imaging pH, though practical pH imaging agents exploiting this technique will need to have a greater chemical shift differentiation and would also benefit from enhanced signal intensity. The former could easily be achieved by changing the lanthanide ion for one with greater inherent anisotropy (e.g Dy, Tb), while incorporation of chemically equivalent protons (e.g., t-butyl groups) could be used to amplify the signal at a given chemical shift.

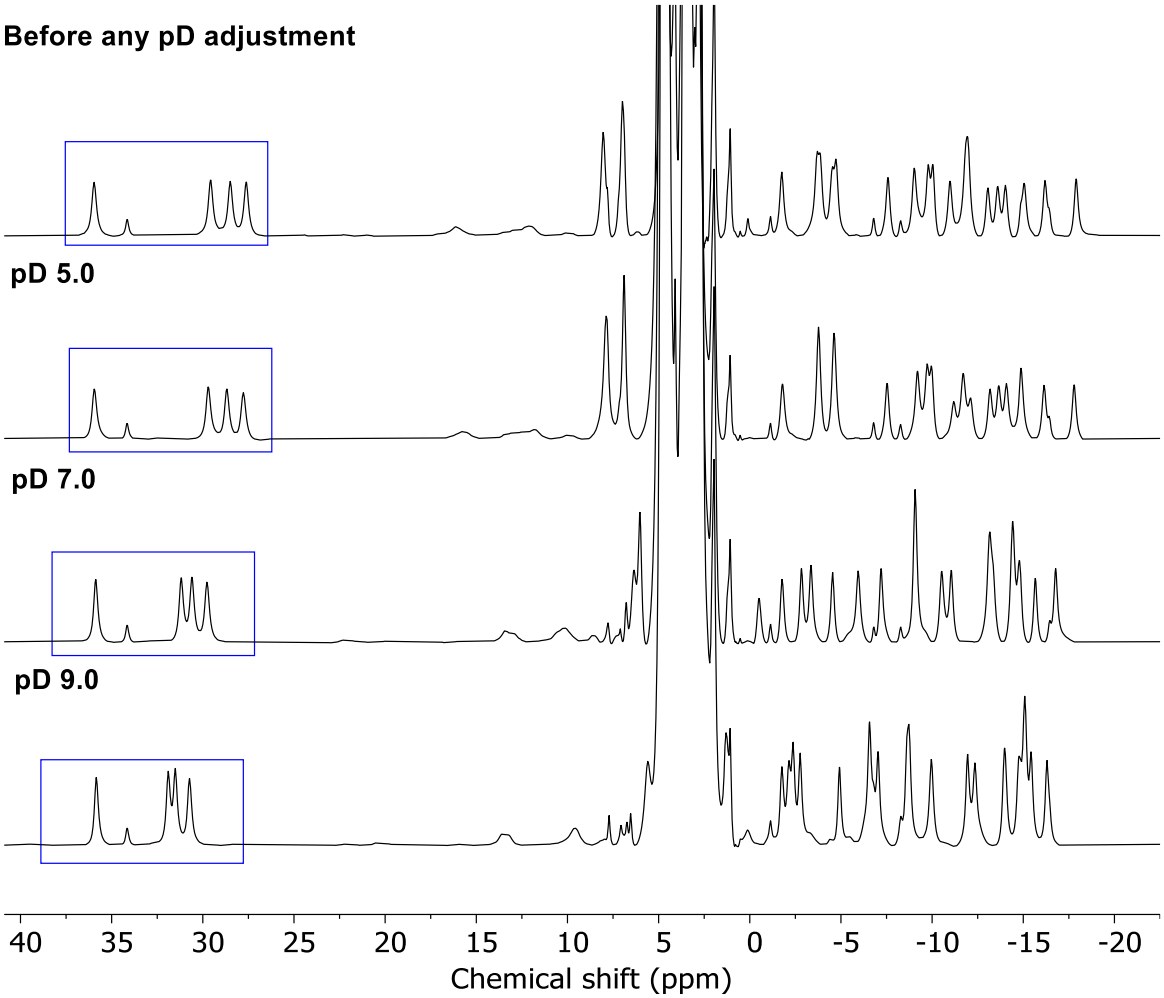



*Figure 34 - $^{1}$H-NMR (500 MHz, $D_2O$) spectra for **Eu.3** before and after pD adjustment to pD 5.5, 7.0, and 9.0, measured at 25°C.*

Overall, the effect of pH on photoluminescence and relaxivity of **Ln.3** were exploited where

the presence of two species were confirmed (protonated and deprotonated species) under UV-Vis spectroscopy to investigate the potential of **Ln.3** as an MRI contrast agent or for bioassays. The $T_1$ values obtained were very similar to one another at all pHs studied, which limits the potential of classical MRI methods using the gadolinium complex. Under proton NMR and luminescence spectroscopy, it was clear that the compound changes its geometry at neutral to basic pD or pH, as deprotonation led to the increase in electron donor ability of the phenacyl carbonyl, which shows the potential for imaging pH. However, practical pH imaging agents will need to have a greater chemical shift differentiation and an enhanced signal intensity. Therefore, it would be worth investigating **Dy.3** or **Tb.3** systems with greater inherent anisotropy as well as incorporating chemically equivalent protons (e.g., t-butyl groups) to amplify the signal at a given chemical shift.

# Chapter 5. Conclusion and Further Work

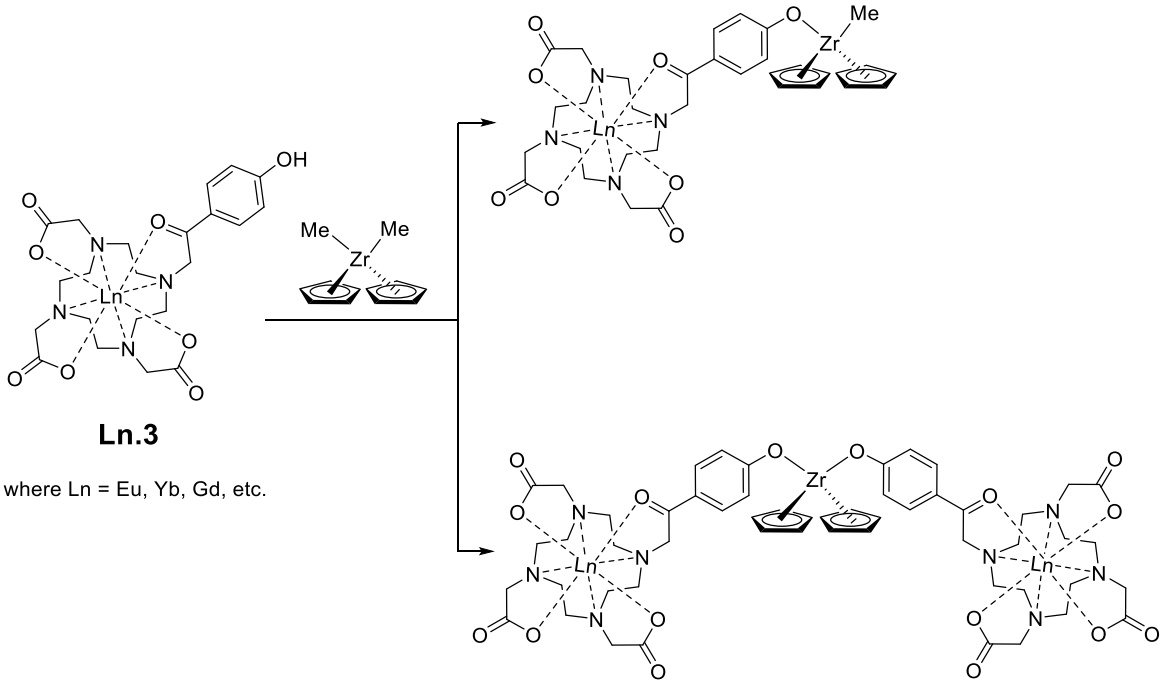
The work described in the preceding chapters illustrates the challenges and rewards that follow from incorporating a sensitising chromophore that is directly conjugated to a lanthanide centre. The hydroxyphenacyl-appended system described in the last chapter clearly shows how such a system can be exceptionally sensitive to the nature of the chromophore, while charge transfer quenching of the europium complex in the deprotonated case clearly reveals the potential to switch signals on and off. It is fortuitous that this system exhibits a pKa very close to physiological pH, and the prospect of acid mediated switching on of signals may have considerable potential in a biomedical context, once the stability of such systems in vivo has been fully assessed.

Similarly, the redox behaviour of ferrocene chromophores has been shown to be very different with conjugated acetyl ferrocene derivatives (when compared to systems where through space energy and electron transfer is the only available pathway). However, such behaviour is complex and challenges to our understanding remain. Redox reactions at both Eu and Fe can clearly be reversible or irreversible in different systems, and the reason as for this are far from clear. It was apparent that some kind of irreversible chemical change occurred upon redox cycles at metal centres which led to change in the ferrocene sensitising/quenching ability of lanthanide luminescence. A systematic study of a range of complexes is clearly needed to elucidate the available pathways in full.

Furthermore, the challenges in synthesizing systems containing conjugated chromophores mean that outcomes are unpredictable, and further work is needed before such compounds

are reliably accessible. In particular, the development of synthetic approaches to *d-f* hybrids containing non-ferrocene metallocene systems requires detailed exploration.

Elaboration of the Eu-hydroxyphenacyl complex (**Eu.3**) to incorporate a zironocene reminds to be explored in depth and requires significant scale up to permit the protonolysis of the zirconocene pendent. Due to cytotoxic effects [143-145, 198] and electrochemical properties of zirconocene, zirconocene derivatives (Scheme 10) were considered as a bioactive molecule that would be further investigated to observe its redox activity under luminescence. Its NMR spectroscopic scale protonolysis reaction has been completed with the collaboration of O'Hare group. But due to its low scale, it was very difficult to see any resonances by proton NMR spectroscopy. Therefore, larger scale can be repeated and can be further investigated on its bioactivity.




*Scheme 10 – Proposed protonolysis of **Ln.3** to form zirconocene derivatives.*

# Chapter 6. Experimental

## 6.1. Experimental Procedures and Conditions

### 6.1.1. NMR Spectroscopy

All 400 MHz NMRs were recorded on a Bruker Avance III HD nanobay 400MHz NMR. All spectra are referenced to the residual solvent peak. The chemical shifts (δ) are reported in parts per million (ppm) and coupling constants are measured in Hz. NMR abbreviations used are as follows: singlet (s), doublet (d), triplet (t), quartet (q), multiplet (m). NMR data were analysed through MestreNova software.

Relaxivity data were acquired at 298 K on a 14.1 T (600 MHz) Agilent DD2 NMR spectrometer equipped with a 5 mm z-axis gradient triple resonance room temperature probe. Longitudinal relaxation rates were measured using an inversion recovery pulse sequence. For all experiments the recycle delay time was set to at least ten times the $T_1$ time to ensure that the magnetisation is fully relaxed back to equilibrium prior to the inversion pulse. Spectra were subsequently phased and Fourier transformed using NMR pipe. Peak intensities for each relaxation delay were integrated and fit to the equation:

$$S(t) = S(\infty)(1 - 2e^{-R_1 t}) \qquad (6.1)$$

*where S is the signal intensity and S(∞) and $R_1$ are fitting parameters using in-house python scripts that utilize the LMFIT and nmrGlue modules.*

All relaxivity data were analysed by TopSpin software.

### 6.1.2. MS

All electron ionisation mass spectrometry for compounds was done on an Agilent Technology 1260 Infinity or a Waters LCT Premier XE spectrometer. For systems purified by HPLC, LC-MS were measured by a Waters LCT Premier bench-top orthogonal acceleration time-offlight LC-MS system. MS data were analysed through MestreNova software.

### 6.1.3. Absorption and Luminescence Measurements

All luminescence data for lanthanide complexes were obtained on a HORIBA Jobin Yvon Fluorolog 3 fluorimeter equipped with Hamamatsu R928 detector, a double-grating emission monochromator and Xenon flash lamp for measuring emission lifetimes. All excitation, emission and lifetime measurements were measured at room temperature. Luminescence lifetimes were analysed by tail fit for Eu(III) complexes using Origin software.

All UV/Vis data was obtained on a Jasco V-770 UV-Visible/NIR spectrophotometer operated under Spectra Manager TM suite. Points were recorded at 0.2 nm interval with UV-Vis bandwidth of 1 nm, UV-Vis response of 0.06 sec in Continuous scan mode at the rate of 400 nm per min. All UV-Vis and lanthanide data analysis was done using OriginPro 9.7 or Microsoft Excel software. The Compact flow-through Cuvettes with screw connections made of High Performance Quartz glass (3 × 3 mm light path) were purchased from Hellma Analytics.

### 6.1.4. Reagents and Solvents Preparation

Dry solvents were obtained from a Mbraun MB SPS-800 or was purchased from Merck. Cyclen was purchased from Chematech. Lanthanide salts were purchased from Strem Chemical, all other reagents including DOTA were obtained from Sigma-Aldrich (Merck), Alfa Aesar and Fluorochem.

Distilled water and deionised water were used throughout the study. Deionised water was obtained from Milli-Q® Ultrapure Water System and Elga PURELAB® Chorus complete with conductivity of 18.2 MΩ.cm.

Buchi Rotavapor® R-200 Rotary Evaporator was used to concentrate solvents *in vacuo* and compounds were further dried in high-vac Schlenk line with an Edwards RV3 Vacuum Pump for all spectroelectrochemical and spectroscopic measurements.

### 6.1.5. Dialysis, Centrifugation, TLC and Column (flash) Chromatography

Spectra-Por® Float-A-Lyzer® G2 dialysis membrane tubing equipped with regenerated cellulose and a molecular weight cut-off of 500 or 1000 MW (Spectrum Labs) were used to purify the lanthanide complexes. The dialysis tube was activated by 10% ethanol solution in Milli-Q water followed by gentle stir of the membrane in Milli-Q water before every use. The complexes were dissolved in Milli-Q water and transferred into dialysis tube. The dialysis tube was placed in a 5L-beaker filled with Milli-Q water. The dialysis lasts for at least two days under stirring and the Milli-Q water was replaced with fresh Milli-Q water every 2-8 h during dialysis. Centrifugations were performed using Beckman Coulter® Allegra® X-12R Benchtop Centrifuge. All centrifugations were performed at 3750 RPM for

15 min at 4 °C. Column chromatography was performed using silica gel 60 (70-230 mesh, Carl Roth) and neutral alumina (activated, Brockmann grade II). Analytical thin layer chromatography (TLC) was performed on aluminium sheet supported silica gel plates coated with silica gel 60 F254 (0.2 mm, Merck) and aluminium sheet supported plates coated with neutral alumina 60 F254 (0.2 mm, Merck) using different eluents as mobile phase. The compounds were visualized in TLC under UV light or by staining the plate with potassium permanganate, followed using the previously reported method from a literature. [199]

### 6.1.6. pH Meter and Buffer Preparation

Hanna Instruments pH 210 Microprocessor pH Meter with a HI 1131B electrode was used for the pH measurements of complexes in water and deuterium oxide. Prior to pH Meter use, the pH meter was calibrated using pH 4.01 (or 10.01) and 7.01 buffer solutions, purchased from Hannah Instruments. The electrodes were cleaned by inorganic cleaning solution for 15-20 min before use and stored in storing solution after use(both solutions purchased from Hannah Instruments). The electrodes were washed with Milli-Q water in between every pH measurement. In deuterium oxide, the pD of the solution was determined using the equation, pD = pH + 0.45, where pH refers to the pH meter calibrated reading in Milli-Q water. [197, 200]

Each buffer was prepared by dissolving appropriate amount of buffer salt (e.g. Trizma base, HEPES, CHES etc.) to 9 mL of Milli-Q water followed by the dropwise addition of 10 mM or 100 mM aqueous solutions of HCl or NaOH until it reached the desired pH value under pH meter. Then Milli-Q water was added to reach 10 mL to obtain the buffer. Each buffer was at least 10 times more concentrated than the concentration of the sample of interest to allow effective adjustment of pH by buffer.

### 6.1.7. HPLC

HPLC was performed using a Waters Autopurification system, equipped with an ACQUITY QDa performance mass spectrometer and UV-Vis absorption spectrometer. UV-Vis absorption spectra were performed on the HPLC. Crude samples were dissolved in 5% MeCN in Milli-Q water and filtered through a syringe filter (nylon, ionic membrane, 0.2 μM, Merck). Two eluents were used in acidic condition (pH 2); 0.1% formic acid in Milli-Q® water (Milipore, Merck) and 0.1% formic acid in HPLC-grade MeOH were used as eluents A and B respectively. Following gradient of solvents (A and B) was used for both analytical and preparative HPLC:

| Time (min) | Eluent A (v/v %) | Eluent B (v/v %) |
|---|---|---|
| 0 | 95 | 5 |
| 1 | 90 | 10 |
| 8 | 25 | 75 |
| 9 | 5 | 95 |
| 10 | 95 | 5 |

For Analytical HPLC, samples were injected in 5 μL aliquots using Waters X-bridge® $C_{18}$ column (5 μm, 4.6 mm × 50 mm) with a flow rate of 1 mL/min and an injection loop of 0.02 mL.

For Preparative HPLC, samples were injected in 750 μL aliquots using X-bridge® BEH $C_{18}$

OBD™ Semi-Prep Column, 130 Å (5µm, 19 mm × 50 mm) with 1 mL injection loop and a flow rate of 20 mL/min.

## 6.2. General Methods

### 6.2.1. General Procedure 1: Lanthanide Complexation

A procedure from the literature [201] was modified as follows:

Compounds with DO3A or DOTA moiety and europium triflate was dissolved in minimal amount of MeOH and was stirred at 60 °C for 30 mins. Then a 1M NaOH solution was added to the reaction mixture to adjust the pH to 5 and this solution was heated under reflux at 60 °C for 48 h. The reaction mixture was concentrated *in vacuo* and the white residue was redissolved in deionised water. The pH was adjusted to 10 to remove excess europium ions as precipitate europium hydroxide. The reaction mixture was centrifuged and syringe-filtered to remove any precipitates. The filtrate was neutralised to pH 7 using 1M HCl solution and the concentrated under reduced pressure and the residue was purified by dialysis to yield the desired product.

### 6.2.2. General Procedure 2: Deprotection of acid groups

The procedure from literature [201] was modified as follows:

Trifluoroacetic acid was added dropwise to a solution of DO3A-tBu or DOTA-tBu derivatives in $CH_2Cl_2$ at 0 °C and the reaction mixture was left to warm to rt and stir overnight. The reaction mixture was concentrated *in vacuo* and triturated by dissolving the compound in a minimal amount of MeOH and adding excess amount of diethyl ether. The mixture was filtered to yield the desired product.

### 6.2.3. General Procedure 3: Attachment of DO3A to a ligand

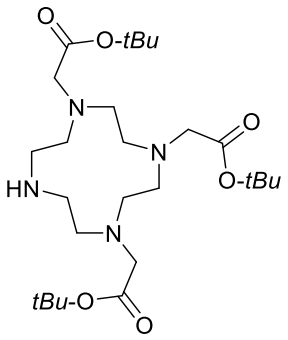
The procedure from literature [53, 202] was modified as follows:

DO3A-tBu was dissolved in minimal amount of acetonitrile and potassium carbonate or caesium carbonate and potassium iodide catalyst were added. The reaction mixture was refluxed for 30 minutes and a ligand was added, which was refluxed at 80 ℃ overnight. This was concentrated *in vacuo* and was purified under flash chromatography to yield the desired product.

## 6.3. Synthetic Methods

### 6.3.1. Products and Intermediates used for Luminescence Studies

**DO3A-tBu**

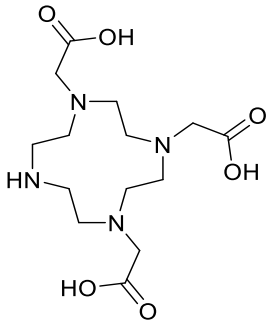



A procedure from the literature [53, 202] was modified as follows:

Cyclen (5.00 g, 29.0 mmol, 1.00 eq) and sodium bicarbonate (8.53 g, 102 mmol, 3.52 eq) was dissolved in acetonitrile (100 mL) and stirred at rt for 30 mins. tert-butylbromoacetate (18.7 g, 95.7 mmol, 3.30 eq) in acetonitrile (20.0 mL) was added dropwise at 0℃ to the stirring mixture of cyclen and sodium bicarbonate. The reaction mixture was left to warm to rt and stir overnight. The suspension was filtered and the filtrate was concentrated *in vacuo*

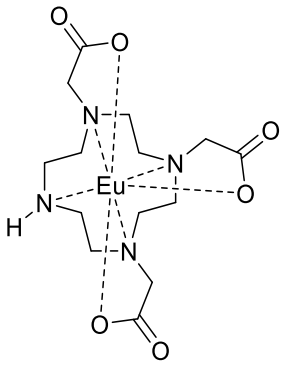
to white powder. The white precipitate was washed with toluene (200 mL) until filtrate is colourless. The white precipitate was recrystallised from hot toluene to yield the white powder of DO3A-tBu.HBr (9.851 g, 66.0%); $^{1}$H-NMR (400 MHz, $CDCl_3$) δ 10.02 (s, 1H), 3.37 (s, 4H), 3.29 (s, 2H), 3.10 (m, 4H), 2.97 – 2.83 (m, 12H), 1.45 (m, 27H).; ESI-MS m/z 515.

**DO3A**



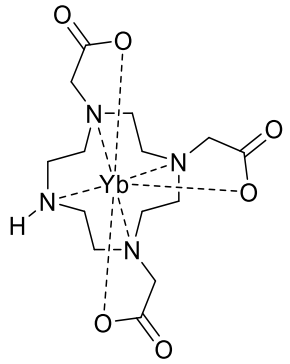

General procedure 2 was followed using TFA (2.39 mL, 31.1 mmol, 79.7 eq), DO3A-tBu.HBr (0.200 g, 0.389 mmol, 1.00 eq) in DCM (3 mL) to yield the white precipitate of DO3A (0.140 g, 89.0%); $^{1}$H-NMR (400 MHz, $D_2O$): δ 3.98 (s, 2H) 3.64 (s, 2H), 3.56-3.43 (m, 8H), 3.38 – 3.33 (m, 2H), 3.24 – 3.04 (m, 6H) 2.93 (m, 2H). ESI-MS *m/z* $[M+H]^+$ 347.

**Eu-DO3A**



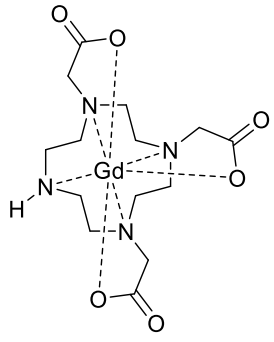
General procedure 1 was followed using DO3A (0.100 g, 0.289 mmol, 1.00 eq) and Eu triflate (0.190 g, 0.318 mmol, 1.10 eq) to obtain Eu-DO3A (0.129 g, 90.0%); $^{1}$H-NMR (400 MHz, $D_2O$): Only peaks outside 0 – 10 ppm are reported: δ 33.98, 32.70, 22.29, 20.46, 15.77, 10.01, -3.26, -5.13, -7.40, -9.14, -11.91, -17.30; ESI-MS *m/z* $[M+H]^+$ 496, $[M+Na]^+$ 518.

**Yb-DO3A**



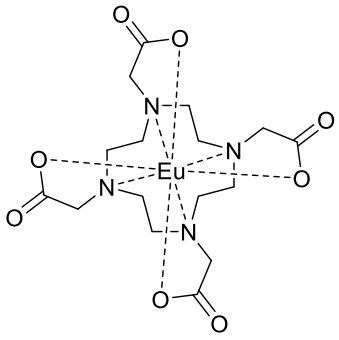

General procedure 1 was followed using DO3A (0.100 g, 0.289 mmol, 1.00 eq) and Eu triflate (0.190 g, 0.318 mmol, 1.10 eq) to obtain Yb-DO3A (0.133 g, 89.3%); $^{1}$H-NMR (400 MHz, $D_2O$): Only peaks outside 0 – 10 ppm are reported: δ 126.18, 114.14, 81.95, 60.98, 41.38, 33.13, 24.38, 19.98, 10.93, 7.91, 6.07, -9.08, -37.39, -47.98, -50.24, -55.57, -66.36, -72.57, -81.88, -95.17; ESI-MS *m/z* $[M+H]^+$ 496, $[M+Na]^+$ 518.

**Gd-DO3A**



General procedure 1 was followed using DO3A (0.100 g, 0.289 mmol, 1.00 eq) and Eu triflate (0.190 g, 0.318 mmol, 1.10 eq) to obtain Gd-DO3A (0.132 g, 91.1%); ESI-MS *m/z* $[M+H]^+$ 496, $[M+Na]^+$ 518.

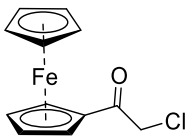
**Eu-DOTA**




General procedure 1 was followed using DOTA (20.0 mg, 49.5 μmol, 1.00 eq) and Eu triflate (32.6 mg, 54.5 μmol, 1.10 eq) to obtain Eu-DOTA (24.7 mg, 90.5%). $^1$H-NMR (400 MHz, $D_2O$): Only peaks outside 0 – 10 ppm are reported: δ 33.84, 13.45, -1.13, -2.32, -6.76, -8.14, -14.70, -16.18: Two sets of five broad singlets appeared on $^1$H NMR spectrum due to the isomerization.

### 6.3.2. Ferrocene-related Products and Intermediates

**Chloroacetylferrocene**

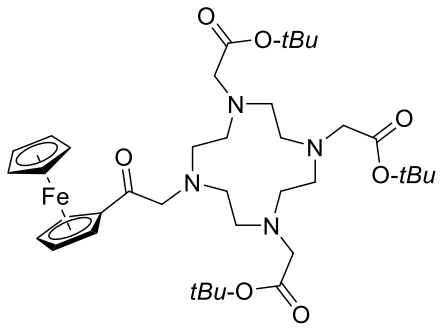



A procedure from literature [203] was modified as follows:

Chloroacetyl chloride (0.282 mL, 3.53 mmol, 0.654 eq) was added dropwise to the solution of ferrocene (1.00 g, 5.40 mmol, 1.00 eq) in 20 mL of DCM and the solution was cooled to

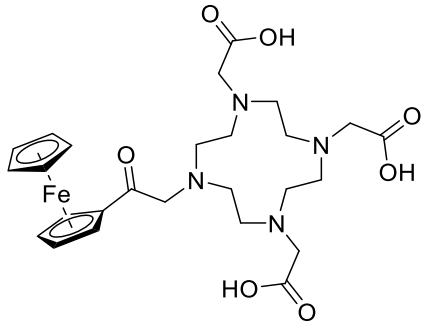
-75 °C. Anhydrous aluminium trichloride (0.476 g, 10.8 mmol, 2.00 eq) was then added slowly, for a period of 4 h, while maintaining the temperature, and the mixture was subsequently allowed to reach rt and stir overnight. The reaction was quenched with ice and the mixture was extracted with DCM (3 × 30 mL). The organic extracts were dried with anhydrous magnesium sulfate and evaporated to dryness, yielding a brown solid. This solid was homogenized with celite and then purified by flash chromatography using $CH_2Cl_2$/pentane 1:2 as the eluent, to yield a dark red crystalline product of chloroacetylferrocene (0.953 g, 67.2%); Rf 0.29 [$SiO_2$, $CH_2Cl_2$/pentane 1:2]; $^1$H-NMR (400 MHz, $CDCl_3$) δ 4.82 (s, 2H), 4.58 (s, 2H), 4.41 (s, 2H), 4.22 (s, 5H); ESI-MS *m/z* $[M+H]^+$ 264.

**Acetylferrocene.DO3A-tBu**



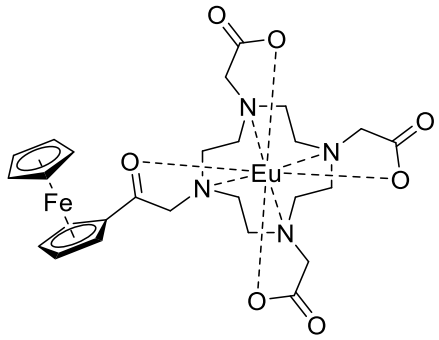

General procedure 3 was followed using DO3A-tBu (565 mg, 0.95 mmol, 1.00 eq), chloroacetylferrocene (275 mg, 1.05 mmol, 1.10 eq), potassium carbonate (325 mg, 2.38 mmol, 2.50 eq), potassium iodide (20.0 mg) and acetonitrile (40 mL), purified by flash chromatography ($Al_2O_3$, MeOH/DCM 0:10 to 1:10, gradient) to yield dark red crystalline of acetylferrocene.DO3A (0.179 g, 25.5%); Rf 0.35 [$SiO_2$, $CH_2Cl_2$/MeOH 97:3]; $^1$H-NMR (400 MHz, $CDCl_3$) δ 4.74 (s, 2H), 4.52 (t, $^3J_{HH}$ = 2.0 Hz, 2H), 4.22 (s, 5H), 3.68 (bs, 2H), 3.30-2.17 (m, 22H), 1.45 (s, 27H); ESI-MS *m/z* $[M+H]^+$ 741.

**Acetylferrocene.DO3A**



General procedure 2 was followed using acetylferrocene.DO3A-tBu (0.572 g, 0.772 mmol, 1.00 eq), TFA (4.73 mL, 65.3 mmol, 80.0 eq) and DCM (4.73 mL) to yield dark red crystalline of acetylferrocene.DO3A (0.442 g, 95.6%); $^{1}$H-NMR (500 MHz, $(CD_3)_2CO$): δ 7.73 (bs, 3H) 4.91 (s, 2H), 4.70 (s, 2H) 4.35 (s, 5H), 3.85-3.30 (m, 16H); ESI-MS *m/z* $[M+H]^+$ 573.

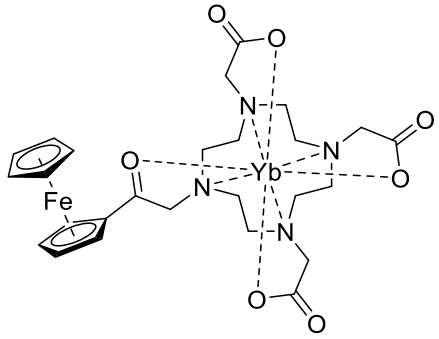
**Eu.Acetylferrocene.DO3A (Eu.2)**



General procedure 1 was followed using 2,2',2''-(1,4,7,10-tetraazacyclododecane-1,4,7-triyl)triacetic acid (100 mg, 0.22 mmol, 1.00 eq) and Eu triflate (145 mg, 0.24 mmol, 1.10 eq) to obtain red-purple powder of Eu.Acetylferrocene.DO3A (0.143 g, 90.0%). $^{1}$H-NMR (400 MHz, $D_2O$): Only peaks outside 0 – 10 ppm are reported: δ 35.31, 34.17, 30.48, 28.52,

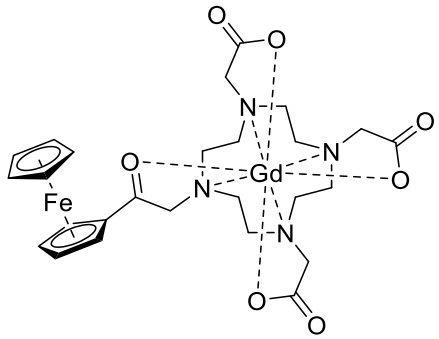
13.89, 13.10, 12.36, 12.04, 3.36, -1.02, -2.45, -3.11, -4.59, -6.70, -8.16, -9.41, -12.74, -13.79, -14.68, -16.16, -18.03); ESI-MS *m/z* $[M+H]^+$ 722.

**Yb.Acetylferrocene.DO3A, (Yb.2)**




General procedure 1 was followed using 2,2',2''-(1,4,7,10-tetraazacyclododecane-1,4,7-triyl)triacetic acid (100 mg, 0.22 mmol, 1.00 eq) and Yb triflate (150 mg, 0.24 mmol, 1.10 eq) to obtain dark red powder of Yb.Acetylferrocene.DO3A (0.148 g, 90.5%); $^1$H-NMR (400 MHz, $D_2O$): Only peaks outside 0 – 10 ppm are reported: δ 35.31, 34.17, 30.48, 28.52, 13.89, 13.10, 12.36, 12.04, 3.36, -1.02, -2.45, -3.11, -4.59, -6.70, -8.16, -9.41, -12.74, -13.79, -14.68, -16.16, -18.03; ESI-MS *m/z* $[M+H]^+$ 743.

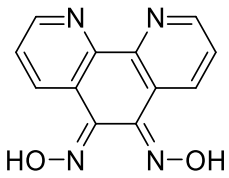
**Gd.Acetylferrocene.DO3A (Gd.2)**



General procedure 1 was followed using 2,2',2''-(1,4,7,10-tetraazacyclododecane-1,4,7-triyl)triacetic acid (100 mg, 0.22 mmol, 1.00 eq) and Gd triflate (146 mg, 0.24 mmol, 1.10 eq) to obtain red-brown powder of Gd.Acetylferrocene.DO3A (0.143 g, 89.5%); ESI-MS *m/z* $[M+H]^+$ 728, $[M+Na]^+$ 750.

### 6.3.3. Phenanthroline-related Products and Intermediates

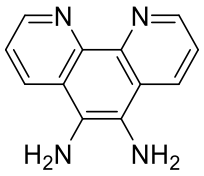
**1,10-Phenanthroline-5,6-dioxime (B1)**




A procedure from the literature[190] was modified as follows:

A mixture of hydroxyl amine hydrochloride (0.500 g, 2.30 mmol, 1.00 eq) and barium carbonate (0.715 g, 3.62 mmol, 1.58 eq) in ethanol (30.0 mL) was heated under reflux and the suspension was left to stir for 14 h. The brownish yellow residue was obtained after flash evaporating. The residue was treated with aqueous 0.2 M HCl (60.0 mL), stirred for 45 mins, and filtered. The greenish-yellow solid was washed thoroughly with water, ethanol and diethyl ether successively and dried under vacuum to yield a green powder of 1,10-phenanthroline-5,6-dioxime (0.403 g, 73.0%); $^1$H-NMR (400MHz, $CD_3OD$-$d^6$): δ 12.99 - 12.92 (s, 2H, OH), 8.80 (t, $^3J_{HH}$ = 2.7 Hz, 2H), 8.32 – 8.18 (m, 2H), 7.60 – 7.47 (m, 2H); the product was not visible under ESI-MS and MALDI due to its bad solubility.

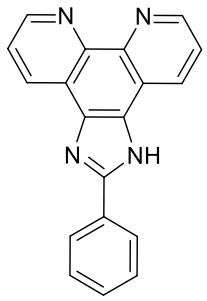
**1,10-Phenanthroline-5,6-diamine (C1)**



A procedure from the literature[190] was modified as follows:

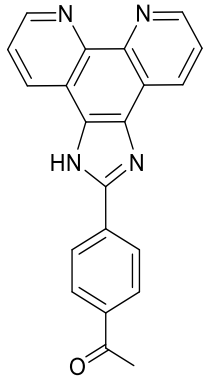
The reaction and workup were performed under argon atmosphere. A slurry of 1,10-phenanthroline-5,6-dioxime (250 mg, 1.19 mmol, 1.00 eq), Pd/C (10 % on activated carbon, Strem) (98.8 mg, 0.470 mmol, 0.390 eq), and ethanol (30.0 mL) was purged with Nitrogen gas, then heated to reflux. A mixture of ethanol (3.50 mL) and hydrazine monohydrate (2.50 mL, 51.54 mmol, 43.3 mmol) was added dropwise over 1 h and the reaction mixture was subsequently heated under reflux overnight. The hot mixture was then filtered through a bed of celite which was then washed with hot ethanol (3 × 15 mL). The solvent was removed from the filtrate *in vacuo*, and the resulting solid was triturated with water and left to sit overnight in a fridge at 4 °C. The mixture was then filtered, washed with cold distilled water (50.0 mL), and concentrated *in vacuo* to produce yellow/tan powder. The product was stored under inert atmosphere, exposure to air led to slow decomposition over the course of several days, indicated by a colour change from yellow to brown (0.175 g, 70.2%); $^{1}$H-NMR (400MHz, DMSO-d$^{6}$): δ 8.77 (dd, $^{4}J_{HH}$ = 4.2 Hz, $^{3}J_{HH}$ =1.6 Hz, 2H), 8.48 (dd, $^{4}J_{HH}$ = 8.4 Hz, $^{3}J_{HH}$ = 1.6 Hz, 2H), 7.60 (dd, $^{4}J_{HH}$ = 8.4 Hz, $^{3}J_{HH}$ = 4.2 Hz, 2H), 5.22 (s, 4H, NH); ESI-MS *m/z* $[M+H]^{+}$ 210.

**2-Phenyl-1H-imidazo[4,5-f][1,10]phenanthroline**



1,10-phenanthroline-5,6-diamine (50.0 mg, 0.238 mmol, 1.00 eq) was added to benzaldehyde (25.2 mg, 0.238 mmol, 1.00 eq) in ethanol (5.00 mL) under argon. The reaction was left to stir and heated to 75 ℃ for 24 h. The reaction mixture was filtered and washed with ice-cold ethanol (20.0 mL) to yield peach powder of 2-phenyl-1H-imidazo[4,5-f][1,10]phenanthroline (62.8 mg, 89.0%); $^{1}$H-NMR (400MHz, DMSO-d$^{6}$): δ 14.34 (s, 1H), 9.28 (d, $^{3}J_{HH}$ = 8.2 Hz, 1H), 9.03 (d, 2H), 8.97 (d, $^{3}J_{HH}$ = 8.2 Hz, 1H), 8.45 – 8.41 (m, 2H), 7.86 (h, $^{3}J_{HH}$ = 4.5 Hz, 1H), 7.64 – 7.57 (m, 2H), 7.52 (tt, $^{4}J_{HH}$ = 7.3 Hz, $^{3}J_{HH}$ = 1.3 Hz, 1H); ESI-MS *m/z* $[M+H]^{+}$ 297.

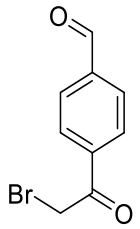
**1-(4-(1H-Imidazo[4,5-f][1,10]phenanthrolin-2-yl)phenyl)ethan-1-one (D2)**



1,10-phenanthroline-5,6-diamine (50.0 mg, 0.238 mmol, 1.00 eq) and 4-acetylbenzaldehyde (42.3 mg, 0.285 mmol, 1.20 eq) in ethanol (5.00 mL) was heated under reflux at 75 ℃ for 24 h. The reaction mixture was filtered and washed with ice-cold ethanol (30.0 mL) to yield peach powder of 1-(4-(1H-imidazo[4,5-f][1,10]phenanthrolin-2-yl)phenyl)ethan-1-one

(36.4 mg, 45.2%); Rf 0.39 [$SiO_2$, $CH_2Cl_2$/MeOH 97:3]; $^1$H-NMR (400MHz, DMSO-d$^6$): δ 13.92 (s, 1H), 9.04 (dd, $^4J_{HH}$ = 4.5 Hz, $^3J_{HH}$ = 1.7 Hz, 2H), 8.92 (dd, $^4J_{HH}$ = 8.1 Hz, $^3J_{HH}$ = 1.8 Hz, 2H), 8.39 (d, $^3J_{HH}$ = 8.4 Hz, 2H), 8.16 (d, $^3J_{HH}$ = 8.4 Hz, 2H), 7.84 (s, 2H), 2.65 (s, 3H); the product was not visible under EI-MS due to its bad solubility. $^1$H-NMR spectrum shown in the Supplementary Data.

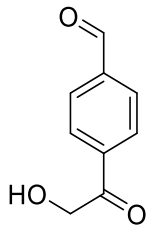
**4-(2-Bromoacetyl)benzaldehyde (B2)**




A procedure from the literature[204] was modified as follows:

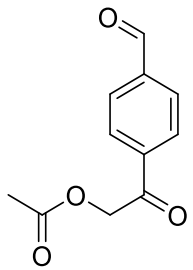
A mixture of 4-acetylbenzaldehyde (0.500 g, 3.37 mmol, 1.00 eq) and copper bromide (1.12 g, 5.06 mmol, 1.50 eq) in 1:1 chloroform/ethyl acetate (120 mL) was heated under reflux at 60 °C overnight. The completion of the reaction was shown by disappearance of black solid and cessation of hydrogen bromide formation. The reaction mixture was filtered to remove copper (I) bromide and washed with ethyl acetate (20.0 mL). The filtrate was concentrated *in vacuo* and purified by flash column chromatography (eluted with toluene) to yield a light yellow precipitate of 4-(2-bromoacetyl)benzaldehyde (0.515 g, 67.3%); Rf 0.35 [$SiO_2$, toluene]; $^1$H-NMR (400 MHz, $CDCl_3$): δ 10.04 (s, 1H), 8.06 (dt, $^4J_{HH}$ = 8.3 Hz, $^3J_{HH}$ = 1.8 Hz, 2H), 7.93 (dt, $^4J_{HH}$ = 8.5 Hz, $^3J_{HH}$ = 1.8 Hz, 2H), 4.41 (s, 2H); ESI-MS *m/z* $[M+H]^+$ 228; isotope pattern of Br was shown under ESI-MS.

**4-(2-Hydroxyacetyl)benzaldehyde**



4-(2-bromoacetyl)benzaldehyde (57.6 mg, 0.254 mmol, 1.00 eq) and sodium formate (51.8 mg, 0.761 mmol, 3.00 eq) in MeOH (750 μL) at rt was left to stir for 24 h, until silica thin layer chromatography shows the completion of the reaction. The filtrate was concentrated *in vacuo*. The residue was dissolved in ethyl acetate, washed with water and brine solution (30.0 mL), and dried over $Na_2SO_4$ and concentrated *in vacuo*. The crude product was purified by flash silica column chromatography (DCM/MeOH 100:0 to 95:5 gradient) to yield white powder of 4-(2-hydroxyacetyl)benzaldehyde (5.00 mg, 12.1%); $R_f$ 0.39 [$SiO_2$, $CH_2Cl_2$/MeOH 97:3]; $^1$H-NMR (400 MHz, $CDCl_3$): δ 10.12 (s, 1H), 8.08 (d, $^3J_{HH}$ = 8.3 Hz, 2H), 8.02 (dd, $^4J_{HH}$ = 8.4, $^3J_{HH}$ = 1.7 Hz, 2H), 4.93 (d, $^3J_{HH}$ = 4.3 Hz, 2H); ESI-MS *m/z* $[M+H]^+$ 165, $[M+Na]^+$ 187.

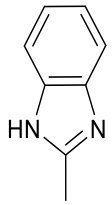
**2-(4-Formylphenyl)-2-oxoethyl acetate (C2)**



A mixture of 4-(2-bromoacetyl)benzaldehyde (0.200 g, 0.880 mmol, 1.00 eq) and sodium acetate (0.361 g, 4.40 mmol, 4.00 eq) in acetonitrile (8.80 mL) was heated under reflux for 14 h at 60 °C. After the starting material being fully consumed was observed by thin layer chromatography, the solid was filtered and concentrated *in vacuo.* The crude product was

then purified by flash silica column chromatography (Pentane/EtOAc 85:15 to 70:30, gradient) to yield a white powder of 2-(4-formylphenyl)-2-oxoethyl acetate (110 mg, 66.1%); $^{1}$H-NMR (400 MHz, $CDCl_3$): δ 10.11 (s, 1H), 8.08 – 8.04 (m, 2H), 8.03 – 7.98 (m, 2H), 5.34 (s, 2H), 2.23 (s, 3H); the product is not visible under ESI-MS.

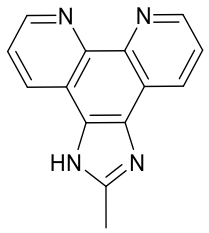
**2-Methyl-1H-benzo[d]imidazole**




A procedure from the literature[205] was modified as follows:

Benzene-1,2-diamine (0.100 g, 0.925 mmol, 1.00 eq) was dissolved in dry dioxane (5.55 mL) at a temperature of 0 °C and left to stir for 20 mins at rt, before acetyl chloride (79.0 μL, 1.11 mmol, 1.20 eq) was added dropwise, the solution was left to stir for 30 mins at rt to give the intermediate product of N-acyl-1,2-phenylenediamine in the reaction mixture. Boron trifluoride etherate (126 μL, 1.02 mmol, 1.10 eq) was added to the reaction mixture and the reaction mixture was heated under reflux for 2.5 h at 130 °C. The reaction mixture was then concentrated *in vacuo* and purified by flash silica column chromatography (DCM/MeOH 100:0 to 90:10 gradient) to yield a red/orange powder of 2-methyl-1H-benzo[d]imidazole (81.7 mg, 66.8%); $R_f$ 0.52 [$SiO_2$, DCM/MeOH 95:5]; $^{1}$H-NMR (400 MHz, DMSO): δ 7.61 (dd, $^{4}J_{HH}$ = 7.1 Hz, $^{3}J_{HH}$ = 3.6 Hz, 2H), 7.32 (dd, $^{4}J_{HH}$ = 6.6 Hz, $^{3}J_{HH}$ = 3.7 Hz, 2H), 5.75 (s, 1H), 2.64 (s, 3H); ESI-MS *m/z* $[M+H]^+$ 132.

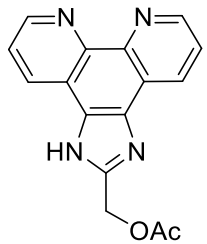
**2-Methyl-1H-imidazo[4,5-f][1,10]phenanthroline (D1)**



A procedure from the literature[205] was modified as follows:

Acetyl chloride (55.8 μL, 0.785 mmol, 1.10 eq) was added to 1,10-phenanthroline-5,6-diamine (0.150 g, 0.713 mmol, 1.00 eq) in dry 1,4-dioxane (5.71 mL) at 0 °C and was left to stir for 30 mins at rt to give the intermediate product of N-acyl-1,2-phenylenediamine in the reaction mixture. Boron trifluoride etherate (185 μL, 1.498 mmol, 2.10 eq) was added to the reaction mixture and the reaction mixture was heated under reflux overnight at 130 °C. The dark brown mixture was concentrated *in vacuo* and purified by flash alumina gel column chromatography (DCM/MeOH/$NH_4OH$ 90:10:0 to 50:50:0 to 50:40:10 gradient) to yield a red/orange powder of 2-methyl-1H-imidazo[4,5-f][1,10]phenanthroline (0.107 g, 64.1%); $R_f$ 0.30 [$SiO_2$, DCM/MeOH/$NH_4OH$ 75:23:2]; $^1$H-NMR (400 MHz, DMSO): δ 13.41 (s, 1H), 8.99 (d, $^3J_{HH}$ = 1.7 Hz, 2H), 8.90 – 8.64 (m, 2H), 7.87 – 7.76 (m, 2H), 2.66 (s, 3H); ESI-MS *m/z* $[M+H]^+$ 235, $[M+Na]^+$ 257.

**(1H-Imidazo[4,5-f][1,10]phenanthrolin-2-yl)methyl acetate (E1)**

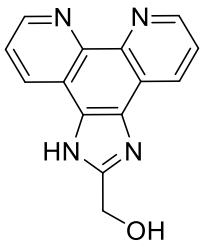


A procedure from the literature[205] was modified as follows:

Acetoxyacetyl chloride (70.0 μL, 0.656 mmol, 1.00 eq) was added to 1,10-phenanthroline-

5,6-diamine (0.125 g, 0.594 mmol, 1.10 eq) in dry 1,4-dioxane (4.75 mL) at 0 ℃ and was stirred for 30 mins at rt to give the intermediate product of N-acyl-1,2-phenylenediamine in the reaction mixture. Boron trifluoride etherate (178 μL, 1.250 mmol, 2.10 eq) was added to the reaction mixture and the reaction mixture was heated to reflux overnight at 130 ℃. The dark brown mixture was concentrated *in vacuo* and purified by flash alumina gel column chromatography (MeCN/$H_2O$ 100:0 to 50:50 gradient) to yield a red/orange powder of 2-methyl-1H-imidazo[4,5-f][1,10]phenanthroline (61.1 mg, 35.2%); $R_f$ 0.55 [$SiO_2$, DCM/MeOH/$NH_4OH$ 75:23:2]; $^1$H-NMR (400MHz, DMSO-d$^6$): δ 13.83 (s, 1H), 9.03 (dd, $^4J_{HH}$ = 4.3, $^3J_{HH}$ = 1.7 Hz, 2H), 8.85 – 8.77 (m, 2H), 7.86 – 7.78 (m, 2H), 5.40 (s, 2H), 2.15 (s, 3H); ESI-MS *m/z* $[M+H]^+$ 293, $[M+Na]^+$ 315.

**(1H-Imidazo[4,5-f][1,10]phenanthrolin-2-yl)methanol (F1)**

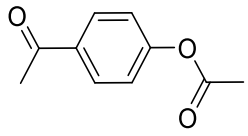



2M NaOH solution (1.97 mL, 3.59 mmol, 3.00 eq) was added to a solution of (1H-imidazo[4,5-f][1,10]phenanthrolin-2-yl)methyl acetate (0.350 g, 1.19 mmol, 1.00 eq) in methanol (11.9 mL) and was stirred at rt until thin layer chromatography showed completion of the reaction. 1M HCl solution was added to neutralise the reaction mixture to pH 7 and remove solvent under vacuum to obtain peach-coloured precipitate of (1H-imidazo[4,5-f][1,10]phenanthrolin-2-yl)methanol (44.7 mg, 15.0%); $R_f$ 0.26 [$SiO_2$, DCM/MeOH /$NH_4OH$ 75:23:2]; $^1$H-NMR (400MHz, DMSO-d$^6$): δ 13.92 (s, 1H), 5.88 (t, $^3J_{HH}$ = 4.8 Hz, 1H), 4.86 (d, $^3J_{HH}$ = 5.2 Hz, 2H); ESI-MS *m/z* $[M+H]^+$ 251. Unsuccessful in purifying product but proton resonances were identifiable. Please find Supplementary data for raw $^1$H-

NMR spectrum.

### 6.3.4. Hydroxyphenacyl-related Products and Intermediates

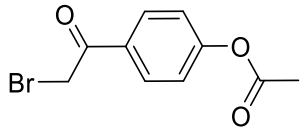
**4-Acetylphenyl acetate**



Procedure from the literature was modified as follows:

To a solution of 4-hydroxyacetophenone (2.00 g, 14.7 mmol, 1.00 eq), triethylamine (306 μL, 22.1 mmol, 1.50 eq) 4-dimethylaminopyridine in DCM, acetic anhydride was added dropwise at 0°C and the mixture was stirred for 1.5 hours at rt. The reaction mixture was poured into water and was extracted with DCM (2 × 20 mL). The organic layer collected was washed further with saturated aqueous ammonia (35 w/v %), then was dried over magnesium sulfate. The reaction mixture was filtered and was dried *in vacuo*. This was purified by flash chromatography ($SiO_2$, DCM) to yield a colourless oil of 4-acetylphenyl acetate (2.13 g, 81.5%); $R_f$ 0.36 [DCM]; $^1$H NMR (400 MHz, $CDCl_3$): δ 7.93 (dp, $^4J_{HH}$ = 8.9 Hz, $^3J_{HH}$ = 2.6 Hz, 2H), 7.13 (dp, $^4J_{HH}$ = 8.8 Hz, $^3J_{HH}$ = 2.6 Hz, 2H), 2.52 (s, 3H), 2.25 (s, 3H); ESI-MS *m/z* $[M+H]^+$ 179.

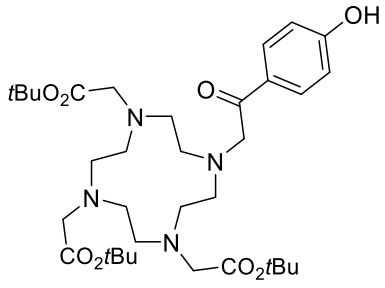
**4-(2-Bromoacetyl)phenyl acetate**



Procedure from the literature was modified as follows:

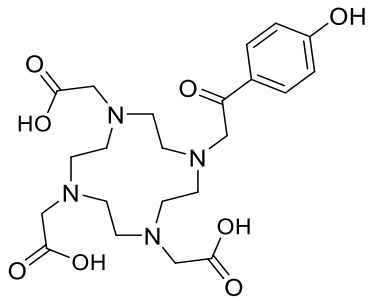
The reaction mixture of 4-acetylphenyl acetate (0.250 g, 1.40 mmol, 1.00 eq) and copper bromide (0.783 g, 3.51 mmol, 2.50 eq) in 1:1 chloroform/ethyl acetate was refluxed at 60°C overnight. The completion of the reaction was shown by disappearance of black solid and cessation of hydrogen bromide formation. Copper(I) bromide was filtered through a bed of celite which was then washed with with ethyl acetate (3 × 15 mL). The solvent was removed from the filtrate by rotary evaporator and was purified by flash chromatography ($SiO_2$, toluene) to yield 4-(2-bromoacetyl)phenyl acetate (0.256 g, 71.1%); $R_f$ 0.42 [toluene]; $^1$H-NMR (400 MHz, $CDCl_3$): δ 8.03 (dp, $^4J_{HH}$ = 8.7 Hz, $^3J_{HH}$ = 1.9 Hz, 2H), 7.23 (dp, $^4J_{HH}$ = 8.8 Hz, $^3J_{HH}$ = 2.0 Hz, 2H), 4.42 (s, 2H), 2.33 (s, 3H); ESI-MS *m/z* $[M+H]^+$ 258.

**1-(4-Hydroxyphenyl)acetyl DO3A-tBu**



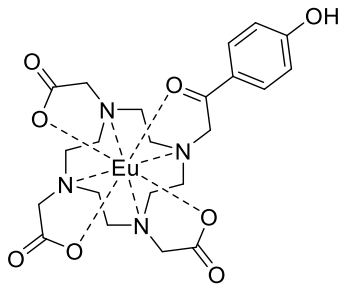

General procedure 3 was followed using 4-(2-bromoacetyl)phenyl acetate (0.250 g, 1.11 mmol, 1.10 eq), DO3A-tBu (0.529 g, 1.01 mmol, 1.00 eq), caesium carbonate (0.783 g, 2.51 mmol, 2.28 eq) and acetonitrile (60 mL) to yield white precipitate of 1-(4-Hydroxyphenyl)acetyl DO3A-tBu (0.557 g, 85.0%); $^1$H-NMR (400 MHz, $CDCl_3$): δ 7.74 (d, *J* = 8.8 Hz, 2H), 6.82 (d, *J* = 8.9 Hz, 2H), 3.83 (t, $^3J_{HH}$ = 5.5 Hz, 2H), 3.63 (t, $^3J_{HH}$ = 6.2 Hz, 2H), 3.36 (s, 2H), 3.28 (s, 2H), 3.16 (s, 2H), 3.06 (t, $^3J_{HH}$ = 5.4 Hz, 2H), 2.94 (t, $^3J_{HH}$ = 6.1 Hz, 2H), 2.76 (s, 5H), 2.66 (s, 1H), 1.47-1.39 (m, 27H); ESI-MS *m/z* $[M+H]^+$ 649.

**1-(4-Hydroxyphenyl)acetyl DO3A (L3.DO3A)**




General procedure 2 was followed using 1-(4-Hydroxyphenyl)acetyl DO3A-tBu (0.360 g, 0.521 mmol, 1.00 eq), TFA (3.19 mL, 41.7 mmol, 80.0 eq), DCM (3.19 mL). This was purified by HPLC (separation method explained in Chapter 6.1.7). Two isomers were found in HPLC, Isomer 1 (25.8 mg, 10.3%, $t_r$ 1.24 min) and Isomer 2 (36.1 mg, 14.0%, $t_r$ 4.03 min); $^1$H NMR (400 MHz, $D_2O$) δ Isomer 1: 7.91 (d, $^3J_{HH}$ = 8.6 Hz, 2H), 7.03 (d, $^3J_{HH}$ = 8.6 Hz, 2H), 4.09 (s, 4H), 3.87 (s, 2H), 3.78 – 3.76 (m, 4H), 3.69 (m, 3H), 3.53 – 3.47 (m, 6H), 3.34 – 3.31 (m, 5H): δ Isomer 2: 7.91 (d, $^3J_{HH}$ = 8.6 Hz, 2H), 7.02z (d, $^3J_{HH}$ = 8.6 Hz, 2H), 4.08 (s, 4H), 3.86 (s, 2H), 3.78 – 3.75 (m, 4H), 3.69 (m, 3H), 3.53 – 3.47 (m, 6H), 3.33 – 3.32 (m, 5H); ESI-MS *m/z* Isomer 1: $[M+H]^+$ 481, Isomer 2: $[M+H]^+$ 495.

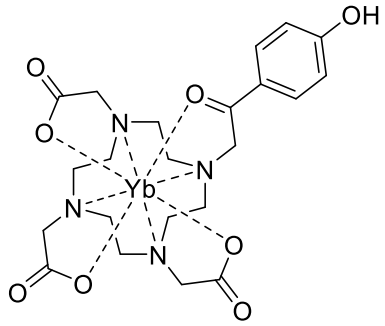
**Eu.1-(4-Hydroxyphenyl)acetyl DO3A (Eu.3)**




General procedure 1 was followed using 1-(4-Hydroxyphenyl)acetyl DO3A (15.0 mg, 31.2 µmol, 1.00 eq), europium triflate (20.6 mg, 34.4 µmol, 1.10 eq), methanol (3.00 mL) and was purified by dialysis to obtain white powder of Eu.1-(4-Hydroxyphenyl)acetyl DO3A (15.7 mg, 80.1%); $^1$H-NMR (400 MHz, $D_2O$): Only peaks outside 0 – 10 ppm are reported:

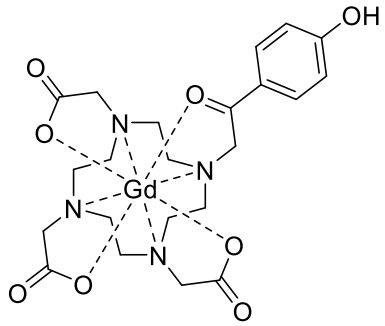
δ Isomer 1: 35.79, 29.39, 28.39, 27.44, -1.83, -3.80, -4.63, -7.52, -8.99, -9.76, -10.00, -11.65, -12.93, -13.45, -13.87, -14.90, -16.06, -17.73, δ Isomer 2: $^{1}$H NMR (400 MHz, $D_2O$) δ 23.98, 21.26, 14.22, 10.38, 1.28, -1.41, -1.68, -2.47, -4.00, -4.66, -5.33, -7.84, -9.14, -9.99, -11.40, -12.75, -13.01, -14.43, -14.68, -17.09, -20.06; ESI-MS m/z Isomer 1: [M+H]+ 630, Isomer 2: [M+H]+ 644.

**Yb.1-(4-Hydroxyphenyl)acetyl DO3A (Yb.3)**




General procedure 1 was followed using 1-(4-Hydroxyphenyl)acetyl DO3A (15.0 mg, 31.2 μmol, 1.00 eq), ytterbium triflate (21.3 mg, 34.4 μmol, 1.10 eq), methanol (3.00 mL) and was purified by dialysis to obtain white powder of Yb.1-(4-Hydroxyphenyl)acetyl DO3A (15.8 g, 78.0%); $^{1}$H-NMR (400 MHz, $D_2O$): Only peaks outside 0 – 10 ppm are reported: $^{1}$H-NMR (400 MHz, $D_2O$) δ Isomer 1: 137.43, 119.43, 116.44, 110.94, 38.57, 30.50, 20.71, 17.88, 17.07, 17.00, 15.23, 13.82, -12.78, -20.68, -29.23, -30.18, -351.21, -38.95, -42.45, -45.54, -52.07, -62.01, -71.16, -71.61, -74.59, δ Isomer 2: 125.97, 114.84, 82.62, 60.73, 41.33, 32.84, -5.48, -9.28, -47.71, -50.72, -55.85, -67.22, -72.77, -95.79, -125.01; ESI-MS *m/z* Isomer 1: $[M+H]^+$ 651, Isomer 2: $[M+H]^+$ 665. Please find more information in the Supplementary data

**Gd.1-(4-Hydroxyphenyl)acetyl DO3A (Gd.3)**




General procedure 1 was followed using 1-(4-Hydroxyphenyl)acetyl DO3A (15 mg, 31.2 μmol, 1.00 eq), gadolinium triflate (20.8 mg, 34.4 μmol, 1.10 eq), methanol (3.00 mL) and was purified by dialysis to obtain white powder of Gd.1-(4-Hydroxyphenyl)acetyl DO3A (14.8 mg, 75.0%); ESI-MS *m/z* $[M+H]^+$ 636

# References


1. J.-C. G. Bünzli and C. Piguet, *Chem. Soc. Rev.*, 2005, **34**.
2. A. de Bettencourt-Dias, in *Luminescence of Lanthanide Ions in Coordination Compounds and Nanomaterials*, 2014, DOI: 10.1002/9781118682760.ch01, pp. 1-48.
3. D. Parker, E. A. Suturina, I. Kuprov and N. F. Chilton, *Acc. Chem. Res*, 2020, **53**, 1520-1534.
4. V. R. Sastri, J. Perumareddi, V. R. Rao, G. Rayudu and J.-C. Bunzli, *Modern aspects of rare earths and their complexes*, Elsevier, 2003.
5. J. Huheey, E. Keiter and R. Keiter, *Journal*, 1993.
6. J. C. G. Bunzli, *Accounts of Chemical Research*, 2006, **39**, 53-61.
7. C. H. Evans, *Episodes from the history of the rare earth elements*, Springer Science & Business Media, 2012.
8. K. Thomas, S. Singh and G. Dieke, *The Journal of Chemical Physics*, 1963, **38**, 2180-2190.
9. G. Choppin and J. Bünzli, *CG Bunzli GR Choppin Elsevier Amsterdam*, 1989, **219**.
10. G. H. Dieke and B. Pandey, *The Journal of Chemical Physics*, 1964, **41**, 1952-1969.
11. N. J. Turro, V. Ramamurthy and J. C. Scaiano, *Modern molecular photochemistry of organic molecules*, Viva Books University Science Books, Sausalito, 2010.
12. B. G. Wybourne, *Molecular Physics*, 2003, **101**, 899-901.
13. X. Z. J. D. Routledge, M. Connolly, M. Tropiano, O. A. Blackburn, A. M. Kenwright, P. D. Beer, S. Aldridge, S. Faulkner, *Angewandte Chemie (International ed. in*

*English)*, 2017, **56**, 7783-7786.

14. M. C. Heffern, L. M. Matosziuk and T. J. Meade, *Chem. Rev.*, 2014, **114**, 4496-4539.

15. C. M. Rudzinski, D. S. Engebretson, W. K. Hartmann and D. G. Nocera, *Journal of Physical Chemistry A*, 1998, **102**, 7442-7446.

16. G. A. Hebbink, S. I. Klink, L. Grave, P. Alink and F. van Veggel, *Chemphyschem*, 2002, **3**, 1014-1018.

17. M. K. Nah, H. G. Cho, H. J. Kwon, Y. J. Kim, C. Park, H. K. Kim and J. G. Kang, *Journal of Physical Chemistry A*, 2006, **110**, 10371-10374.

18. J. R. G. Thorne, J. M. Rey, R. G. Denning, S. E. Watkins, M. Etchells, M. Green and V. Christou, *Journal of Physical Chemistry A*, 2002, **106**, 4014-4021.

19. M. H. Ha-Thi, J. A. Delaire, V. Michelet and I. Leray, *Journal of Physical Chemistry A*, 2010, **114**, 3264-3269.

20. J. B. Lamture, Z. H. Zhou, A. S. Kumar and T. G. Wensel, *Inorganic Chemistry*, 1995, **34**, 864-869.

21. J. Lehr, P. D. Beer, S. Faulkner and J. J. Davis, *Chemical Communications*, 2014, **50**, 5678-5687.

22. S. A. Cotton, *Lanthanide and actinide chemistry*, Wiley, Chichester, 2006.

23. T. Forster, *Annalen Der Physik*, 1948, **2**, 55-75.

24. S. C. V. Balzani, *Top. Curr. Chem.*, 2007, **280**, 1-273.

25. D. L. Dexter, *The Journal of Chemical Physics*, 1953, **21**, 836-850.

26. C. Reinhard, R. Valiente and H. U. Gudel, *Journal of Physical Chemistry B*, 2002, **106**, 10051-10057.

27. S. J. A. Pope, B. P. Burton-Pye, R. Berridge, T. Khan, P. J. Skabara and S. Faulkner, *Dalton Transactions*, 2006, DOI: 10.1039/b600598e, 2907-2912.

28. P. Yuster and S. Weissman, *The Journal of Chemical Physics*, 1949, **17**, 1182-1188.

29. L. Ozawa and M. Itoh, *Chem. Rev.*, 2003, **103**, 3835-3856.

30. S. Shinoya and W. M. Yen, *CRC, Boca Raton*, 1999.

31. R. C. Evans, P. Douglas and C. J. Winscom, *Coordination chemistry reviews*, 2006, **250**, 2093-2126.

32. G. Urbain, *Comptes Rendus Hebdomadaires des Seances de L´Academie des Sciences*, 1906, **142**, 205.

33. W. Yen, S. Shionoya and H. Yamamoto, *Boca Raton*, 2007.

34. A. de Bettencourt-Dias, *Dalton Transactions*, 2007, DOI: 10.1039/B702341C, 2229-2241.

35. D. Payne and L. Reekie, 1988.

36. J. Kido and Y. Okamoto, *Chem. Rev.*, 2002, **102**, 2357-2368.

37. J. Geusic, H. Marcos and L. Van Uitert, *Applied Physics Letters*, 1964, **4**, 182-184.

38. E. Terazzi, S. Suarez, S. Torelli, H. Nozary, D. Imbert, O. Mamula, J. P. Rivera, E. Guillet, J. M. Bénech and G. Bernardinelli, *Advanced functional materials*, 2006, **16**, 157-168.

39. K. Matsumoto and J. Yuan, *Metal Ions in Biological Systems*, 2003, **40**, 191-232.

40. S. Faulkner and J. Matthews, *Comprehensive coordination chemistry II*, 2004, **9**, 913-944.

41. S. Faulkner, S. J. Pope and B. P. Burton-Pye, *Applied Spectroscopy Reviews*, 2005,

**40**, 1-31.

42. J. Shen, L. Zhao and G. Han, *Advanced drug delivery reviews*, 2013, **65**, 744-755.

43. B. Song, C. D. Vandevyver, A.-S. Chauvin and J.-C. G. Bünzli, *Organic & Biomolecular Chemistry*, 2008, **6**, 4125-4133.

44. J.-C. G. Bünzli, S. Comby, A.-S. Chauvin and C. D. Vandevyver, *Journal of rare earths*, 2007, **25**, 257-274.

45. B. A. Hess, A. Kedziorski, L. Smentek and D. Bornhop, *The Journal of Physical Chemistry A*, 2008, **112**, 2397-2407.

46. J.-C. G. Bünzli, *Chemistry Letters*, 2009, **38**, 104-109.

47. K. Kumar and M. F. Tweedle, *Pure and applied chemistry*, 1993, **65**, 515-520.

48. S. H. Koenig and R. D. Brown III, *Progress in Nuclear Magnetic Resonance Spectroscopy*, 1990, **22**, 487-567.

49. S. Aime, M. Botta, M. Fasano and E. Terreno, *Chemical Society Reviews*, 1998, **27**, 19-29.

50. A. Dadabhoy, S. Faulkner and P. G. Sammes, *J. Chem. Soc., Perkin Trans. 2*, 2000, DOI: 10.1039/B008179P, 2359-2360.

51. D. Parker, K. Senanayake and J. A. G. Williams, *Chem. Commun.*, 1997, DOI: 10.1039/A704318J, 1777-1778.

52. P. Atkinson, K. S. Findlay, F. Kielar, R. Pal, D. Parker, R. A. Poole, H. Puschmann, S. L. Richardson, P. A. Stenson, A. L. Thompson and J. Yu, *Organic & Biomolecular Chemistry*, 2006, **4**, 1707-1722.

53. A. Beeby, L. M. Bushby, D. Maffeo and J. A. G. Williams, *J. Chem. Soc., Perkin Trans. 2*, 2000, **2**, 1281-1283.

54. A. Juris, V. Balzani, F. Barigelletti, S. Campagna, P. Belser and A. v. von Zelewsky, *Coordination Chemistry Reviews*, 1988, **84**, 85-277.

55. J. W. Verhoeven, *Pure and Applied Chemistry*, 1996, **68**, 2223-2286.

56. S. E. Braslavsky, *Pure and applied chemistry*, 2007, **79**, 293-465.

57. A. de-Bettencourt-Dias, *Luminescence of Lanthanide Ions in Coordination Compounds and Nanomaterials*, 2014, DOI: 10.1002/9781118682760, 1-370.

58. J. Mehra and H. Rechenberg, *The Conceptual Completion and Extensions of Quantum Mechanics 1932-1941. Epilogue: Aspects of the Further Development of Quantum Theory 1942-1999: Subject Index: Volumes 1 to 6*, Springer Science & Business Media, 2001.

59. D. E. Morris and A. de Bettencourt-Dias, *Luminescence of Lanthanide Ions in Coordination Compounds and Nanomaterials*, 2014, 49-75.

60. J. Reuben, *Progress in nuclear magnetic resonance spectroscopy*, 1973, **9**, 3-70.

61. W. D. Horrocks and D. R. Sudnick, *J. Am. Chem. Soc.*, 1979, **101**, 334-340.

62. I. Bertini, P. Turano and A. J. Vila, *Chem. Rev.*, 1993, **93**, 2833-2932.

63. B. Bleaney, *Journal of Magnetic Resonance (1969)*, 1972, **8**, 91-100.

64. B. Bleaney, C. M. Dobson, B. A. Levine, R. B. Martin, R. J. P. Williams and A. V. Xavier, *Journal of the Chemical Society, Chemical Communications*, 1972, DOI: 10.1039/C3972000791B, 791b-793.

65. N. Long and W.-T. Wong, *The chemistry of molecular imaging*, John Wiley & Sons, 2014.

66. E. N. Zapolotsky, Y. Qu and S. P. Babailov, *Journal of Inclusion Phenomena and Macrocyclic Chemistry*, 2022, **102**, 1-33.

67. G. Ofelt, *The journal of chemical physics*, 1962, **37**, 511-520.

68. B. R. Judd, *Physical review*, 1962, **127**, 750.

69. C. K. Jørgensen and B. Judd, *Molecular Physics*, 1964, **8**, 281-290.

70. C. Piguet and C. F. Geraldes, *Handbook on the physics and chemistry of rare earths*, 2003, **33**, 353-463.

71. I. Bertini, C. Luchinat and G. Parigi, *Progress in Nuclear Magnetic Resonance Spectroscopy*, 2002, **40**, 249.

72. J. D. Rinehart and J. R. Long, *Chemical Science*, 2011, **2**, 2078-2085.

73. M. E. Boulon, G. Cucinotta, J. Luzon, C. Degl'Innocenti, M. Perfetti, K. Bernot, G. Calvez, A. Caneschi and R. Sessoli, *Angewandte Chemie International Edition*, 2013, **52**, 350-354.

74. S. Aime, A. Barge, M. Botta, A. S. D. Sousa and D. Parker, *Angewandte Chemie, International Edition*, 1998, **37**, 2673-2675.

75. M. P. Placidi, L. S. Natrajan, D. Sykes, A. M. Kenwright and S. Faulkner, *Helvetica Chimica Acta*, 2009, **92**, 2427-2438.

76. N. Cakić, T. Ž. Verbić, R. M. Jelić, C. Platas-Iglesias and G. Angelovski, *Dalton Transactions*, 2016, **45**, 6555-6565.

77. Silvio Aime, †, Mauro Botta, Mauro Fasano, M. Paula M. Marques, Carlos F. G. C. Geraldes, ‡, a. Dirk Pubanz and André E. Merbach*, *Inorg. Chem.*, 1997, **36**, 2059-2068.

78. K. J. Miller, A. A. Saherwala, B. C. Webber, Y. Wu, A. D. Sherry and M. Woods, *Inorganic chemistry*, 2010, **49**, 8662-8664.

79. S. Aime, M. Botta and G. Ermondi, *Inorg. Chem.*, 1992, **31**, 4291-4299.

80. L. S. Natrajan, N. M. Khoabane, B. L. Dadds, C. A. Muryn, R. G. Pritchard, S. L. Heath, A. M. Kenwright, I. Kuprov and S. Faulkner, *Inorganic chemistry*, 2010, **49**, 7700-7709.

81. S. Aime, A. Barge, J. I. Bruce, M. Botta, J. A. Howard, J. M. Moloney, D. Parker, A. S. De Sousa and M. Woods, *J. Am. Chem. Soc.*, 1999, **121**, 5762-5771.

82. M. Woods, S. Aime, M. Botta, J. A. Howard, J. M. Moloney, M. Navet, D. Parker, M. Port and O. Rousseaux, *J. Am. Chem. Soc.*, 2000, **122**, 9781-9792.

83. P. Caravan, J. J. Ellison, T. J. McMurry and R. B. Lauffer, *Chem. Rev.*, 1999, **99**, 2293-2352.

84. L. M. De Leon-Rodriguez, A. J. M. Lubag, C. R. Malloy, G. V. Martinez, R. J. Gillies and A. D. Sherry, *Accounts of Chemical Research*, 2009, **42**, 948-957.

85. A. E. Merbach and É. Tóth, *The chemistry of contrast agents in medical magnetic resonance imaging*, Wiley, Chichester, 2001.

86. J. E. Jones and S. J. A. Pope, *Dalton Transactions*, 2009, DOI: 10.1039/b913902h, 8421-8425.

87. M. Tropiano, C. J. Record, E. Morris, H. S. Rai, C. m. Allain and S. Faulkner, *Organometallics*, 2012, **31**, 5673-5676.

88. S. Faulkner, L. S. Natrajan, W. S. Perry and D. Sykes, *Dalton Transactions*, 2009, DOI: 10.1039/b902006c, 3890-3899.

89. A. Beeby and S. Faulkner, *Chem. Phys. Lett.*, 1997, **266**, 116-122.

90. A. Beeby, R. S. Dickins, S. Faulkner, D. Parker and J. A. G. Williams, *Chem. Comm.*, 1997, DOI: 10.1039/a702388j, 1401-1402.

91. S. I. Klink, L. Grave, D. N. Reinhoudt, F. C. van Veggel, M. H. Werts, F. A. Geurts

and J. W. Hofstraat, *The Journal of Physical Chemistry A*, 2000, **104**, 5457-5468.

92. G. M. Davies, H. Adams, S. J. Pope, S. Faulkner and M. D. Ward, *Photochemical & Photobiological Sciences*, 2005, **4**, 829-834.

93. M. González-Lorenzo, C. Platas-Iglesias, F. Avecilla, S. Faulkner, S. J. Pope, A. De Blas and T. Rodríguez-Blas, *Inorganic chemistry*, 2005, **44**, 4254-4262.

94. W. D. Horrocks, J. P. Bolender, W. D. Smith and R. M. Supkowski, *J. Am. Chem. Soc.*, 1997, **119**, 5972-5973.

95. A. Beeby, S. Faulkner and J. A. G. Williams, *J. Chem. Soc., Dalton Trans.*, 2002, DOI: 10.1039/B201867P, 1918.

96. W. S. Perry, S. J. A. Pope, C. Allain, B. J. Coe, A. M. Kenwright and S. Faulkner, *Dalton Transactions*, 2010, **39**, 10974-10983.

97. S. Faulkner, B. P. Burton-Pye, T. Khan, L. R. Martin, S. D. Wray and P. J. Skabara, *Chemical Communications*, 2002, DOI: 10.1039/b204218e, 1668-1669.

98. T. Főrster, *Discussions of the Faraday Society*, 1959, **27**, 7-17.

99. F. Barigelletti, L. Flamigni, V. Balzani, J.-P. Collin, J.-P. Sauvage, A. Sour, E. Constable and A. C. Thompson, *Coordination Chemistry Reviews*, 1994, **132**, 209-214.

100. T. Lazarides, D. Sykes, S. Faulkner, A. Barbieri and M. D. Ward, *Chemistry–A European Journal*, 2008, **14**, 9389-9399.

101. T. Lazarides, N. M. Tart, D. Sykes, S. Faulkner, A. Barbieri and M. D. Ward, *Dalton Transactions*, 2009, 3971-3979.

102. M. R. Sambrook, D. Curiel, E. J. Hayes, P. D. Beer, S. J. Pope and S. Faulkner, *New Journal of Chemistry*, 2006, **30**, 1133-1136.

103. F.-F. Chen, Z.-Q. Chen, Z.-Q. Bian and C.-H. Huang, *Coordination Chemistry Reviews*, 2010, **254**, 991-1010.

104. L.-J. Xu, G.-T. Xu and Z.-N. Chen, *Coordination Chemistry Reviews*, 2014, **273-274**, 47-62.

105. N. M. Shavaleev, G. Accorsi, D. Virgili, Z. R. Bell, T. Lazarides, G. Calogero, N. Armaroli and M. D. Ward, *Inorganic Chemistry*, 2005, **44**, 61-72.

106. A. Vlcek, E. S. Dodsworth, W. J. Pietro and A. Lever, *Inorganic Chemistry*, 1995, **34**, 1906-1913.

107. W. Kaim, *Coordination chemistry reviews*, 1987, **76**, 187-235.

108. M. K. De Armond and M. L. Myrick, *Accounts of Chemical Research*, 1989, **22**, 364-370.

109. K. Kalyanasundaram and M. Grätzel, *Coordination chemistry reviews*, 1998, **177**, 347-414.

110. V. Balzani, *Tetrahedron*, 1992, **48**, 10443-10514.

111. M. Marcaccio, F. Paolucci, C. Paradisi, M. Carano, S. Roffia, C. Fontanesi, L. J. Yellowlees, S. Serroni, S. Campagna and V. Balzani, *Journal of Electroanalytical Chemistry*, 2002, **532**, 99-112.

112. V. Balzani, G. Bergamini, F. Marchioni and P. Ceroni, *Coordination Chemistry Reviews*, 2006, **250**, 1254-1266.

113. T. Koullourou, L. S. Natrajan, H. Bhavsar, S. J. A. Pope, J. H. Feng, J. Narvainen, R. Shaw, E. Scales, R. Kauppinen, A. M. Kenwright and S. Faulkner, *J. Am. Chem. Soc.*, 2008, **130**, 2178-+.

114. S. J. A. Pope, B. J. Coe, S. Faulkner, E. V. Bichenkova, X. Yu and K. T. Douglas, *J.*

*Am. Chem. Soc.*, 2004, **126**, 9490-9491.

115. K. Sénéchal-David, S. J. Pope, S. Quinn, S. Faulkner and T. Gunnlaugsson, *Inorganic chemistry*, 2006, **45**, 10040-10042.

116. Z. Kotková, L. Helm, J. Kotek, P. Hermann and I. Lukeš, *Dalton Transactions*, 2012, **41**, 13509-13519.

117. M. Weller, T. Overton, J. Rourke and F. Armstrong, *Inorganic chemistry*, Oxford University Press, USA, 6th edn., 2014.

118. N. J. Long, *Metallocenes : an introduction to sandwich complexes*, Blackwell Science, Oxford, 1998.

119. G. Wilkinson, M. Rosenblum, M. C. Whiting and R. B. Woodward, *J. Am. Chem. Soc.*, 1952, **74**, 2125-2126.

120. A. Haaland, *Accounts of Chemical Research*, 1979, **12**, 415-422.

121. I. Langmuir, *Science*, 1921, **54**, 59-67.

122. W. B. Jensen, *J. Chem. Educ.*, 2005, **82**, 28.

123. A. Togni, *Ferrocenes: homogeneous catalysis, organic synthesis, materials science*, John Wiley & Sons, 2008.

124. L. Lin, A. Berces and H.-B. Kraatz, *Journal of organometallic chemistry*, 1998, **556**, 11-20.

125. S. Barlow and S. R. Marder, *Chemical Communications*, 2000, DOI: 10.1039/B004907G, 1555-1562.

126. J. C. Calabrese, L. T. Cheng, J. C. Green, S. R. Marder and W. Tam, *J. Am. Chem. Soc.*, 1991, **113**, 7227-7232.

127. E. S. Phillips, *Ferrocenes [electronic resource] : compounds, properties and applications*, Nova Science Publishers, New York, 2011.

128. M. M. H. a. G. Mokdsi, *Current Medicinal Chemistry*, 2000, **7**, 1289-1303.

129. P. Köpf-Maier, W. Wagner and H. Köpf, *Cancer Chemotherapy and Pharmacology*, 1981, **5**, 237-241.

130. K. E. Dombrowski, W. Baldwin and J. E. Sheats, *J. Organomet. Chem.*, 1986, **302**, 281-306.

131. P. Kopfmaier, B. Hesse and H. Kopf, *Journal of Cancer Research and Clinical Oncology*, 1980, **96**, 43-51.

132. K. M. Christensen, A. Bakac and J. H. Espenson, *Chem. Phys.*, 1993, **176**, 359-365.

133. C. D. Hall and N. W. Sharpe, *J. Photochem. Photobiol., A*, 1991, **56**, 255-265.

134. Yao-Feng Yuan, Thomas Cardinaels, Kyra Lunstroot, Kristof Van Hecke, Luc Van Meervelt, Christiane Görller-Walrand, a. Koen Binnemans and Peter Nockemann*, *Inorg. Chem.*, 2007, **46**, 5302-5309.

135. M. Tropiano, N. L. Kilah, M. Morten, H. Rahman, J. J. Davis, P. D. Beer and S. Faulkner, 2011, **133**, 11847 - 11849.

136. A. Beeby, S. Faulkner and J. A. G. Williams, 2002, DOI: 10.1039/B201867P, 1918.

137. D. Kovacs, E. Mathieu, S. R. Kiraev, J. A. Wells, E. Demeyere, A. Sipos and K. E. Borbas, *J. Am. Chem. Soc.*, 2020, **142**, 13190-13200.

138. Y. Xu, P. Saweczko and H.-B. Kraatz, *Journal of Organometallic Chemistry*, 2001, **637**, 335-342.

139. S. R. Kiraev, E. Mathieu, F. Siemens, D. Kovacs, E. Demeyere and K. E. Borbas, *Molecules*, 2020, **25**, 5282.

140. P. D. Beer, A. R. Graydon, A. O. Johnson and D. K. Smith, *Inorganic chemistry*, 1997, **36**, 2112-2118.

141. P. D. Beer, D. B. Crowe, M. I. Ogden, M. G. B. Drew and B. Main, *Journal of the Chemical Society, Dalton Transactions*, 1993, DOI: 10.1039/DT9930002107, 2107-2116.

142. E. PMC, *Res. Commun. Mol. Pathol. Pharmacol.*, 1980, **27**, 139.

143. D. J. Beck and R. R. Brubaker, *J. Bacteriol.*, 1973, **116**, 1247-1252.

144. H. N. A. Fraval, C. J. Rawlings and J. J. Roberts, *Mutation Research/Fundamental and Molecular Mechanisms of Mutagenesis*, 1978, **51**, 121-132.

145. H. K. P. Köpf-Maier, *Zeitschrift für Naturforschung B*, 2018, **34**, 805-807.

146. M. Kartalou and J. M. Essigmann, *Mutation Research/Fundamental and Molecular Mechanisms of Mutagenesis*, 2001, **478**, 1-21.

147. K. Woźniak and J. Błasiak, *Acta Biochimica Polonica*, 2002, **49**, 583-596.

148. W. W. P. Köpf-Maier, H. Köpf, *Cancer Chemotheraphy and Pharmacology*, 1981, **5**, 237-241.

149. H. S. G. Lümmen, H. Luboldt, T. Otto, H. Rübben, *Cancer Chemotheraphy and Pharmacology*, 1998, **42**, 415-417.

150. T. J. M. J. H. Toney *J. Am. Chem. Soc.*, 1985, **107**, 947-953.

151. O. R. Allen, R. J. Knox and P. C. McGowan, *J. Chem. Soc., Dalton Trans.*, 2008, DOI: 10.1039/B812244J, 9293-9295.

152. S. Faulkner and B. P. Burton-Pye, *Chemical Communications*, 2005, DOI:

10.1039/b412329h, 259-261.

153. A. Beeby, I. M. Clarkson, R. S. Dickins, S. Faulkner, D. Parker, L. Royle, A. S. de Sousa, J. A. G. Williams and M. Woods, *Journal of the Chemical Society-Perkin Transactions 2*, 1999, DOI: 10.1039/a808692c, 493-503.

154. R. G. Franz, *AAPS PharmSci*, 2001, **3**, 1.

155. L. R. Hill, T. J. Sorensen, O. A. Blackburn, A. Brown, P. D. Beer and S. Faulkner, *Dalton Transactions*, 2013, **42**, 67-70.

156. T. J. Sorensen, L. R. Hill and S. Faulkner, *Chemistryopen*, 2015, **4**, 509-515.

157. C. M. Fisher, E. Fuller, B. P. Burke, V. Mogilireddy, S. J. Pope, A. E. Sparke, I. Déchamps-Olivier, C. Cadiou, F. Chuburu and S. Faulkner, *Dalton Transactions*, 2014, **43**, 9567-9578.

158. A. E. Sparke, C. M. Fisher, R. E. Mewis and S. J. Archibald, *Tetrahedron Lett.*, 2010, **51**, 4723-4726.

159. E. A. Lewis, R. W. Boyle and S. J. Archibald, *Chemical communications*, 2004, 2212-2213.

160. C. Piguet and J.-C. G. Bünzli, *Chemical Society Reviews*, 1999, **28**, 347-358.

161. J.-F. Lemonnier, L. Guénée, C. Beuchat, T. A. Wesolowski, P. Mukherjee, D. H. Waldeck, K. A. Gogick, S. Petoud and C. Piguet, *J. Am. Chem. Soc.*, 2011, **133**, 16219-16234.

162. Simon J. A. Pope, Benjamin J. Coe, †, Stephen Faulkner, †, Elena V. Bichenkova, a. Xuan Yu and K. T. Douglas‡, *J. Am. Chem. Soc.*, 2004, **126**, 9490-9491.

163. T. J. Sorensen and S. Faulkner, *Accounts of Chemical Research*, 2018, **51**, 2493-2501.

164. M. Tropiano, Thesis (D.Phil.), University of Oxford, 2013.

165. M. Jauregui, W. S. Perry, C. Allain, L. R. Vidler, M. C. Willis, A. M. Kenwright, J. S. Snaith, G. J. Stasiuk, M. P. Lowe and S. Faulkner, *Dalton transactions*, 2009, 6283-6285.

166. A. Beeby, R. S. Dickins, S. FitzGerald, L. J. Govenlock, C. L. Maupin, D. Parker, J. P. Riehl, G. Siligardi and J. A. G. Williams, *Chem. Comm.*, 2000, DOI: 10.1039/b002452j, 1183-1184.

167. S. I. Klink, H. Keizer and F. van Veggel, *Angewandte Chemie-International Edition*, 2000, **39**, 4319-+.

168. N. M. Shavaleev, L. P. Moorcraft, S. J. A. Pope, Z. R. Bell, S. Faulkner and M. D. Ward, *Chemical Communications*, 2003, DOI: 10.1039/b301878d, 1134-1135.

169. N. M. Shavaleev, L. P. Moorcraft, S. J. A. Pope, Z. R. Bell, S. Faulkner and M. D. Ward, *Chemistry-a European Journal*, 2003, **9**, 5283-5291.

170. M. Polášek, J. Kotek, P. Hermann, I. Císařová, K. Binnemans and I. Lukeš, *Inorg. Chem.*, 2008, **48**, 466-475.

171. E. McCafferty, *Introduction to corrosion science*, Springer Science & Business Media, 2010.

172. R. Torres, A. Arnau and H. Perrot, *Revista EIA*, 2006, 9-21.

173. H. Varela, M. Malta and R. M. Torresi, *Química Nova*, 2000, **23**, 664-679.

174. K. J. Lee, N. Elgrishi, B. Kandemir and J. L. Dempsey, *Nature Reviews Chemistry*, 2017, **1**, 1-14.

175. P. T. Kissinger and W. R. Heineman, *J. Chem. Educ.*, 1983, **60**, 702.

176. J. J. Van Benschoten, J. Y. Lewis, W. R. Heineman, D. A. Roston and P. T. Kissinger, *J. Chem. Educ.*, 1983, **60**, 772.

177. J.-M. Savéant, *Elements of molecular and biomolecular electrochemistry: an electrochemical approach to electron transfer chemistry*, John Wiley & Sons, 2006.

178. N. Elgrishi, K. J. Rountree, B. D. McCarthy, E. S. Rountree, T. T. Eisenhart and J. L. Dempsey, *J. Chem. Educ.*, 2018, **95**, 197-206.

179. C. Swearingen, J. Wu, J. Stucki and A. Fitch, *Environmental Science & Technology*, 2004, **38**, 5598-5603.

180. R. S. Dickins, S. Aime, A. S. Batsanov, A. Beeby, M. Botta, J. Bruce, J. A. K. Howard, C. S. Love, D. Parker, R. D. Peacock and H. Puschmann, *J. Am. Chem. Soc.*, 2002, **124**, 12697-12705.

181. T. Kimura and G. R. Choppin, *Journal of Alloys and Compounds*, 1994, **213**, 313-317.

182. M. H. V. Werts, J. W. Hofstraat, F. A. J. Geurts and J. W. Verhoeven, *Chemical Physics Letters*, 1997, **276**, 196-201.

183. A. Beeby and S. Faulkner, *Chemical Physics Letters*, 1997, **266**, 116-122.

184. A. Beeby, R. S. Dickins, S. Faulkner, D. Parker and J. A. G. Williams, *Chemical Communications*, 1997, DOI: 10.1039/a702388j, 1401-1402.

185. M. H. V. Werts, R. H. Woudenberg, P. G. Emmerink, R. van Gassel, J. W. Hofstraat and J. W. Verhoeven, *Angewandte Chemie-International Edition*, 2000, **39**, 4542-+.

186. D. Imbert, M. Cantuel, J. C. G. Bunzli, G. Bernardinelli and C. Piguet, *J. Am. Chem. Soc.*, 2003, **125**, 15698-15699.

187. S. Campagna, F. Puntoriero, F. Nastasi, G. Bergamini and V. Balzani, *Top. Curr. Chem.*, 2007, **280**, 117-214.

188. W. Wu, S. Ji, W. Wu, J. Shao, H. Guo, T. D. James and J. Zhao, *Chemistry–A*

*European Journal*, 2012, **18**, 4953-4964.

189. C. Alexander, N. Prajith, P. Priyanka, A. Nithyakumar and N. Arockia Samy, *JBIC Journal of Biological Inorganic Chemistry*, 2019, **24**, 405-418.

190. A. I. Jothi and V. Alexander, *Crystengcomm*, 2017, **19**, 5251-5258.

191. Z. X. Wang and H. L. Qin, *Journal of Heterocyclic Chemistry*, 2005, **42**, 1001-1005.

192. D. Coman, G. E. Kiefer, D. L. Rothman, A. D. Sherry and F. Hyder, *NMR in Biomedicine*, 2011, **24**, 1216-1225.

193. C. C. Hinckley, *J. Am. Chem. Soc.*, 1969, **91**, 5160-5162.

194. A. C. Harnden, D. Parker and N. J. Rogers, *Coordination Chemistry Reviews*, 2019, **383**, 30-42.

195. S. F. Mason, R. D. Peacock and B. Stewart, *Chemical Physics Letters*, 1974, **29**, 149-153.

196. P. Harvey, A. M. Blamire, J. I. Wilson, K.-L. N. A. Finney, A. M. Funk, P. K. Senanayake and D. Parker, *Chemical Science*, 2013, **4**, 4251-4258.

197. A. Krężel and W. Bal, *Journal of inorganic biochemistry*, 2004, **98**, 161-166.

198. E. PMC, *Res. Commun. Mol. Pathol. Pharmacol.*, 1980, **27**, 139.

199. J. Leonard, B. Lygo and G. Procter, *Advanced practical organic chemistry*, CRC press, 3 edn., 2013.

200. P. K. Glasoe and F. Long, *The Journal of Physical Chemistry*, 1960, **64**, 188-190.

201. A. Dadabhoy, S. Faulkner and P. G. Sammes, *Journal of the Chemical Society, Perkin Transactions 2*, 2002, 348-357.

202. W. J. Kruper, P. R. Rudolf and C. A. Langhoff, *J. Org. Chem.*, 1993, **58**, 3869-3876.

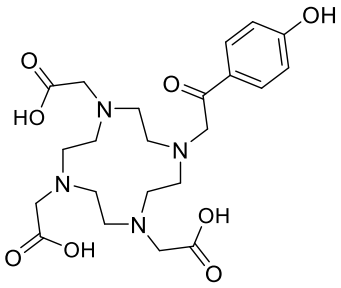
203. A. P. Ferreira, J. o. L. F. da Silva, M. T. Duarte, M. F. M. da Piedade, M. P. Robalo, S. G. Harjivan, C. Marzano, V. Gandin and M. M. Marques, *Organometallics*, 2009, **28**, 5412-5423.

204. L. C. King and G. K. Ostrum, *J. Org. Chem.*, 1964, **29**, 3459-3461.

205. V. K. Tandon and M. Kumar, *Tetrahedron Lett.*, 2004, **45**, 4185-4187.

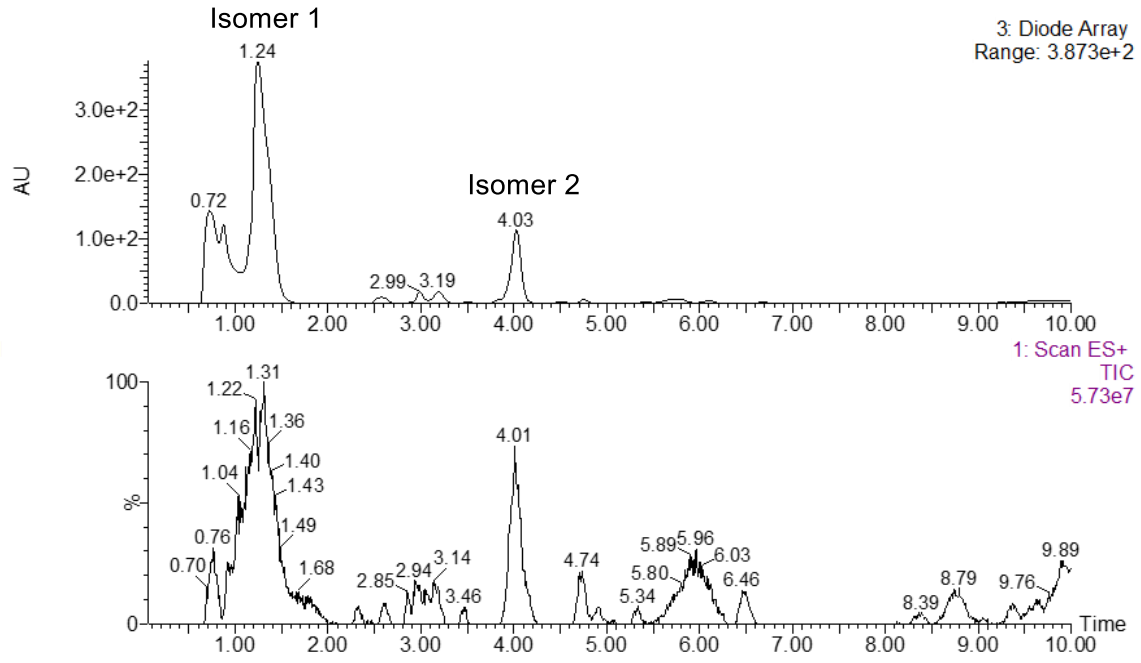
# Supplementary Data

### 1-(4-Hydroxyphenyl)acetyl DO3A

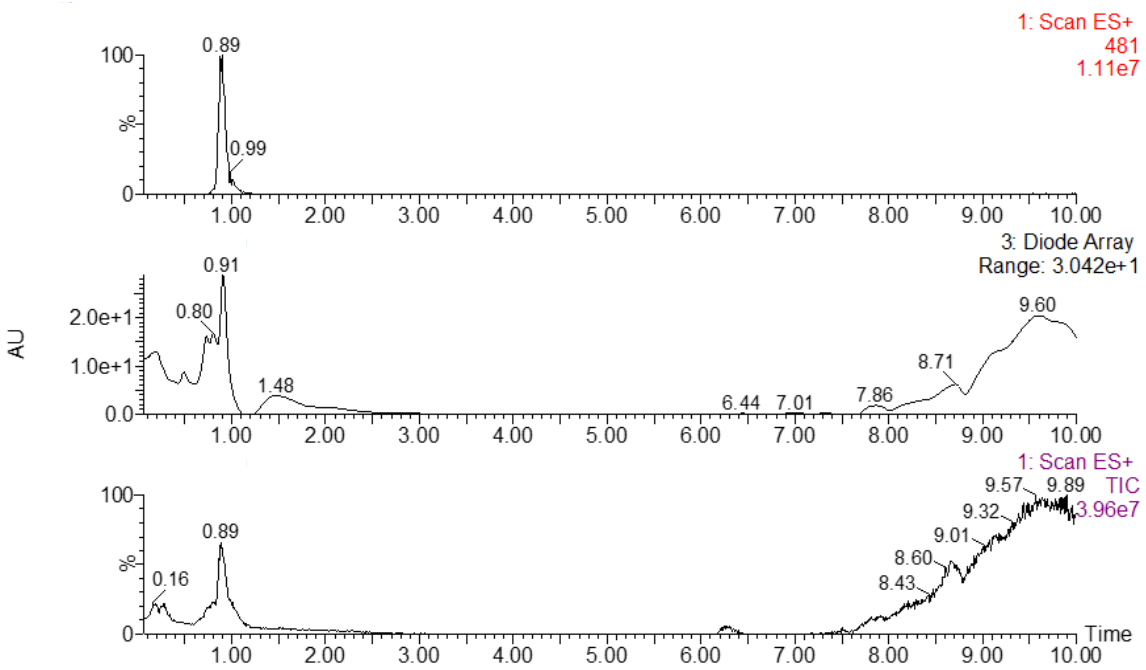


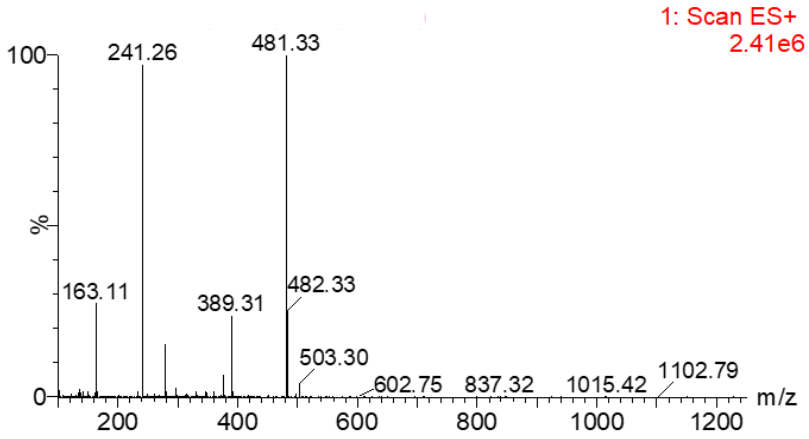

HPLC

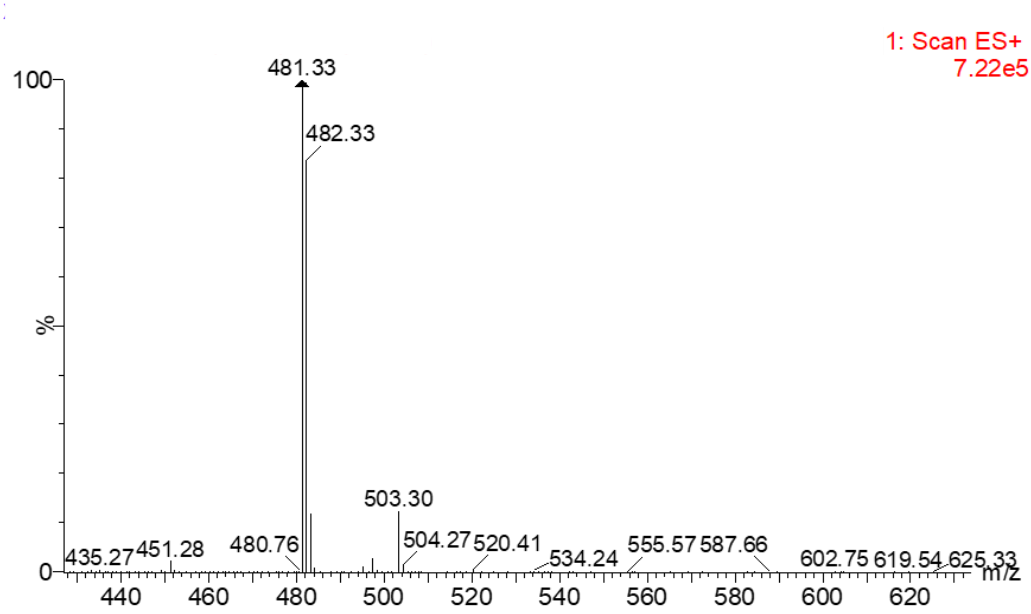
Analytical HPLC data before purification:



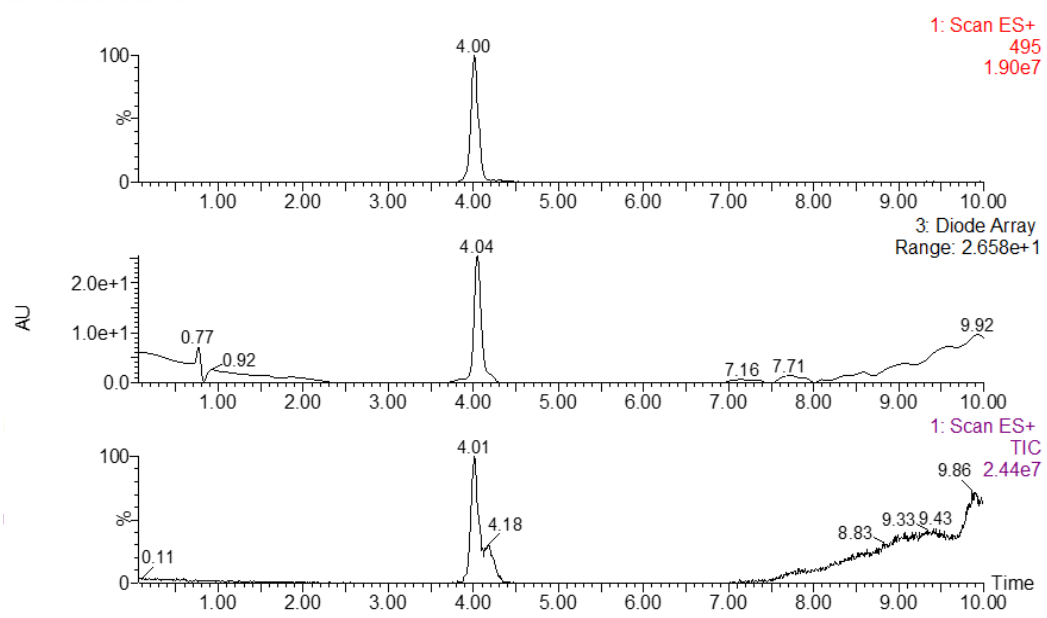

Analytical HPLC data of purified Isomer 1:

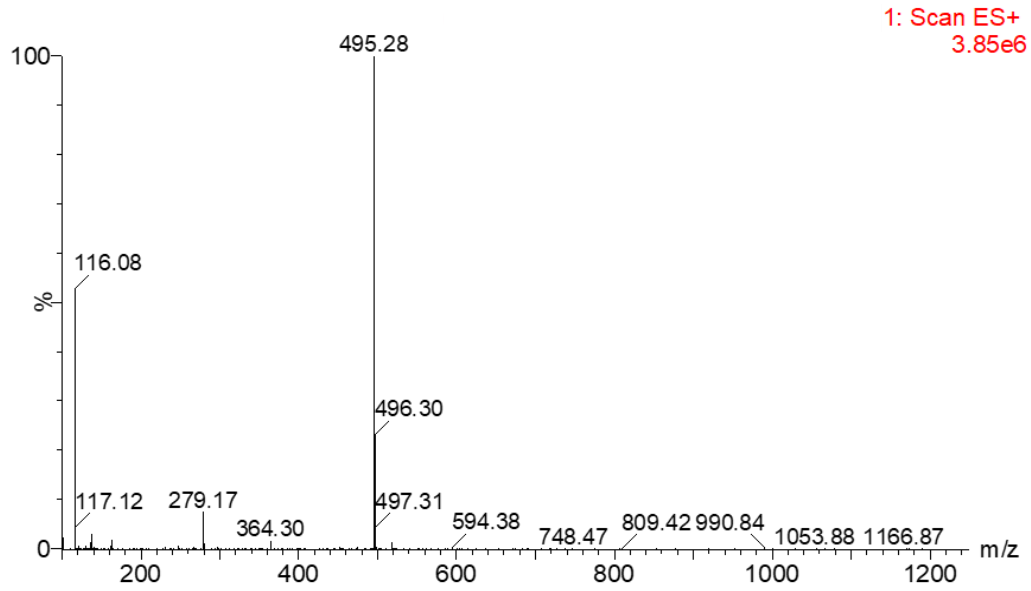

1: Scan ES+
481
1.11e7
0.89
0.99
3: Diode Array
Range: 3.042e+1
AU
0.91
0.80
1.48
6.44
7.01
7.86
8.71
9.60
1: Scan ES+
TIC
3.96e7
9.57
9.89
9.32
9.01
8.60
8.43
0.16
Time


1: Scan ES+
2.41e6
241.26
481.33
163.11
389.31
482.33
503.30
602.75
837.32
1015.42
1102.79
m/z

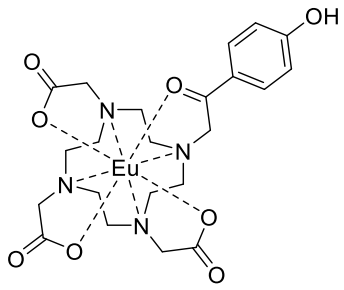



Analytical HPLC data of purified Isomer 2:

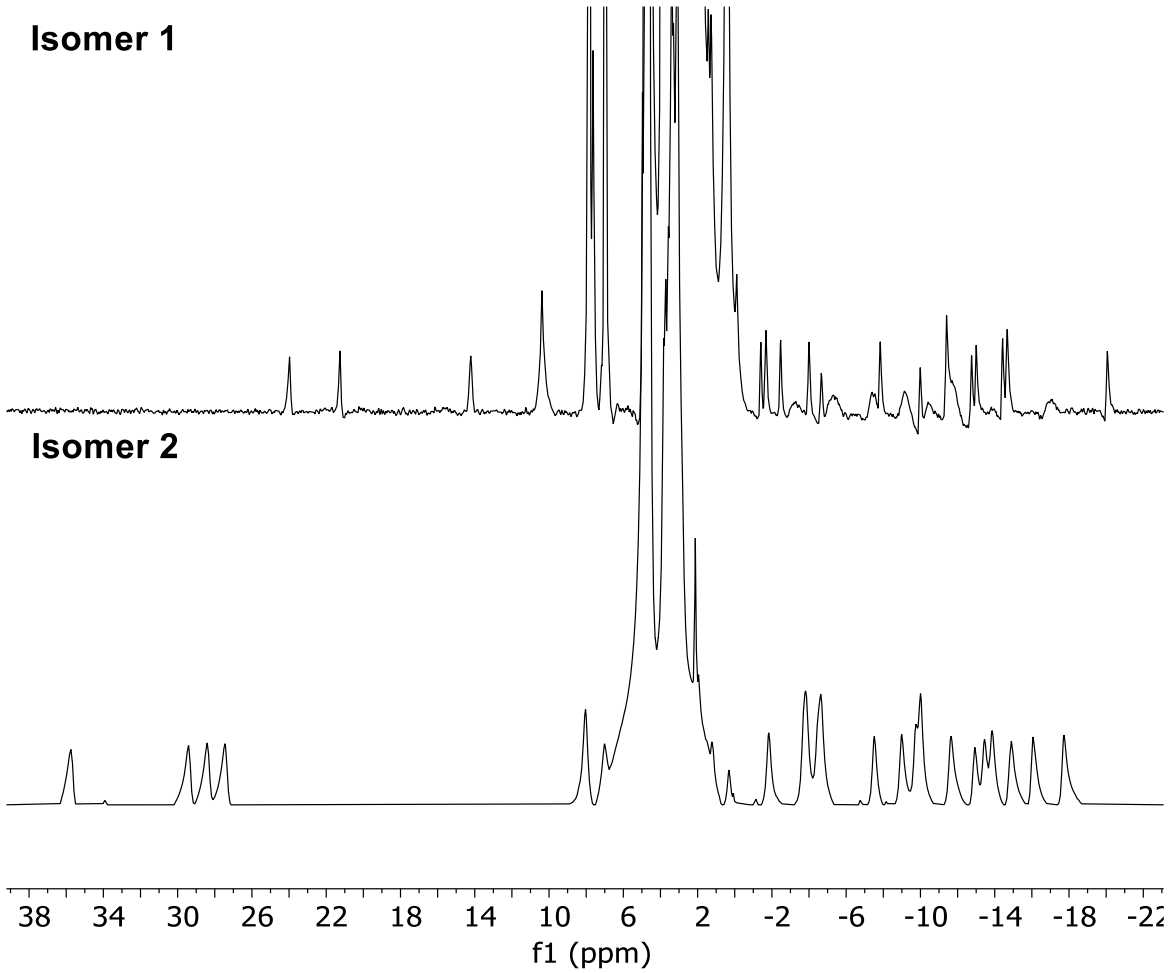





**Eu.1-(4-Hydroxyphenyl)acetyl DO3A (Eu.3)**



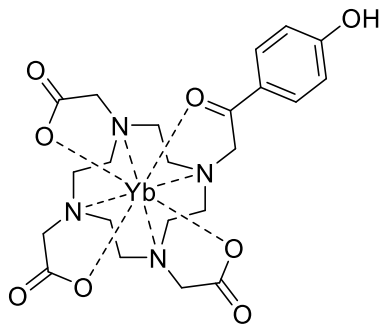

$^{1}$H-NMR



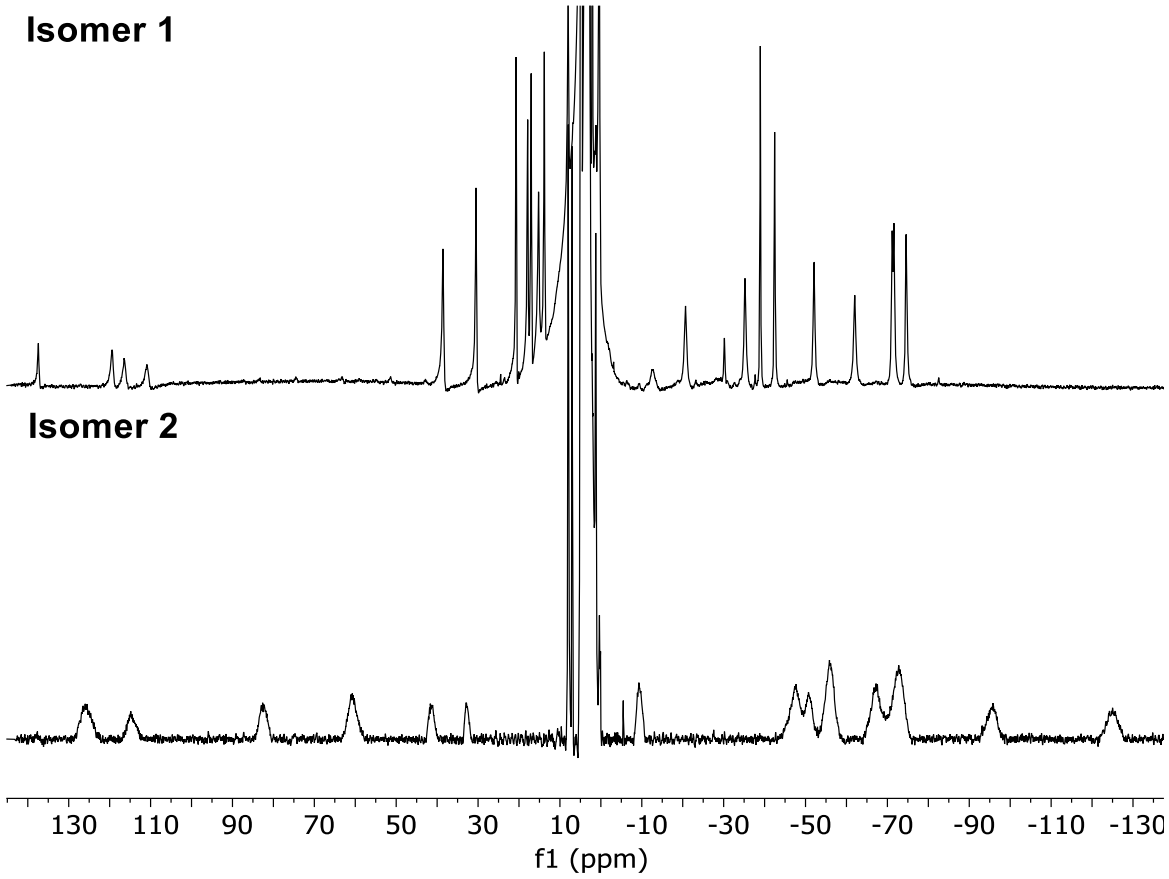

it is clear that, while the europium complex exists predominantly as SAP isomers, the ytterbium complex is a mixture of SAP and TSAP forms. This is likely to be a consequence of the lanthanide contraction, with the smaller ytterbium centre giving rise to higher steric interactions in the ternary complex (and interfering significant coordination of water or carboxylate at the axial coordination site).

Isomer 1 predominantly exists as TSAP isomers with chemical shift for axial azamacrocyclic ring protons at 10-26 ppm. Isomer 2 predominantly exists as SAP isomer with chemical shift for axial azamacrocyclic ring protons at 26-38 ppm.

**Yb.1-(4-Hydroxyphenyl)acetyl DO3A (Yb.3)**

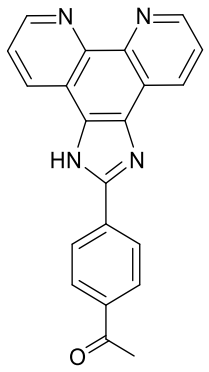



$^{1}$H-NMR

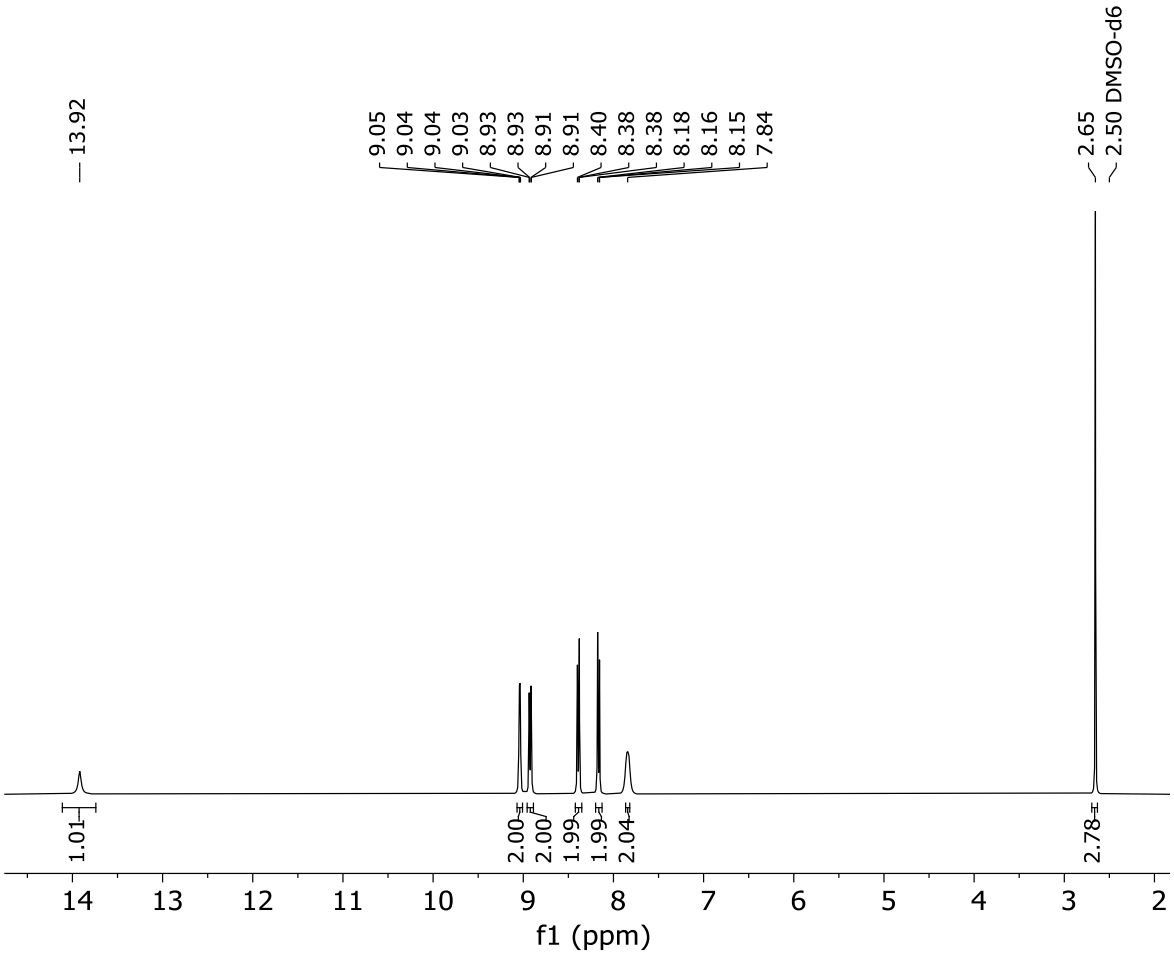



Isomer 1 predominantly exists as SAP isomers with chemical shifts for axial azamacrocyclic ring protons at 100-140 ppm. Isomer 2 exists as a mixture of TSAP and SAP isomers with chemical shifts for axial azamacrocyclic ring protons at 30-130 ppm. Broadened peaks for Isomer 2 show a slow exchange of TSAP and SAP isomers in NMR timescale.

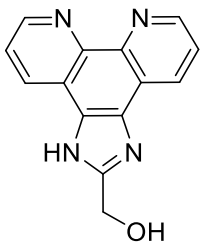
**1-(4-(1H-Imidazo[4,5-f][1,10]phenanthrolin-2-yl)phenyl)ethan-1-one**




$^{1}$H-NMR

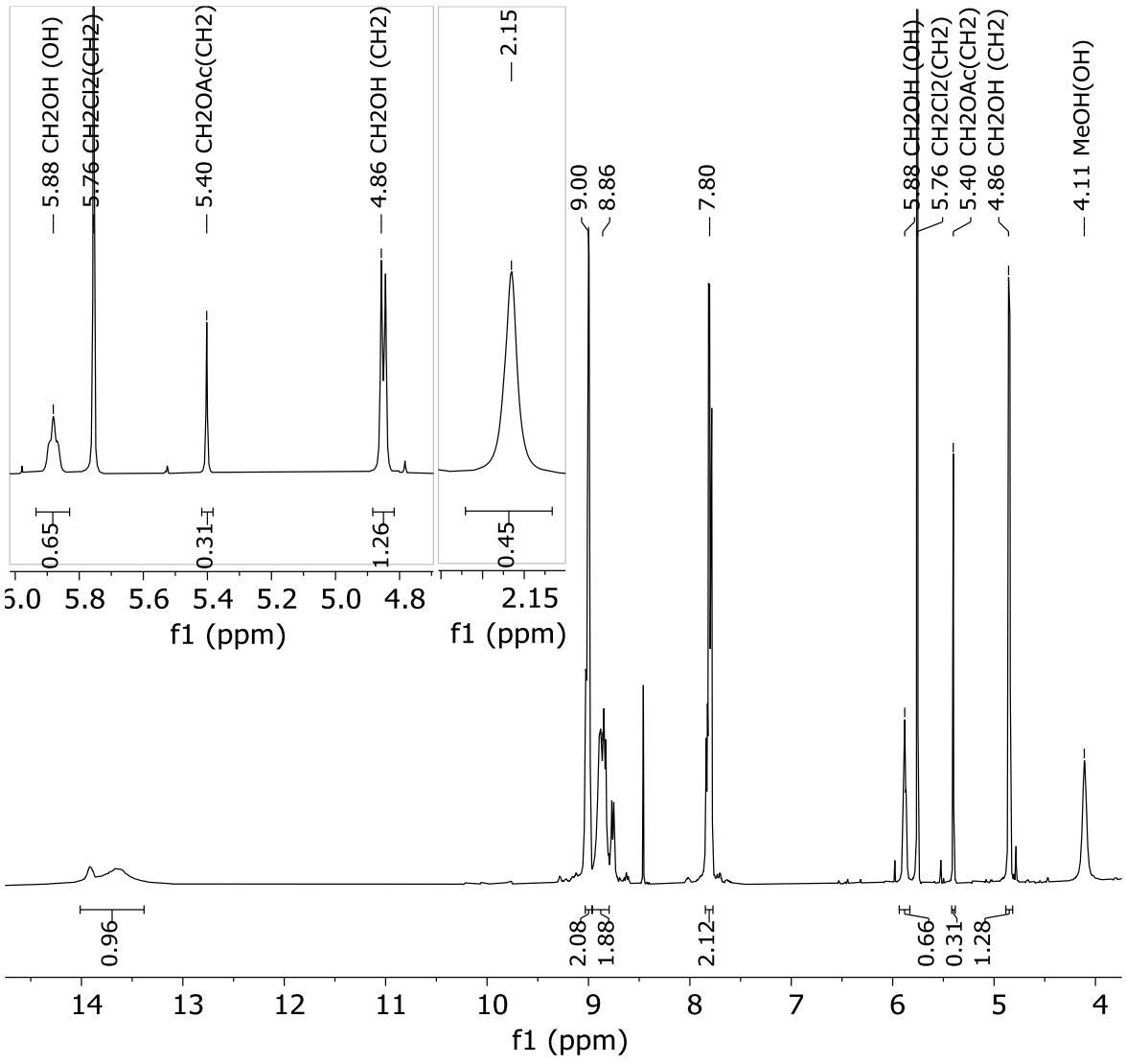


**(1H-Imidazo[4,5-f][1,10]phenanthrolin-2-yl)methanol**



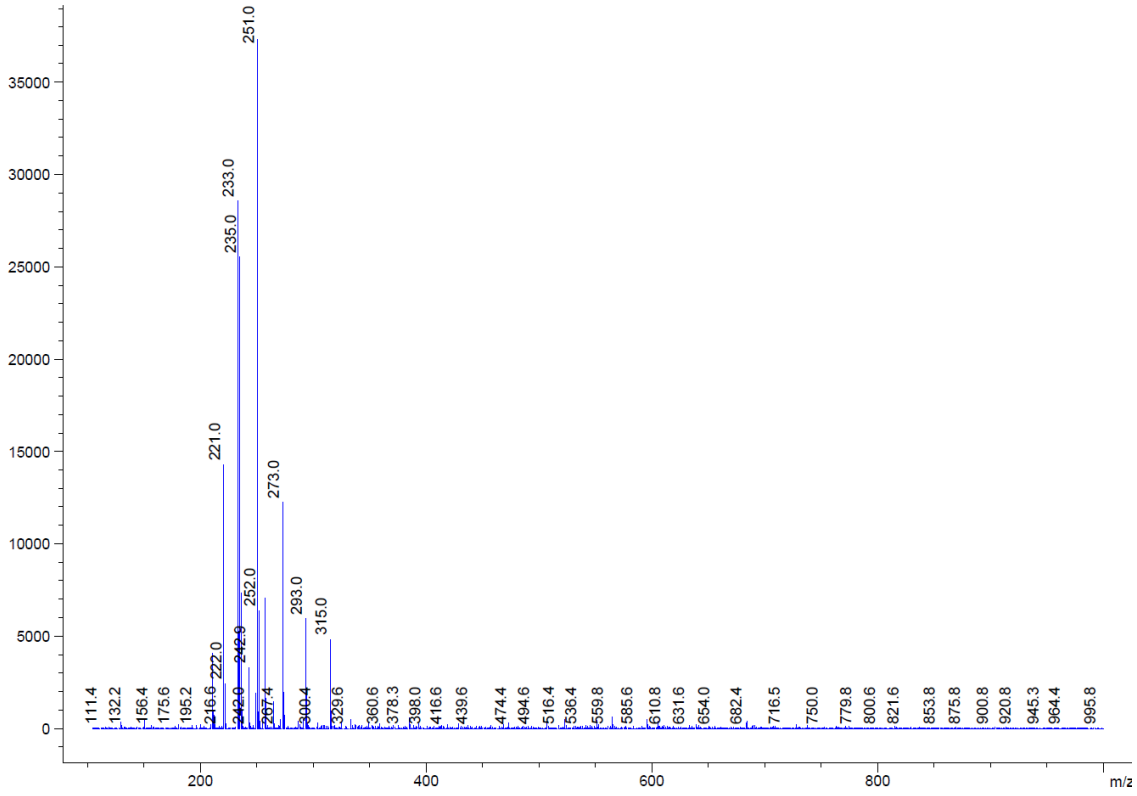

$^{1}$H-NMR

Shows mixture of isomers.

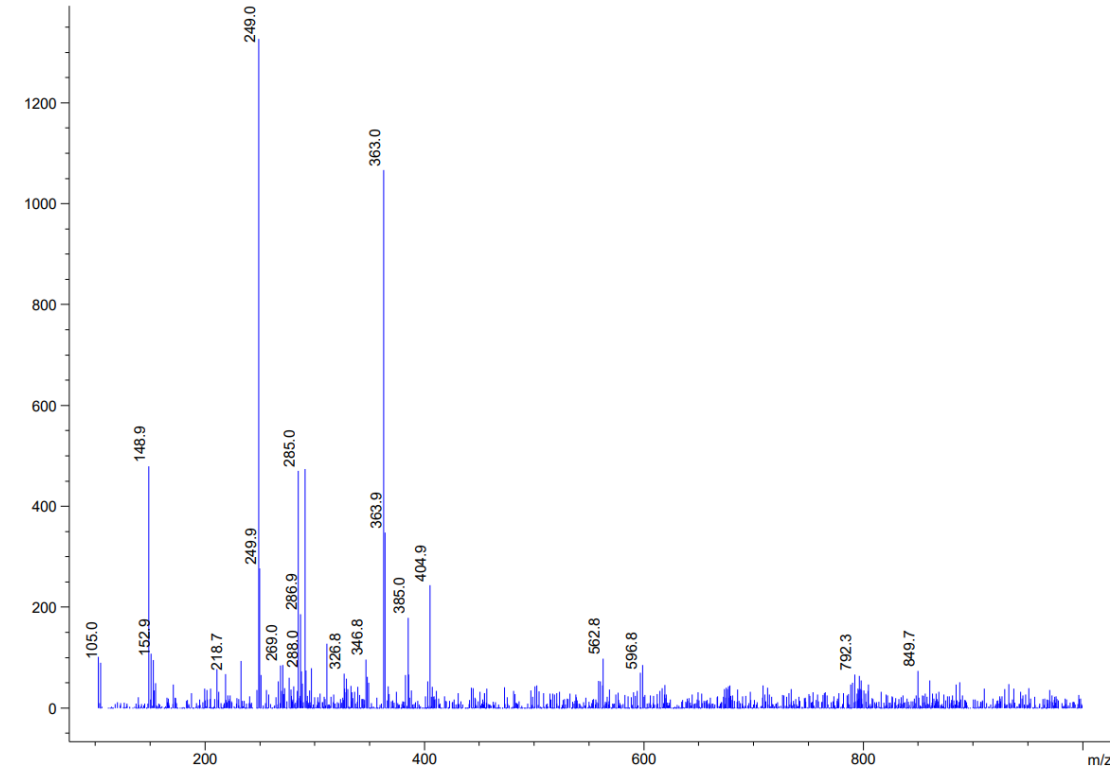


MS

[M+H]


251.0
233.0
235.0
221.0
273.0
252.0
293.0
315.0
111.4
132.2
156.4
175.6
195.2
216.6
222.0
242.9
267.4
300.4
329.6
360.6
378.3
398.0
416.6
439.6
474.4
494.6
516.4
536.4
559.8
585.6
610.8
631.6
654.0
682.4
716.5
750.0
779.8
800.6
821.6
853.8
875.8
900.8
920.8
945.3
964.4
995.8
35000
30000
25000
20000
15000
10000
5000
0
200
400
600
800
m/z

[M-H]


249.0
363.0
148.9
285.0
363.9
249.9
404.9
286.9
385.0
105.0
152.9
218.7
269.0
288.0
326.8
346.8
562.8
596.8
792.3
849.7
1200
1000
800
600
400
200
0
200
400
600
800
m/z